Feedbacks Between Plants, Flow, and Particle Fate

by

Elizabeth M. Follett

B.S. Chemical-Biological Engineering
Massachusetts Institute of Technology, 2009
M.S. Environmental Chemistry
Massachusetts Institute of Technology, 2011

SUBMITTED TO THE DEPARTMENT OF CIVIL AND ENVIRONMENTAL ENGINEERING IN PARTIAL FULFILLMENT OF THE REQUIREMENTS FOR THE DEGREE OF

DOCTOR OF PHILOSOPHY IN ENVIRONMENTAL FLUID MECHANICS

AT THE

MASSACHUSETTS INSTITUTE OF TECHNOLOGY

JUNE 2016

Signature redacted

Author .....
Department of Civil and Environmental Engineering
May 13, 2016

Signature redacted

Certified by .....
Heidi M. Nepf
Donald and Martha Harleman Professor of Civil and Environmental Engineering
Thesis Supervisor

Signature redacted

Accepted by .....
Heidi M. Nepf
Donald and Martha Harleman Professor of Civil and Environmental Engineering
Chair, Graduate Program Committee

Feedbacks Between Plants, Flow, and Particle Fate

by

Elizabeth M. Follett

Submitted to the Department of Civil and Environmental Engineering
on May 13, 2016, in Partial Fulfillment of the
Requirements for the Degree of Doctor of Philosophy in
Environmental Fluid Mechanics

Abstract

Environmental flows carry a wide variety of particles that interact with vegetation. Vegetated canopies are anchored by sediment, release pollen and seeds to colonize new ground, rely on nutrients carried by sediment, and may be killed by disease spores. While the influence of vegetation on flow profiles has been investigated, the transport of particles within vegetated canopies remains poorly understood. In this thesis I present the results from laboratory experiments and numerical modeling that investigated particle fate and transport around emergent and submerged model vegetation canopies.

The effect of canopy mediated flow on particle transport was explored in experimental studies using model vegetation. First, the flow diversion and extended wake region due to a circular patch of model reedy emergent vegetation resulted in regions of scour on the patch side and deposition in the patch wake, which are related to a non-dimensional flow blockage parameter. In-patch scour increased with turbulent kinetic energy levels, which were positively correlated to stem density. Second, within a long, submerged canopy, the capture of particles was reduced near the leading edge due to the presence of a vertical updraft. In the fully developed region, particle capture was increased for releases below the penetration of canopy scale vortices, and for particles with increased settling velocity.

The impact of canopy flexibility on turbulence within the canopy was explored using a submerged canopy of model flexible vegetation. The drag reduction due to reconfiguration was described through a drag coefficient that decreased as a power-law function of velocity, with a negative exponent (Vogel number). Velocity measurements made within and above the canopy demonstrate that unsteady reconfiguration, responding to individual turbulent events, preferentially allows stronger sweeps to penetrate the canopy, enhancing the skewness.

Next, spore escape was investigated across a range of canopy densities and particle settling velocities using a random displacement model (RDM) parameterized with an eddy diffusivity based on a simple set of physical parameters. This work filled a gap between field observations and traditional Lagrangian stochastic modeling, improving predictions of fungal spore escape to drive long range transport models. The effect of canopy and particle characteristics on the genotypic diversity of *Zostera marina* canopies was explored, pointing to the physical mechanisms governing successful pollination.

Thesis Supervisor: Heidi M. Nepf
Title: Donald and Martha Harleman Professor of Civil and Environmental Engineering

Acknowledgments

The feedback processes present in natural systems have always fascinated me. I am grateful to have had the chance to study the workings of the natural world in-depth during my years in graduate school, and especially to have worked with Heidi Nepf and Phil Gschwend. I consider myself lucky to have happened upon one, and then two, advisors who exemplify the best ideals of what it means to be a scientist, both in their research results and personal conduct. The members of my thesis committee, Eric Adams and Lydia Bourouiba, have encouraged me to stretch my capabilities and provided invaluable advice. I knew that I belonged at MIT when I first stepped foot on campus as a middle-school tourist, and my eleven years as part of this community have lived up to those initial dreams. The student communities of pika, East Campus, MIT Track & Field, and the Tech Catholic Community have supported and challenged me to grow as a researcher and friend. Finally, I remain grateful to my spouse, Chris Follett, and daughter, Marie. May our adventures continue to inspire us to grow in faith, hope, and love.

Contents

Chapter 1

Introduction

The feedbacks between plants, flow, and particle fate shape the size, shape, and resilience of vegetated regions, which provide key ecosystem services to the landscapes in which they reside. Vegetation acts as an ecosystem engineer by creating distinct regions of flow diversion, turbulent mixing, and quiescent flow, dependent upon canopy physical parameters. The relatively quiescent regions created by dense vegetated patches reduce turbidity and provide shelter for larvae and fish, enhancing local biodiversity (Crowder and Diplas, 2000, Roni et al., 2006, van Katwijik et al., 2016). Vegetated patches can directly alter landscape geomorphology by creating regions of scour and deposition, which promote the formation of teardrop river islands (Gurnell et al., 2001, 2008, Chen et al., 2012). The density and extent of vegetated canopies alters the canopy mediated flow profile, in turn influencing particle transport. Field observations imply that seagrass meadows adjust the stem density within the meadow to promote bed health, either encouraging sediment deposition through flow attenuation (high stem density), or promoting resuspension and export through an increase in stem-generated turbulence (low stem density), preventing anoxic conditions from forming in the seagrass bed (van Katwijk et al., 2010). The transport of pollen and escape of fungal spores, important to canopy genetic diversity and the long distance transport of fungal diseases, also depends on the canopy density and blade morphology, in addition to local wind speed. As vegetation alters the canopy flow profile, the position of the plants is in turn altered by the hydrodynamic forces, which cause flexible reconfiguration and, in extreme circumstances, uprooting and breakage (Luhar and Nepf, 2011, de Langre et al., 2012). In order to predict the resiliency and future growth of vegetation, it is necessary to consider particle transport in light of the

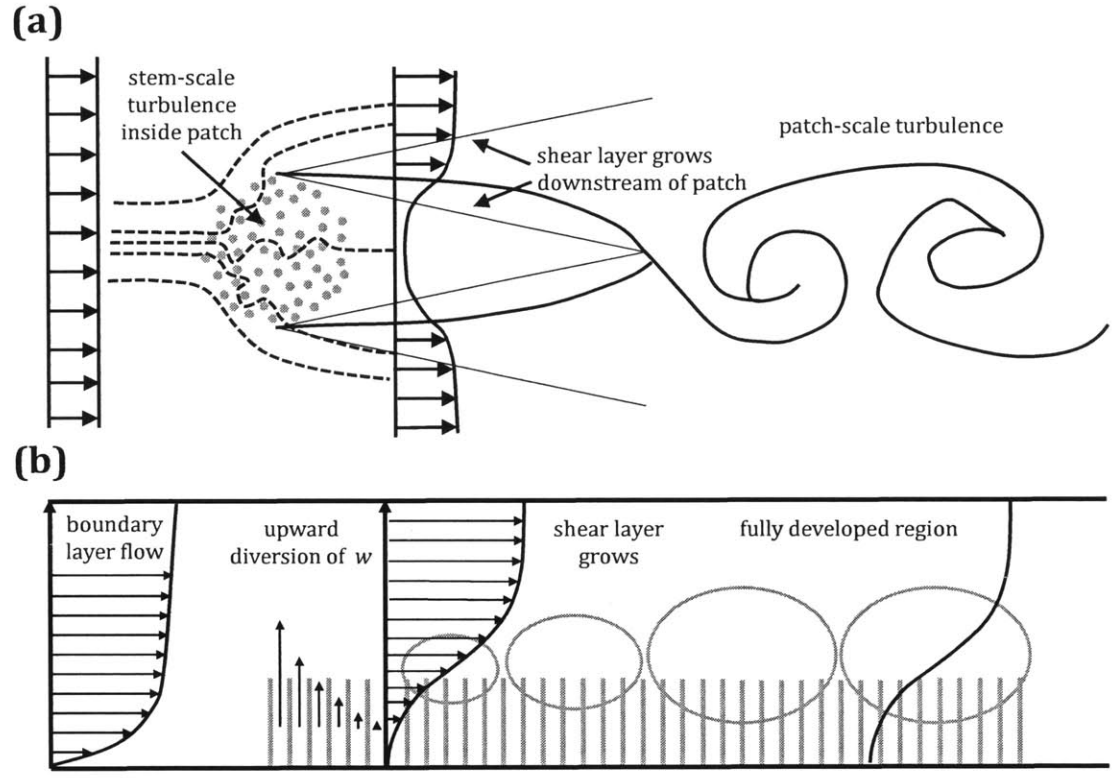

Figure 1-1: Schematic of flow development around vegetated canopies: (a) flow around a circular emergent patch, showing the delayed onset of the von Kármán vortex street and the extended wake region, and (b) upward diversion and development of the mixing layer over a submerged canopy, showing the growth and characteristic penetration distance of the canopy scale vortices.

canopy-mediated flow environment. For example, the importance of planting large, dense meadows has recently been recognized as beneficial to the success of seagrass restoration. This planting scheme allows for full flow attenuation, promoting nutrient deposition and establishment of the feedbacks conducive to seagrass growth (van Katwijk et al., 2016). This thesis considers particle fate and transport in emergent and submerged vegetated canopies through laboratory experiments and numerical modeling, connecting transport trends to the physical parameters governing the canopy mediated flow profile, as well as the particle size and density.

Previous investigators have characterized the flow structure around emergent and submerged vegetated canopies (Nepf, 2012). As flow approaches a circular emergent patch of vegetation, the

velocity begins to decelerate about one patch diameter upstream, as flow is diverted around this region of high drag (Zong and Nepf, 2012). Some flow travels through the porous patch, creating a steady wake region of slow streamwise flow directly behind the patch (Figure 1-1a). The presence of flow in this region delays the onset of the von Kármán vortex street, relative to flow around a solid cylinder. Deposition of fine suspended particles in the steady wake region may increase sediment nutrient content, promoting the growth of new vegetation.

Submerged canopies experience an upward deflection of velocity that begins upstream of the canopy, similar to the diversion of flow around the porous patch (Figure 1-1b). This vertical diversion reaches a maximum at the canopy leading edge and decays throughout the initial adjustment region of the canopy. A mixing layer profile is created, with faster flow above the canopy and slower flow inside the canopy (Ghisalberti and Nepf, 2002). This flow profile is inherently unstable, so that the regions of high and low momentum are mixed by canopy scale Kelvin-Helmholtz vortices. The vortices achieve a characteristic penetration distance, dependent upon the drag coefficient and canopy density (Nepf, 2007). In both terrestrial flows, which are unconfined, and deeply submerged aquatic flows, with submergence depth more than 10 times the canopy height, the flow within the canopy is driven by the turbulent stress at the top of the canopy. As the submergence depth decreases, the contribution of the pressure gradient increases, so that the flow is driven by both turbulent stress and the pressure gradient. In flows with submergence depth less than twice the canopy height, the extent of the mixing layer is restricted, reducing the size and penetration of canopy scale vortices (Nepf and Vivoni, 2000). For very sparse canopies, the drag from the vegetation is not strong enough to generate canopy scale turbulence, so that the canopy mixing is dominated by blade scale vortices. In the transitional region, the canopy scale vortices penetrate to the bed; as the canopy density increases, the vortex penetration distance is reduced, as the vortices are damped on vegetation elements. The region below the vortex penetration distance is relatively quiescent, characterized by slow streamwise flow and blade-scale turbulence, while the upper region of the canopy is routinely flushed by canopy scale vortices, increasing the streamwise velocity and enhancing turbulent transport. The fate of particles released within the canopy depends on the relative strength of competing transport processes, controlled by canopy and particle characteristics—ground deposition due to settling, deposition on canopy elements, and escape

from the canopy through turbulent transport. The balance between these processes depends on the relative strengths of the particle settling velocity and the canopy scale turbulence, represented by the canopy shear velocity, allowing the scaling of experiments to mimic terrestrial or aquatic processes. This thesis investigates the effect of the canopy mediated flow structure on particle fate and transport, relating transport trends to canopy and particle physical parameters.

1.1 Thesis structure

This thesis consists of five distinct chapters, some of which have been published or submitted for publication. Chapter 2 is a paper published as Follett and Nepf (2012). This chapter presents a description of the sediment patterns formed within and around a model patch of reedy emergent vegetation. The patch porosity, flow velocity, and flow depth were varied, resulting in a range of effects on bedload transport and fine particle deposition. Chapter 3 examines the capture of particles released within the initial adjustment and fully developed regions of a 10 m long rigid, submerged model canopy. The effect of the upward flow diversion over the initial adjustment region, the presence and penetration of canopy scale vortices in the fully developed region, and the effect of particle velocity ratio are examined. Chapter 4 is a paper published as Pan et al. (2014). In this chapter, the drag reduction due to flexible blade reconfiguration was described through a drag coefficient that decreased as a power-law function of velocity, with a negative exponent known as the Vogel number. Experimental observations of mean and unsteady one-dimensional linear elastic reconfiguration over a model seagrass meadow (Ghisalberti and Nepf, 2006) are used to explain the influence of the drag reduction on the size and penetration of canopy scale events, which is reflected in the velocity skewness. Chapter 5 is a paper published as Follett et al. (2016). This chapter describes the physical influence of the canopy on flow and fungal spore transport through a random displacement model forced by a physically based family of curves of mean longitudinal velocity and eddy diffusivity, using canopy parameters often measured in the field. This method predicts the average fraction of spores escaping the canopy without detailed turbulence measurements, enabling a physically realistic description of particle escape to drive long-distance transport models of fungal transport in field crops. In Chapter 6, the fate and transport of seagrass pollen is explored as a

function of canopy and particle characteristics. Intraspecies genetic diversity, which depends on successful transport of pollen from the point of release to flowers, has recently been recognized as a key metric of seagrass health (Hughes and Stachowicz, 2004), so that the health and resiliency of seagrass beds could be influenced by the transport of particles within canopy mediated flow.

References

Chen, Z., Ortiz, A., Zong, L., Nepf, H., 2012. The wake structure behind a porous obstruction and its implications for deposition near a finite patch of emergent vegetation. Water Res. Res. 48, W09517.

Crowder, D.W., Diplas, P., 2000. Evaluating spatially explicit metrics of stream energy gradients using hydrodynamic model simulations. Canadian Journal of Fisheries and Aquatic Sciences 57 (7), 1497.

Follett, E., Nepf, H., 2012. Sediment patterns near a model patch of reedy emergent vegetation. Geomorphology 179, 141-151.

Follett, E., Chamecki, M., Nepf, H., 2016. Evaluation of a random displacement model for predicting particle escape from canopies using a simple eddy diffusivity model. Agricultural and Forest Meteorology 224, 40-48.

Ghisalberti, M., Nepf, H., 2002. Mixing layers and coherent structures in vegetated aquatic flows. Journal of Geophysical Research 107 (C2), 3011.

Ghisalberti, M., Nepf, H., 2006. The structure of the shear layer in flows over rigid and flexible canopies. Environmental Fluid Mechanics 6, 277-301.

Chapter 2

Sediment patterns near a model patch of reedy emergent vegetation[1]

[1]This chapter has been previously copyrighted by Elsevier Ltd. and is therefore excluded from the MIT copyright covering other chapters of this thesis. Citation: Follett, E., Nepf, H., 2012. Sediment patterns near a model patch of reedy emergent vegetation. Geomorphology 179, 141-151. doi:10.1016/j.geomorph.2012.08.006

Geomorphology 179 (2012) 141–151

Contents lists available at SciVerse ScienceDirect

Geomorphology

journal homepage: www.elsevier.com/locate/geomorph

Sediment patterns near a model patch of reedy emergent vegetation

Elizabeth M. Follett *, Heidi M. Nepf

Department of Civil and Environmental Engineering, Massachusetts Institute of Technology, MIT Bldg. 48-216, 77 Massachusetts Avenue, Cambridge, MA 02139, USA

ARTICLE INFO

Article history:
Received 16 March 2012
Received in revised form 7 August 2012
Accepted 10 August 2012
Available online 23 August 2012

Keywords:
Emergent vegetation
Sediment transport
Wake
Deposition
Flume
Porous patch

ABSTRACT

This laboratory study describes the sediment patterns formed in a sand bed around circular patches of rigid vertical cylinders, representing a patch of reedy emergent vegetation. The patch diameter was much smaller than the channel width. Two patch densities (solid volume fraction 3% and 10%) and two patch diameters (22 and 10 cm) were considered. For flows above the threshold of sediment motion, patterns of sediment erosion and deposition were observed around and within the patch. Scouring within the patch was positively correlated with turbulent kinetic energy in the patch. For sparse patches, sediment scoured from within the patch was mostly deposited within one patch diameter downstream of the patch. For dense patches, which experience greater flow diversion, sediment scoured from the patch was carried farther downstream before deposition along the patch centerline. Differences between the sparse and dense patch patterns of deposition are explained in the context of flow diversion and wake structure, which are related to a nondimensional flow blockage parameter. While sediment was redistributed near the patch, observations suggest that net deposition was not recorded at the reach scale.

1. Introduction

Vegetation can increase flow resistance and reduce flow conveyance so that many consider it a nuisance in culverts and stream channels (Kouwen and Unny, 1975). However, vegetation improves water quality by removing nutrients from and releasing oxygen to the water column (Chambers and Prepas, 1994; Wilcock et al., 1999; Schulz et al., 2003). It also promotes habitat diversity by creating a diversity of flow regimes (Crowder and Diplas, 2000; Kemp et al., 2000; Crowder and Diplas, 2002). The bed stabilization effects of vegetation have been widely recognized (Wynn and Mostaghimi, 2006; Afzalimehr and Dey, 2009; Wang et al., 2009; Li and Millar, 2010; Pollen-Bankhead and Simon, 2010). As an example, vegetation has been shown to stabilize both single thread (Tal and Paola, 2007) and meandering (Braudrick et al., 2009) channel morphologies. Sediment loading from bank erosion is also diminished by vegetation (Lawler, 2008). The reduction of velocity within vegetated regions can encourage deposition of fine particles and sediment retention (Abt et al., 1994; Lopez and Garcia, 1998; Cotton et al., 2006; Gurnell et al., 2006) and promote the growth of ridges and islands (Edwards et al., 1999; Tooth and Nanson, 1999; Gurnell et al., 2001, 2008). Similarly, aeolian literature reports that vegetation accelerates the nucleation of dunes (Luna et al., 2011). While most studies have focused on enhanced deposition within vegetated regions, vegetation also promotes erosion under some conditions. Specifically, close to vegetated regions of finite width, the diversion of flow away from the vegetation leads to the acceleration of flow along the vegetation edge, which causes localized erosion (Fonseca et al., 1983; Bouma et al., 2007; Bennett et al., 2008; Rominger et al., 2010).

Recognizing the benefits of vegetation to river health, ecologically minded management and replanting of denuded regions are now encouraged (Mars et al., 1999; Pollen and Simon, 2005). However, successful river restoration requires an understanding of how vegetation impacts flow and sediment transport. For example, Larsen and Harvey (2011) explained the stability of different landscape patterns in the Everglades by coupling vegetation dynamics to both sediment transport and flow. While many studies have described long, uniform reaches of vegetation, only a few have considered finite patches of vegetation. Bennett et al. (2002, 2008) described how the introduction of finite patches along the wall of a channel changes the flow and erosion pattern. The channel response was found to depend on both the shape and density of the rigid model stems. In particular, alternating patches of semicircular shape were recommended to promote the restoration of meandering geometries.

In this study we consider the erosion pattern associated with a circular patch of emergent vegetation located at mid-channel, making connections to flow structure previously described by Zong and Nepf (2012). Zong and Nepf considered circular arrays of diameter D constructed from circular cylinders, each of diameter d, at a density of n cylinders/m^2. This produced a frontal area per unit volume of $a = nd$, and a solid volume fraction of $\phi = n\pi d^2/4$ within the patch. Upstream of the patch, the velocity is uniform with magnitude U_0 (Fig. 1). As flow approaches the patch, the velocity begins to decelerate about $1D$ upstream, as flow is diverted around this region of high

Abbreviations: SAFL, Saint Anthony Falls Laboratory; TKE, turbulent kinetic energy.

* Corresponding author. Tel.: +1 847 471 8878; fax: +1 817 258 8850.
E-mail addresses: emf@mit.edu (E.M. Follett), hmnepf@mit.edu (H.M. Nepf).

0169-555X/$ – see front matter © 2012 Elsevier B.V. All rights reserved.
http://dx.doi.org/10.1016/j.geomorph.2012.08.006

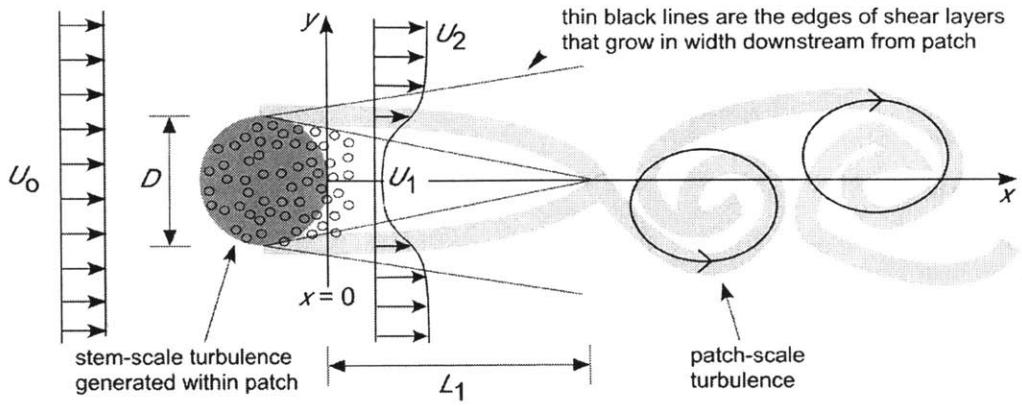

Fig. 1. Schematic diagram of wake behind a porous circular patch (grey shaded circle) showing upstream velocity (U_o), steady wake velocity (U_1), velocity outside the wake (U_2), and the length of the steady wake region (L_1). Stem-scale turbulence shown by small black circles within and just behind the patch. Light grey lines represent tracer released at the two sides of the patch. The tracer reveals the eventual onset on the von Kármán vortex street.

drag. Diversion and flow deceleration continue through the patch. While the mean velocity within the patch is diminished relative to the free stream, the turbulence levels may be enhanced, as turbulent eddies form in the wake of each individual cylinder.

Because the patch is porous, some flow penetrates through the patch, creating an area of slow streamwise velocity directly behind the patch, which we call the steady wake region. The presence of flow in the steady wake delays the onset of the von Kármán vortex street and thus alters the wake structure relative to that observed behind a solid obstruction (Nicolle and Eames, 2011; Zong and Nepf, 2012). The flow in the steady wake (U_1) separates two regions of faster velocity (U_2), creating a shear layer on either side of the steady wake. These layers grow linearly with distance from the patch, eventually meeting at the wake centerline (Fig. 1). At this point, the interaction between the shear layers results in the von Kármán vortex street. The length L_1 between the end of the patch and the onset of the von Kármán vortex street defines the length of the steady wake region (Ball et al., 1996). The length of the steady wake region (L_1) may be predicted from the growth of the linear shear layers and the patch geometry (Zong and Nepf, 2011),

$$L_1 = 2.5D\frac{(1+U_1/U_2)}{(1-U_1/U_2)} \approx 2.5D\frac{(1+U_1/U_o)}{(1-U_1/U_o)} \quad (1)$$

The right most expression assumes $U_2 = U_o$, which is reasonable if D is much less than the channel width, which is valid in our experiments.

The formation of the von Kármán vortex street provides a lateral flux of momentum that erodes the velocity deficit in the wake. After the additional distance L_2, the velocity profile again approaches the upstream value, U_o. The region L_2 is called the wake recovery region. Based on data given in Zong and Nepf (2012), we propose the following empirical relation:

$$\frac{L_2}{D} = 13\frac{U_1}{U_o} + 4 \quad (2)$$

The total length of the wake is $L_1 + L_2$.

For a solid cylinder, the von Kármán vortex street begins immediately behind the obstruction, so that $L_1 = 0$, and $L_2/D \approx 3$ ($Re_D =$ 23000; Zong and Nepf, 2012). Behind a porous obstruction, L_1 and L_2 increase with increasing steady wake velocity, U_1 (Eqs. (1) and (2)). Because U_1 increases with increasing patch porosity (i.e. decreasing ϕ), L_1 and L_2 increase with decreasing ϕ. Because these length scales describe important features of the flow field, i.e., the onset of the von Kármán vortex street (L_1) and the end of the wake velocity deficit ($L_1 + L_2$), we hypothesize that they can be connected to the pattern of erosion and deposition observed near a patch. This hypothesis will be tested in the current study.

Bedload transport is characterized by the bed shear stress,

$$T = \rho u_*^2 \quad (3)$$

with ρ the fluid velocity and u_* the bed shear velocity. When the bed shear stress exceeds a critical value (τ_c), sediment motion is initiated; for conditions of $\tau > \tau_c$, sediment motion increases monotonically with increasing τ (e.g., Julien, 1998). Bed shear stress is known to increase with velocity, but it may also be elevated by turbulent motions (Diplas et al., 2008). From the flow description given above, we expect increased bed shear stress, and therefore increased sediment movement, along the sides of the patch and within the von Kármán vortex street. Because small-scale turbulence may also be generated within the patch, scour is also possible within the patch. Alternatively, we expect bedload accumulation in regions of reduced bed shear stress, specifically in the steady wake region of length L_1, where both velocity and turbulence are diminished.

While we anticipate that a finite patch of vegetation will change bedload transport locally (described above), at the reach scale we expect that the introduction of an isolated patch of vegetation will have little impact. This is because a finite patch alters the flow field over a limited distance (L), beginning about D upstream of the patch and extending downstream a distance $L_1 + L_2$ (i.e., $L = 2D + L_1 + L_2$). Beyond this distance, the flow—and therefore the bedload transport—should be unaffected by the patch. This idea will be tested experimentally by considering the change in net deposition integrated over the length scale L. Note, this length scale should be slightly extended to reflect the saltation distance (L_s). Once a particle of diameter d_s is set in motion, it travels (on average) over a length scale $L_s = 150d_s$ (Habersack, 2001). For typical sand grain sizes, this length scale is on the order of 10 cm.

The scour and deposition associated with a circular patch of vegetation will be compared to that observed for a solid cylinder. Dargahi (1990) investigated scour and deposition around an emergent circular cylinder of diameter $D = 0.15$ m, in a flow of 20-cm depth and 26 cm/s, which are comparable to the flow conditions used here. We use D to denote diameter to allow comparisons to patches of diameter D. Dargahi observed scour beginning 25 s after the initiation of the experiment. The scour hole was roughly circular, extending $1.5D$ upstream from the leading edge and $2D$ downstream from the trailing edge of the cylinder. The sediment scoured from around the cylinder was deposited in a mound that extended to nearly $6D$ downstream from the back of the cylinder. The lateral motion associated with the von Kármán vortex street carried sediment toward the

wake centerline so that the deposition mound was on the wake centerline. The volume of scour balanced the volume of deposition so that at the reach scale no net change in sediment volume occurred, which is consistent with the argument presented for finite vegetation patches given in the previous paragraph.

2. Materials and methods

Experiments were conducted at the St. Anthony Falls Laboratory (SAFL; Minneapolis, MN) in a 5-m-long, 1.2-m-wide sediment flume that was filled with an 8-cm layer of Silurian pool filter sand (U.S. Silica, Frederick, MD). The upstream sediment level did not change during the experiment, indicating that the sediment was not supply limited. The median sand grain diameter was 500 μm, and the density was 2.65 g/cm^3. The flume was fed by water drawn from the Mississippi River and controlled by a manual valve. A weir located at the downstream end of the flume was adjusted to achieve the desired flow depth. Circular patches were constructed from cylindrical wooden rods ($d=0.64$ cm) placed in a perforated plastic board. Patches were constructed with the following diameters and solid volume fractions: ($D=10$ cm, $\phi=0.1$), ($D=22$ cm, $\phi=0.1$), and ($D=22$ cm, $\phi=0.03$). The maximum patch diameter, D, was 0.18 of the channel width so that the walls have little influence on the flow near the patch. Using a rigid stem model simplifies construction, and it is justified because we focus on conditions with emergent vegetation—for which the flow response is largely two-dimensional, with the flow diversion and the dominant shear layers in the horizontal plane. As long as the plants remain emergent, the magnitude of diversion and lateral shear is set by the nondimensional flow blockage (aD). While a flexible stem might allow flow blockage to change with flow speed, for a given flow blockage, the flow structure in the wake will be the same (Chen et al., 2012). Finally, the basal region of most real stems is rigid, so that our model correctly captures the stem geometry close to the bed (Leonard and Luther, 1995; Leonard and Reed, 2002).

Velocity upstream of the patch was measured with a Nortek Vectrino. The Vectrino was secured to a bar placed on top of the flume, and it was unclamped and moved along the bar to measure different locations across the flume. At the start of each run, the flow rate was manually adjusted until the velocity measured 5 cm below the water surface reached a preselected target velocity (20, 30, or 40 cm/s). A vertical velocity profile was then measured upstream of the patch and 1 m from the inlet flow straightener. Velocity was recorded at each point for 240 s at a sampling rate of 25 Hz. The vertical profile of time-averaged velocity was depth-averaged to obtain the upstream velocity U_o. A lateral transect of velocity was also taken upstream of the patch to confirm the lateral uniformity of the flow profile. Behind the patch, a measurement of U_1 (Fig. 1) was made using a handheld SonTek FlowTracker sampling at 10 Hz over a 30-s interval. Velocity was measured at 0.2 and 0.8 times the water depth. The mean of these values is an estimate for the depth-averaged velocity.

Because we were not able to make velocity measurements within the patch, the turbulence associated with stem generation was estimated using a relation developed and experimentally verified by Tanino and Nepf (2008):

$$k_t = u^2\left|\frac{\phi}{(1-\phi)\pi/2}\right|^{2/3} \approx U_o^2\left(nd^2/2\right)^{2/3} \quad (4)$$

where $k_t \equiv \left(\overline{u'^2}+\overline{v'^2}+\overline{w'^2}\right)/2$ is the turbulent kinetic energy per fluid mass. The right-most expression assumes $\phi \ll 1$ and substitutes $\phi = n\pi d^2/4$ to explicitly show the relationship with stem density, n. Further, because we were not able to measure velocity inside the patch, we substitute $u = U_o$. With this approximation Eq. (4) cannot predict the absolute magnitude of turbulence within the patch but can still serve as a comparative metric between patches. Finally, Eq. (4) is strictly valid only for stem Reynolds numbers $Re_d = ud/\nu > 100$, the limit above which shedding of vortices from the stems is present.

The bed friction velocity, $u_* = \sqrt{\tau/\rho}$, was estimated from a logarithmic profile, assuming smooth turbulent conditions (Julien, 1998),

$$\frac{U_o}{u_*} = 5.75\log\left(\frac{u_* h}{\nu}\right) + 3.25 \quad (5)$$

where h is the water depth, and ν is the kinematic viscosity of water. This profile is valid for $Re_* = \frac{u_* d_s}{\nu} < 4$. Our Re_* values ranged from 2.6 to 9.3, which technically fall in the transition regime. However, estimates of shear velocity were similar (within 5%) using the rough turbulent ($Re_* > 70$) and smooth turbulent profiles.

The change in bed elevation was found by differencing bed elevation before and after exposure to flow. A Keyence LK-G laser, mounted on a motorized track above the flume, measured the distance to the sediment bed every 2 mm across the flume and every 5 mm along the flume (parallel to the flow field). Before each run, the sand was smoothed with a 1-m-long rigid plastic board, and sediment inside the patch was manually smoothed in order to provide similar initial conditions for each run. The sediment was scanned before and after several hours of flow. The scans were interpolated and plotted in Matlab using code written by Craig Hill (University of Minnesota, Minneapolis, MN). In order to remove very large values associated with individual rods, cells with distances <700 mm from the laser or with gradients >0.6 mm/mm were removed; replacement values were interpolated from surrounding cells. Scans taken before and after each run were differenced to find the net deposition as a function of x (streamwise) and y (lateral). Longitudinal transects of laterally averaged deposition were constructed by summing across each lateral (y) scan.

In order to find the net deposition within the patch, the patch center was located using an uncorrected scan, which showed the dowel rods; a circle was defined using the patch center and known radius. Values of net deposition inside the circle were summed in order to find the total net deposition volume within the patch. Net deposition behind the patch was defined as the net deposition within a square of side length D centered directly behind the patch. Uncertainty in the net deposition within and directly behind the patch was estimated by shifting the circle or square by 1 cm in each coordinate direction.

The net deposition at the reach scale was estimated from the average change in sediment height over the area covered by the laser scan. In cases where scour extended upstream of the laser scan, we extrapolated the laterally averaged deposition upstream to the point of zero net deposition. This extrapolation is consistent with the shape of upstream scour holes measured within the laser scan limits and the scour holes measured by Dargahi (1990). For some cases (4, 5, and 10), the net deposition extended downstream beyond the footprint of the scan (an example is discussed in the results section). In these cases, we extrapolated the laterally averaged net deposition from the end of the laser scan to a point of zero deposition at L_1+L_2. This was justified because visual observations confirmed that the patch-induced bedform extended behind the patch approximately L_1+L_2, as anticipated in Section 1. Uncertainty in the channel average net deposition (± 1.1 mm) was estimated by comparing two sets of replicates. The variation between replicates was in part caused by the deposition of fine particles, which were present in the Mississippi River water. The concentration of suspended particles varied from day to day, based on observed water clarity. Fine particle deposition was readily apparent from the contrast between the dark brown fine particles and the light tan of the Silurian pool filter sand.

The length of the steady wake, L_1, was estimated using dye, following a method similar to that of Zong and Nepf (2012). Red dye was injected near the surface directly behind the patch, and movies were taken of the dye motion. The point at which von Kármán

oscillations were first observed marked the end of the steady wake region. After this evaluation, the flow was left to run for several hours. We chose run times that allowed us to replicate the distinct patterns of erosion and deposition at different flow velocities—2 hours for 40 cm/s velocity, 5 hours for 30 cm/s velocity, and overnight for 20 cm/s velocity. These run times are consistent with Dargahi (1990) who, for comparable flow speeds and depths, observed intense scouring for 3 hours, with 60% of the final scour depth reached after 2 hours. After each run, the flow was stopped and the flume allowed to drain. Excess water was bailed; the remaining water was aspirated, or sucked out of the flume using a hose. Once dry, a laser scan was run on the sediment formation; pictures of the sediment and apparatus were taken.

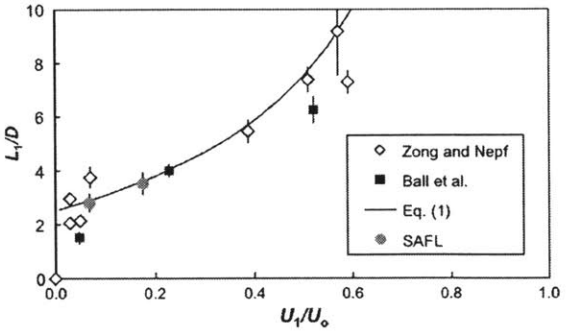

Fig. 3. L_1/D vs. U_1/U_o. L_1 is measured by dye injection. Model Eq. (1) is shown as a solid line.

3. Results

3.1. Flow field

Because it was not feasible to make longitudinal transects of velocity in the SAFL flume, we utilized the detailed transects measured by Zong and Nepf (2012). To do so, we first confirmed that our measured values of U_1 were consistent with those of Zong. Although Zong considered $U_o = 10$ cm/s and the SAFL experiments consider a range of U_o (10 to 33 cm/s), the flow distribution is expected to be self-similar, i.e., for the same ϕ and D, U/U_o will be the same. This is confirmed in Fig. 2, which shows the longitudinal transects (U/U_o, x/D) made by Zong for $D = 22$ cm, $\phi = 0.1$ and $\phi = 0.03$, along with the value of U_1/U_o measured in the SAFL experiments. The SAFL points represent the mean U_1/U_o ratio, and the error bar denotes the standard deviation for all measurements at a given patch geometry (D, ϕ). For both transects, the SAFL values overlap with the detailed profiles of Zong. For the patch $D = 10$ cm, $\phi = 0.1$, we measured $U_1/U_o = 0.25 \pm 0.13$, compared to Zong's $U_1/U_o = 0.22 \pm 0.02$ (data not shown). Furthermore, our values of L_1 are consistent with the model prediction (Eq. (1)) and with measurements from previous studies (Fig. 3). Given these confirmations, we are confident in using Eqs. (1) and (2) to predict L_1 and L_2, respectively, when these length scales could not be measured directly (Table 1).

The adjustment of flow near the patch depends on the degree of flow blockage provided by the patch, which is described by the patch width, D, and the frontal area within the patch, a. Together, these define a dimensionless flow blockage parameter, aD. The flow diversion and velocity reduction within the patch increase as aD increases. For example, in Fig. 2 the velocity is reduced to a greater extent for the patch with higher aD, specifically $\phi = 0.1$, $aD = 4.4$. In addition, for this case the velocity becomes negative at the end of the steady wake region (about $x/D = 3$), indicating the presence of a recirculation zone similar to that observed behind a solid body. No recirculation exists behind the sparser patch ($\phi = 0.03$, $aD = 1.3$). A recirculation zone is only present for patches with $aD > 4$ (Chen et al., 2012). Consistent with this, the smaller dense patch ($D = 10$ cm, $\phi = 0.1$, $aD = 2.0$) does not have a recirculation zone. Later we will see that the presence of the recirculation zone leaves a specific signature in the sediment pattern.

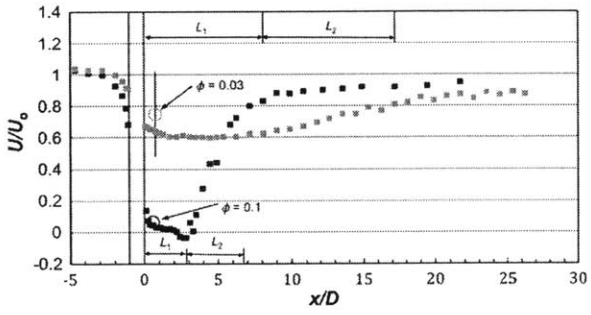

Fig. 2. Plot of U/U_o vs. x/D for a patch of diameter $D = 22$ cm. Patch is located between $x/D = -1$ and 0. L_1 and L_2 are plotted for reference. Profiles measured by Zong and Nepf (2012) shown by small squares: $\phi = 0.1$, $aD = 4.4$ (grey squares) and for $\phi = 0.03$, $aD = 1.3$ (black squares). Our measurements are shown by open circles in grey ($\phi = 0.03$, $aD = 1.3$) and black ($\phi = 0.1$, $aD = 4.4$). The vertical bar on our points corresponds to the standard deviation among all cases with the same aD.

3.2. Solid cylinder

The expected pattern of scour and deposition around a solid cylinder (Dargahi, 1990; Simpson, 2001) was observed in the SAFL flume for a cylinder of diameter $D = 3$ cm (Fig. 4). Unfortunately, we did not capture a laser scan for the initially flat bed, so estimates of net deposition are not possible; however, regions of scour (blue) and deposition (red) are still clearly evident. The white circle indicates the position of the cylinder, and flow occurred from left to right. A circular scour hole is centered on the obstruction with a diameter of 3.5D; the deposition mound is located on the wake centerline, extending to about 7D. Both observations are consistent with Dargahi (1990), discussed in Section 1. The maximum deposition is located at about 4.8D. The scour hole has a maximum depth of 3.4 cm (about 1D). The pattern of scour and deposition observed for the solid cylinder is contrasted below with the patterns observed for porous patches.

3.3. Porous patch

The scour and deposition observed for four porous patch experiments are shown in Fig. 5. In the colored contour plots, the upstream ($x/D = -1$) and downstream ($x/D = 0$) limits of the patch are marked with black vertical lines. Flow was in the positive x direction. The corresponding, laterally averaged deposition is shown next to each contour plot. The wake length scales L_1 and L_2, defined by Eqs. (1) and (2), are shown within the plot—except for case 17, for which the length scales were too far downstream ($L_1 + L_2 = 615$ cm).

We first discuss cases 4 and 5, which represent patches with high flow blockage ($D = 22$ cm, $\phi = 0.1$, $aD = 4.4$; Fig. 5A and B). Although these two cases have different channel velocity, $U_o = 33$ cm/s (case 4) and 17 cm/s (case 5), the patterns of deposition and erosion are similar, which is consistent with the fact that the spatial pattern of the flow is similar, as set by the flow blockage. The sediment pattern for these two cases differs in several ways from that observed with a solid object. First, unlike the circular scour region observed around the solid cylinder (Fig. 4), the scour near the porous patch (blue color) has a horseshoe shape, with deposition replacing scour directly downstream of the patch. The flow passing through the patch (U_1) delivers sediment that is subsequently deposited directly

Table 1
Summary of experimental conditions.[a]

Expt #	U_o (cm/s)	a (cm^{-1})	ϕ	D (cm)	h (cm)	U_1 (cm/s)	Duration (h)	In-patch scour (cm^3)	Deposit behind patch (cm^3)	L_1 (cm)
1	25	0.20	0.1	22	12	0.4	2	−840±60	420±9	65
2	13	0.20	0.1	22	23	0.7	2	40±11	42±1	>120
3	25	0.20	0.1	22	12	0.4	2	−83±18	21±2	70
4	33	0.20	0.1	22	13	2.8	2	−2475±2	−200±20	58
5	17	0.20	0.1	22	9	1.3	23	−1450±60	29±12	52
6	20	0.06	0.03	22	9	–	23	−490±20	704±12	>120
7	24	0.06	0.03	22	12	–	5	−660±20	830±20	>120
8	16	0.06	0.03	22	24	–	23	24±1	42±0.3	>120
9	21	0.06	0.03	22	26	1.3	5	14±2	19±1	>120
10	32	0.20	0.1	10	13	1.3	2	−565±6	−209±13	42
11	26	0.20	0.1	10	14	0.9	2	−269±12	150±10	31
12	20	0.20	0.1	10	11	4.2	5	−266±12	139±9	34
13	15	0.20	0.1	10	9	3.1	19	−60±70	41±3	36
14	17	0.20	0.1	10	9	1.4	4.25	−274±13	153±7	33
15	19	0.06	0.03	22	13	18	4.25	−1110±20	860±20	>120
16	10	0.20	0.1	22	23	0.9	19	−39±2	62±2	36
17	30	0.06	0.03	22	12	21	2	−1228±12	940±30	>120
±	0.5			0.5	0.5	0.5				2

[a] Depth-averaged velocity U_o (m/s), frontal area per unit volume a (cm^{-1}), solid volume fraction ϕ, patch diameter D (cm), flow depth h (cm), flow in the steady wake zone behind the patch U_1, duration of flow (hours), in-patch scour (cm^3), direct deposit behind patch in a square of side length D centered directly behind the patch (cm^3), and L_1 (cm) estimated from dye injections. In several cases L_1 was greater than 120 cm, the end of the visual zone; for these cases, L_1 is denoted >120. U_1 was not measured for experiments 6–8. Uncertainty given in last row.

downstream of the patch (red mound just past $x/D=0$). Second, unlike the solid object (Fig. 4), scour extends very little upstream of the porous patches. This is based on visual observation not captured in the scans. Looking at the laterally averaged transect, we see that in each case scour began at the front of the patch, increased with distance inside the patch for about 0.5D, and then began decreasing. Third, there exist two distinct regions of deposition: the first mound directly downstream ($x/D\approx0.2$) and a second mound distributed over some distance downstream, but with a peak at $x/D\approx5$. The position of the second peak in deposition is similar to that observed for the single deposition mound observed behind a solid cylinder (at $x/D=4.8$; Fig. 4). Notably, the second region of deposition falls on the wake centerline, similar to the solid cylinder; this is again attributed to the lateral transport provided by the von Kármán vortex street. Indeed, the second region of deposition occurs just after the onset of this vortex street, i.e., $x>L_1$ (Fig. 5A,B; cases 4 and 5). Some aspects of the dense patch deposition will show similarity with the solid cylinder because, as flow blockage increases, the wake structure approaches that of a solid cylinder. Numerical studies done by Nicolle and Eames (2011) suggested that this occurs for $aD>\approx9$. Beyond this limit the wake structure, and likely the deposition pattern, will be identical to that of a solid object.

Perhaps the most striking feature in the wake of this high flow blockage patch is the triangular ridge that grows from the bar of sediment behind the patch (Fig. 5A,B; $x/D=0.25$ to $x/D=2.4$). The tip of this triangle is located just before L_1 and corresponds to the position at which the recirculation zone occurs at the end of the steady wake (Fig. 2). As noted above, a recirculation zone is present only for cases with $aD\geq4$. The region inside the triangle did not experience any sand accumulation or depletion. Saltation was observed along the raised border of the triangle but not inside the region, suggesting that bedload transport did not occur inside this region. However, fine particle deposition from the mean flow was observed, as indicated by the contrast between the dark fine particles and lighter color of the Silurian pool filter sand in a photograph (Fig. 6).

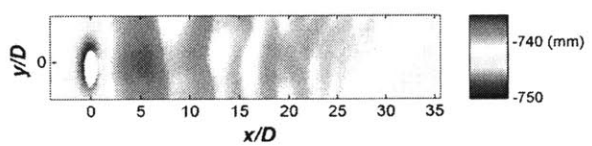

Fig. 4. Laser scan of sediment formation around solid cylinder of diameter $D=3$ cm. The white oval indicates the position of the cylinder; the y coordinate has been stretched. Because a laser scan was not taken prior to this experiment, the sediment is not zeroed. Units are mm from the laser probe.

For these patches ($aD=4.4$), the wake length defined by L_1+L_2 is a good measure of the length of the bed formation associated with the patch. This is visually demonstrated in the panoramic photograph of case 5 (Fig. 6). Near the position marked L_1+L_2, the relatively smooth mound of wake deposition ends; the sediment pattern returns to spanwise ripples, similar to that observed upstream of the patch. From the above discussion, we suggest that for $aD>4$, the wake length scales L_1 and L_2 can describe key features in the deposition and erosion pattern.

Next, we consider case 17 (Fig. 5C), which was the sparsest patch we considered and the lowest flow blockage ($\phi=0.03$, $D=22$ cm, $aD=1.3$). Compared to a high flow blockage experiment with comparable D, h, and U_o (case 4, Fig. 5A), the pattern of deposition and erosion has several differences. First, because the changes in the velocity are less pronounced and occur more gradually over space (Fig. 2), the resulting sediment pattern is more diffuse—i.e., the features are less sharply delineated. For example, the scour around the edge of the patch is less pronounced because the flow diversion is less severe (Fig. 5, cases 4 and 17). Second, the mound of deposition directly behind the patch ($0<x/D<1$) is larger. This is discussed further below. Third, deposition beyond the first mound ($x/D>1$) does not occur on the wake centerline but creates a formation that is open to the downstream direction. This open formation is consistent with the absence of a recirculation zone and with the very large value of L_1, which is beyond the end of the image shown. Recall that the von Kármán vortex street provides the mechanism for sediment transport toward the wake centerline, but this mechanism is only present for $x>L_1$. The absence of this lateral transport mechanism near the patch results in deposition that is offset from the centerline, as seen in case 17. We conclude that open formations (e.g., case 17) are favored with low flow blockage patches that produce long regions of steady wake, and closed formations (e.g. case 5) are favored with high flow blockage patches.

Although L_1+L_2 was estimated to be much longer for case 17 than for cases 4 and 5, the length of the sediment formation was similar (Fig. 5). Specifically, in case 5, $L_1+L_2\approx8D$; this length is consistent with the length of the sediment formation (Fig. 6). By contrast, for

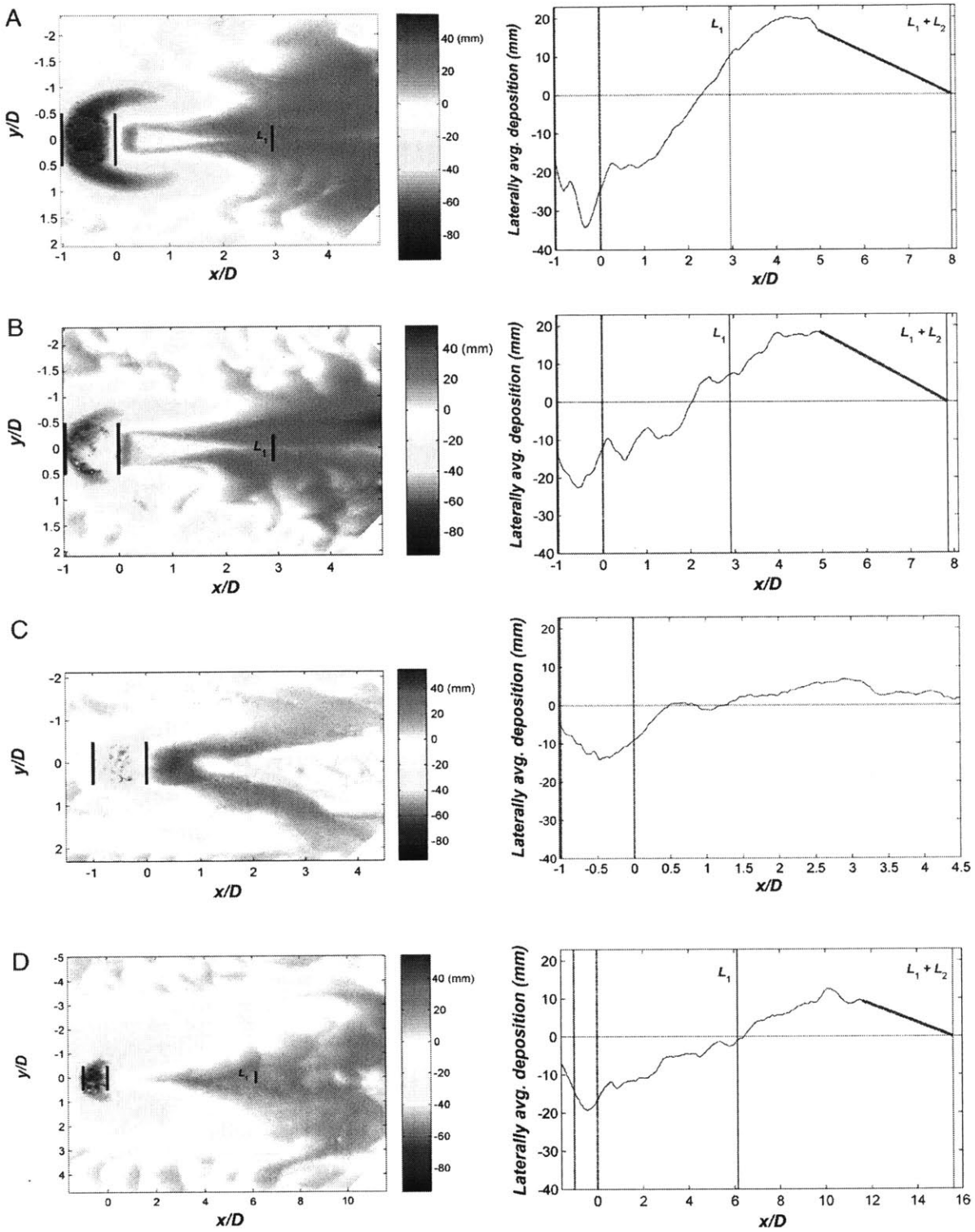

Fig. 5. Net deposition estimated from laser scans. Yellow indicates zero net deposition; red and orange indicate positive net deposition; blue and green indicate negative net deposition (scour). Longitudinal (x/D) profiles of laterally averaged net deposition are located next to each laser scan. The patch is located between $x/D = -1$ and 0, noted by vertical dashed lines in the laterally averaged profiles. (A) case 4: $\phi = 0.1$, $D = 22$ cm, $U_o = 0.33$ m/s, $aD = 4.4$; (B) case 5: $\phi = 0.1$, $D = 22$ cm, $U_o = 0.17$ m/s, $aD = 4.4$; (C) case 17: $\phi = 0.03$, $D = 22$ cm, $U_o = 0.30$ m/s, $aD = 1.3$; (D) case 10: $\phi = 0.1$, $D = 10$ cm, $U_o = 0.32$ m/s, $aD = 2.0$. Heavyweight dashed lines represent the extrapolation out to $L_1 + L_2$.

the sparse case 17, the length of the sediment formation is $4.5D$ (Fig. 5); $L_1 + L_2 = 25D$, a large disparity, suggesting that the wake length is not a good measure of the sediment pattern for sparse patches. When the wake is very long, as in case 17, the sediment supply provided by erosion near the patch likely runs out before the end of the wake is reached.

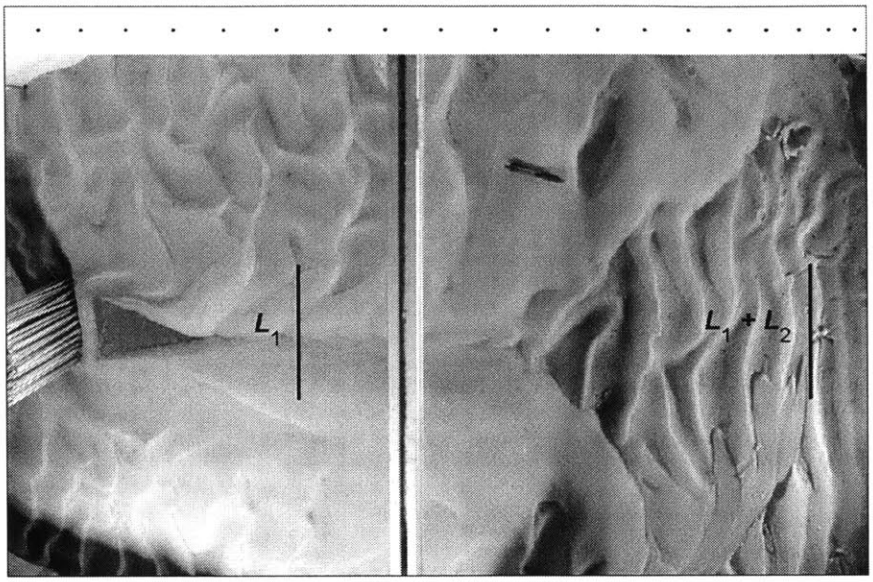

Fig. 6. Panoramic photograph of case 5 ($D = 22$ cm, $\phi = 0.1$, $U_o = 0.17$ m/s). The darker triangular region directly behind the path indicates fine particle deposition. Markers above picture indicate one decimeter of real space, and the first marker is located at $x = 10$ cm. $x = 0$ is the downstream edge of the patch. L_1 and L_2 are marked for reference.

We next consider case 10 (Fig. 5D), for which $D = 10$ cm, $\phi = 0.1$, $aD = 2$. Because $aD < 4$, no recirculation zone is present in the steady wake zone. Consistent with this, this patch does not generate the closed triangular ridge observed in the high flow blockage cases (e.g., cases 4 and 5 in Fig. 5A,B). However, similar to cases 4 and 5, net deposition along the centerline of the wake begins near L_1 (Fig. 5D). Taken together, the four cases shown in Fig. 5 suggest the following generalization: if sediment supply is sufficient, the onset of the von Kármán vortex street at L_1 produces lateral transport toward the wake center and net deposition on the wake centerline beginning near L_1 (cases 4, 5, and 10, Fig. 5A,B,D). For sparse patches with very large L_1, the sediment scoured from around the patch deposits long before the onset of the von Kármán vortex street, and the absence of significant lateral transport within the steady wake leads to downstream deposition that is displaced from the wake centerline (case 17, Fig. 5C).

The distinctive restructuring of the bed shown in Fig. 5 was not observed in every case. If the flow conditions were below the critical value for bedload transport, then no restructuring of the bed could occur. This is also true for the formation of ripples. The bed shear stress, τ, is used to characterize the threshold of sediment motion. From previous literature on bedforms in open channels (Southard, 1991), we expect to find a threshold value (τ_c) above which ripples and bed formations will be observed. In fact, our data suggest this is true, i.e., the same threshold holds for both types of bedform. Specifically, cases for which no ripples were present also have no patch-driven bed formations. The experimental runs fell into three regimes: (1) no ripples and no patch-driven bed forms; (2) no ripples upstream, but ripples triggered by the flow diversion and acceleration around the patch; and (3) ripples and patch-driven bedforms together (e.g., Fig. 6). In regime (3), ripples did not seem to influence the patch-driven formation; no ripples were observed inside the patch. These three regimes are denoted by different symbols in Fig. 7. A distinct transition in regimes occurs near the value $\tau = 0.05$ Pa. Julien (1998, Fig. 7.6) predicted the initiation of sediment motion near $\tau = 0.28 \pm 0.02$ Pa. We are unsure why the observed and predicted thresholds do not match. The addition of stem generated turbulence may play a role, especially within the patch. Further, the diversion of flow enhances the local velocity, which in turn elevates local bed stress above that predicted from U_o. So, local bed stresses are higher than 0.05 Pa at the transition. The data suggest that the critical shear stress is dependent on aD, with a lower transition value occurring for higher aD. This makes sense because, at higher values of aD, more flow is diverted away from the patch, leading to a greater enhancement of velocity outside the patch and a greater local increase in shear rate.

3.4. Within patch scour

In most cases net scour was observed within the patch, and the degree of scour increased with channel velocity (Fig. 8). Note that in our convention scour is negative net deposition, so that a more negative value indicates a greater mean depth of scour within the patch. A linear regression was fit to the low stem density patches ($\phi = 0.03$) and the high stem density patches ($\phi = 0.1$) individually to emphasize the difference between these cases. For the high stem density patches, the patch diameter did not have a significant impact so, for simplicity, these two classes are lumped together. For the same channel velocity (U_o), deeper scour occurred within the higher density patches (black symbols and black trend line in Fig. 8A) than in the

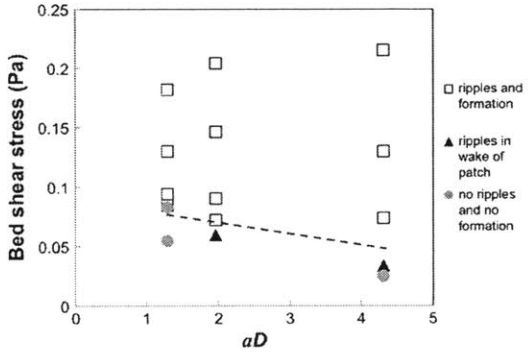

Fig. 7. Classification of cases by bed shear stress (Pa). Ripples and patch-induced formations were not observed for flow conditions with low shear stress but were observed for high bed shear stress. For conditions with intermediate values, ripples were only observed in the patch wake. Error is contained within the symbols. Dashed line represents bed stress transition from conditions that do (above line) and do not (below line) lead to sediment formations.

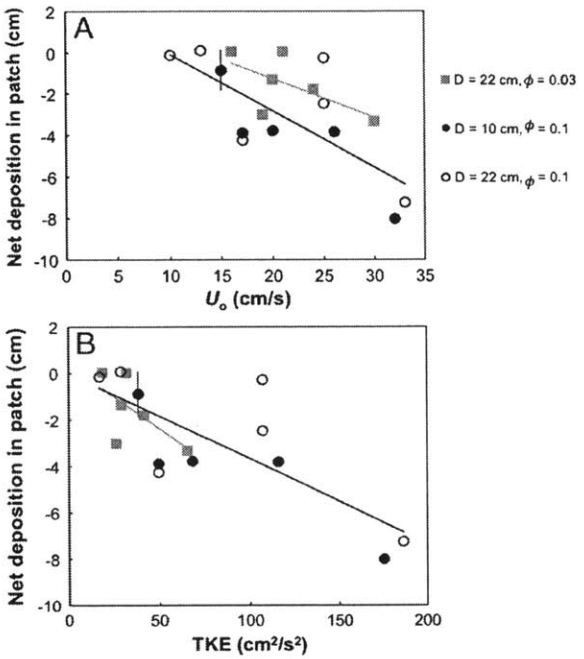

Fig. 8. Net deposition within the patch (cm) versus (A) depth average upstream velocity U_0 (cm/s) and (B) turbulent kinetic energy TKE (cm^2/s^2) estimated from Eq. (4). Black lines show linear trends among $\phi = 0.1$ cases; gray lines show linear trends among $\phi = 0.03$ cases. In most cases, error bars were within the marker size.

lower density patches (grey symbols and grey trend line in Fig. 8A). This is also evident in the comparison shown in Fig. 5: for the same channel velocity, case 4 ($\phi = 0.1$) experienced much deeper in-patch scour than case 17 ($\phi = 0.03$). Increased turbulence generation within the dense patches may be responsible for the increased levels of scour. Using the turbulence level estimated from Eq. (4) as the dependent variable, the measured scour for all patch densities falls on similar trend lines (Fig. 8). This suggests that turbulence level is a better predictor of sediment mobility within the patch than local velocity.

Experiments for which in-patch scour was observed also included a mound of sediment deposition directly behind the patch. This mound consisted, at least in part, of sediment scoured from within the patch. The fraction of in-patch erosion contributing to the mound was estimated as the ratio of mound volume to the volume scoured from within the patch. We only considered cases in which the erosion within the patch was non-zero and net deposition occurred behind the patch. Cases 4 and 10 were omitted because the average net deposition behind the patch was negative owing to scour behind the patch along the sides of the mound (Fig. 5A,D). The mound volume to scour volume ratio decreased as the flow blockage, aD, increased (Fig. 9). To explain this trend, we consider the fraction of flow passing through the patch. Integration of lateral profiles (Zong and Nepf, 2012) indicated that 56% of incoming flow continued through the low flow blockage patch ($aD = 1.3$), while only 19% of incoming flow continued through the high flow blockage patch ($aD = 4.4$). Because the high flow blockage patch has higher flow diversion, which carries away a fraction of the sediment scoured from within the patch, the sediment available to deposit directly behind the patch is reduced. This explains the smaller fraction of mound volume to in-patch scour. The higher flow diversion associated with the denser patch also leads to a greater acceleration at the patch edge, which is reflected in the greater scour depth at the patch edge. For example, compare cases 4 and 17 in Fig. 5, which have similar channel velocity. For case 4 ($aD = 4.4$), the scour on the sides of the patch reached a maximum depth of 7.8 cm, while the deepest point of scour for case 17 ($aD = 1.3$) was 3.5 cm.

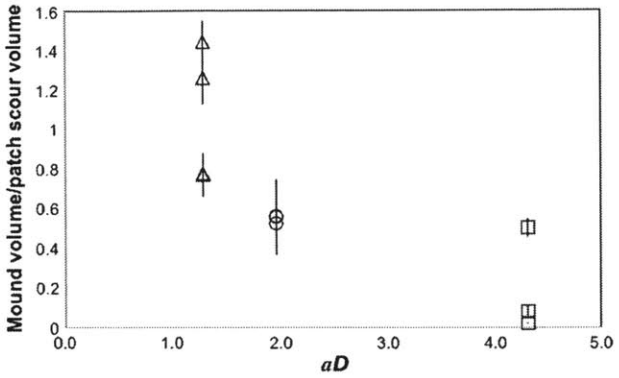

Fig. 9. Ratio of mound volume behind the patch to scour volume within the patch. Mound volume was defined as the volume of sediment deposited in a square area of side length D centered directly behind the patch. △: $\phi = 0.03$, $D = 22$ cm; ○: $\phi = 0.1$, $D = 10$ cm; □: $\phi = 0.1$, $D = 22$ cm.

3.5. Net deposition at reach scale

Finally, we consider whether the introduction of a finite patch of vegetation promotes net deposition at the reach scale. Recall that for a solid cylinder, over a distance $> 10D$, the net change in sediment volume is zero (Dargahi, 1990); i.e., no change in net deposition exists at the reach scale. The channel average net deposition is shown in Fig. 10. Two dashed lines indicate the replicate uncertainty (± 1.1 mm), and any point falling between these lines we consider to be indistinguishable from zero. All but two cases fall within these lines. We can explain case 15, which showed an intrusion of upstream sediment into the laser scan area, probably caused by loosening of the flow straightener upstream, which allowed a stream of relatively fast-moving flow to progress along the side of the flume. In case 5, the predicted $L_1 + L_2$ overestimated the end of the observed patch-driven bedform by about 15 cm (Fig. 6). If we reduce $L_1 + L_2$ by this amount, the channel-scale net deposition is reduced to 1.6 mm. This is still outside the limits for zero net deposition by a margin of 45%. Setting aside this case, the other 16 cases are supportive of the following tentative conclusion. Although significant sediment redistribution is observed, it is spatially contained within the scale of the patch and wake ($L = 2D + L_1 + L_2$), and the introduction of a single patch does not generate net deposition at the reach scale.

4. Discussion

First, let us consider how the vegetation-induced wake may influence the growth pattern for a patch. The bedload transport described in this study and the suspended load deposition observed in this

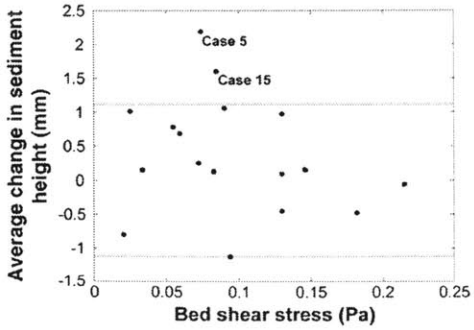

Fig. 10. Average change in sediment height (mm) vs. bed shear stress (Pa) at the reach scale. Variability between ± 1.1 mm (dashed line) represents the estimated uncertainty based on the observations of two sets of replicates.

study and experimentally investigated by Tsujimoto (1999) and Chen et al. (2012) suggest that the wake behind a patch of vegetation is a region of elevated fine particle deposition that is also shaded from significant bedload transport. This would likely make the wake a region of nutrient–rich soil that is favorable for new plant growth, so we expect the patch to grow into the region of the steady wake (L_1). Edwards et al. (1999) and Gurnell et al. (2001, 2008) observed a similar patch growth process leading to a mature streamlined formation in the Tagliamento River, Italy. In this case, spring flooding produced an initial deposit of woody debris on a gravel bar. During subsequent low intensity flow, debris was trapped in the patch wake. Gurnell et al. (2001) and Zong and Nepf (2010) also observed a limited area of fine particle deposition upstream of a patch and attributed this to local flow deceleration.

The enhanced flow at the edges of a finite patch (which induced scour in our experiment) would likely inhibit patch growth in the lateral direction. The regions of high bed shear stress created by flow diversion produced areas of scour in sand with $d_{50}=0.5$ mm. However, in preliminary tests we considered beds of $d_{50}=1.8$ mm. For this larger grain size, no sediment motion occurred around the patches at any of the flow speeds considered. Given this differential in behavior, we anticipated that the diverted flow could selectively transport the finer grains in a graded sediment bed and create an armor layer by leaving only the grains that are too large to be moved by the flow (Carling and Reader, 1982; Jackson and Beschta, 1982; Lisle, 1995). Although fine particle deposition in the steady wake has been proposed as the dominant mechanisms by which a pioneer island expands into a streamlined, elongated formation (Tooth and Nanson, 1999; Gurnell et al., 2001, 2008), armoring of island sides may be an additional mechanism, preventing lateral island expansion. Indeed, Edwards et al. (1999) observed scour similar to that found in our study around islands in the Tagliamento River. Taken together, these processes of deposition and erosion suggest that after a finite patch of vegetation (or woody debris) is introduced, growth of the patch is promoted inline with the patch (mostly downstream, but also upstream); while growth is inhibited in the lateral direction, leading to patches that are elongated in the streamwise direction. Indeed, this is consistent with the shapes observed for instream islands (Gurnell et al., 2001, 2008) and vegetation patches (Sand-Jensen and Madsen, 1992).

Second, the wake behind a patch of vegetation may provide refuge to fish. The wakes of vegetated regions are similar to the wakes of boulders and woody debris in shallow flow, in that the wakes contain regions of low turbulence directly behind the obstruction where wake-scale structures (i.e. the Kármán vortices) are suppressed. For vegetation patches, the Kármán vortices are delayed by the flow through the patch (Zong and Nepf, 2012). In shallow flow conditions, as is typical for boulders, the Kármán vortices are suppressed by the bed friction (Chen and Jirka, 1995; Tritico and Hotchkiss, 2005). Fish prefer these areas of reduced velocity and turbulence because fighting slower currents requires less energy, and these areas often allow fine particle deposition of larvae or macroinvertebrates (Crowder and Diplas, 2000; Roni et al., 2006). Although the literature on fish interaction with vegetation wakes is limited, we suspect that pool-preferring fish will similarly prefer the steady wake zone behind vegetated patches, with the added enticement of prey species activity inside the vegetation patch (Pihl et al., 1994; Collier et al., 1999; Harrison and Harris, 2002). Further, ripples triggered by the patch or areas of scour holes around the patch may provide refuge for small fish (Gerstner, 1998).

Finally, in this study we observed increased scour within the patch with increased stem density. Although this may be somewhat surprising, it is consistent with previous observations. Zong and Nepf (2011) measured flow and fine particle deposition in a long patch of model vegetation. Near the leading edge of the patch, u was close to U_o so that the stem-generated turbulence (Eq. (4)) raised the turbulence levels within the patch above that measured in the adjacent open channel. The elevated levels of turbulence suppressed deposition below that measured for an adjacent bare bed. With the scaling argument that follows, we propose that a good fraction of a circular patch behaves like the leading edge of a long patch, with u close to U_o, so that turbulence will be elevated (relative to the bare bed) over a significant fraction of a circular patch. This elevation of turbulence explains the observed scour.

When flow encounters a long patch of vegetation of width D, the velocity in the patch will decelerate in response to the elevated flow resistance provided by the vegetation. This deceleration occurs within the patch over a length scale L_u, which is roughly equal to the larger of D and a^{-1} (Rominger and Nepf, 2011). Because we only consider patches for which $aD \geq 1$, we reasonably anticipate that $L_u \approx D$. This means that the entire patch length is needed to reach the diminished velocity expected within an extended patch of vegetation, and therefore we can assume $u \approx U_o$ within some non-negligible fraction of the patch. This is true for both sparse and dense patches. Together with Eq. (4) and the observations of Zong and Nepf (2011), we expect that the turbulence level within the circular patch will be elevated, relative to the same flow conditions over a bare bed, which explains the observation of scour.

Similar patterns of scour within circular patches of vegetation have been observed in the field. Bouma et al. (2007) placed dense ($\phi=0.02$, $D=2$ m) and sparse ($\phi=0.001$, $D=2$ m) patches of bamboo canes ($d=6$–8 mm) in a sandy section of an intertidal flat. They observed higher within-patch erosion for the denser patch. The scour began just before the leading edge of the patch and continued about $0.5D$ into the patch, after which sediment accumulation was observed. Bouma's pattern is similar to our observations, except that in our cases the maximum sediment accumulation was always behind the patch rather than inside the patch. This difference could be related to the submerged flow conditions that occurred near high tide in the Bouma study, whereas our study considers only emergent flow conditions.

The result that finite length patches of higher stem density experience greater in-patch erosion stands in contrast to observations in long meadows, for which near-bed turbulence is enhanced within sparse meadows but suppressed within dense meadows (see discussion in Nepf, 2012). For a patch whose length is much greater than L_u, most of the patch experiences fully developed flow. For fully developed flow, the velocity within the patch will depend on the stem density, with u decreasing as n increases. Changes in TKE with increasing stem density then reflect the competing effects of reduced velocity and increased turbulence production (Eq. (4)). These opposing tendencies produce a nonlinear response in which the turbulence levels initially increase with increasing stem density, but decrease as n increases further. So, long sparse canopies experience turbulence that is elevated above the bare bed level, but long dense canopies experience turbulence that is diminished below the bare bed level. The enhancement of near-bed turbulence within sparse meadows can lead to the removal of fines, a process called sandification, while the suppression of near-bed turbulence within dense meadows can lead to a preferential accumulation of fines, a process called muddification (van Katwijk et al., 2010). Similarly, Sand-Jensen (1998) investigated the effect of submerged vegetation on flow and sediment composition in streams. Fine particle deposition was observed in patches dense and long enough to display turbulence suppression, while open streamlined canopies had little effect on flow or sediment.

5. Conclusion

Flow around a circular patch of vegetation creates both deposition and erosion in a pattern that can be linked to the mean and turbulent flow field. None of the conditions considered led to sediment accumulation within the patch, and most of the patches had some degree

of scouring. Scouring increased with increasing stem density, and this trend can be explained by the expected higher level of turbulent kinetic energy within a finite patch of higher stem density. For the lowest flow blockage ($\phi = 0.03$, $aD = 1.3$), 80 to 100% of the sediment scoured from within the patch was deposited within one patch diameter directly behind the patch. Additional deposition occurred farther downstream but at the sides of the wake, creating an open bed formation (e.g., case 17, Fig. 5). For the highest flow blockage ($\phi = 0.1$, $aD = 4.4$), strong flow diversion carried away much of the sediment scoured from within the patch so that the mound directly behind the patch contained <50% of this scoured material and as little as 5%. For $aD = 4.4$ and 2.0, a second region of deposition occurred just beyond L_1, where the action of the von Kármán vortex street directed deposition to the centerline of the wake, creating a closed bed formation (e.g. cases 4, 5, 10, Fig. 5). In all but one case, the redistribution of sediment was contained within the patch and wake length scale $L = 2D + L_1 + L_2$, and over this length scale the patch produced zero net deposition.

Acknowledgments

Research assistance was provided by Lijun Zong, Craig Hill, and Sara Mielke. This work was supported by the STC Program of the National Science Foundation via the National Center for Earth-surface Dynamics under Agreement No. EAR-0120914. This material is based upon work supported by the National Science Foundation under Grant No. EAR 0738352. Any opinions, findings, and conclusions or recommendations expressed in this material are those of the authors and do not necessarily reflect the views of the National Science Foundation.

References

Abt, S., Clary, W.P., Thornton, C.I., 1994. Sediment deposition and entrapment in vegetated streambeds. Journal of Irrigation and Drainage Engineering 120 (6), 1098–1111.

Afzalimehr, H., Dey, S., 2009. Influence of bank vegetation and gravel bed on velocity and Reynolds stress distributions. International Journal of Sediment Research 24 (2), 236–246.

Ball, B.J., Stansby, P.K., Alliston, N., 1996. Modeling shallow water flow around pile groups. Journal of Fluid Mechanics 351, 167–199.

Bennett, S., Pirim, T., Barkdoll, B., 2002. Using simulated emergent vegetation to alter stream flow direction within a straight experimental channel. Geomorphology 44, 115–126.

Bennett, S., Wu, W., Alonso, C.V., Wang, S.Y., 2008. Modeling fluvial response to in-stream woody vegetation: implications for stream corridor restoration. Earth Surface Processes and Landforms 33, 890–909.

Bouma, T.J., van Duren, L.A., Temmerman, S., Claverie, T., Blanco-Garcia, A., Ysebaert, T., Herman, P.M.J., 2007. Spatial flow and sedimentation patterns within patches of epibenthic structures: combining field, flume and modelling experiments. Continental Shelf Research 27 (8), 1020–1045.

Braudrick, C.A., Dietrich, W.E., Leverich, G.T., Sklar, L.S., 2009. Experimental evidence for the conditions necessary to sustain meandering in coarse-bedded rivers. PNAS 106 (40), 16936–16941.

Carling, P.A., Reader, N.A., 1982. Structure, composition and bulk properties of upland stream gravels. Earth Surface Processes and Landforms 7, 349–365.

Chambers, P.A., Prepas, E.E., 1994. Nutrient dynamics in riverbeds—the impact of sewage effluent and aquatic macrophytes. Water Research 28 (2), 453–464.

Chen, D., Jirka, G., 1995. Experimental study of plane turbulent wakes in a shallow water layer. Fluid Dynamics Research 16, 11–41.

Chen, Z., Ortiz, A., Zong, L., Nepf, H., 2012. The wake structure behind a porous obstruction and its implications for deposition near a finite patch of emergent vegetation. Water Research 48.

Collier, K.J., Champion, P.D., Croker, G.F., 1999. Patch- and reach-scale dynamics of a macrophyte–invertebrate system in a New Zealand lowland stream. Hydrobiologia 392, 89–97.

Cotton, J.A., Wharton, G., Bass, J.A.B., Heppell, C.M., Wotton, R.S., 2006. The effects of seasonal changes to in-stream vegetation cover on patterns of flow and accumulation of sediment. Geomorphology 77 (3–4), 320–334.

Crowder, D.W., Diplas, P., 2000. Using two-dimensional hydrodynamic models at scales of ecological importance. Journal of Hydrology 230 (3–4), 172–191.

Crowder, D.W., Diplas, P., 2002. Vorticity and circulation: spatial metrics for evaluating flow complexity in stream habitats. Canadian Journal of Fisheries and Aquatic Sciences 59 (4), 633–645.

Dargahi, B., 1990. Controlling mechanism of local scouring. Journal of Hydraulic Engineering 116 (10), 1197–1214.

Diplas, P., Dancey, C.L., Celik, A.O., Valyrakis, M., Greer, K., Akat, T., 2008. The role of impulse on the initiation of particle movement under turbulent flow conditions. Science 322, 717–720.

Edwards, P.J., Kolmann, J., Gurnell, A.M., Petts, G.E., Tockner, K., Ward, J.V., 1999. A conceptual model of vegetation dynamics on gravel bars of a large alpine river. Wetlands Ecology and Management 7, 141–153.

Fonseca, M.S., Zieman, J.C., Thayer, G.W., 1983. The role of current velocity in structuring eelgrass (*Zostera-marina L.*) meadows. Estuarine, Coastal and Shelf Science 17 (4), 367–380.

Gerstner, C.L., 1998. Use of substratum ripples for flow refuging by Atlantic cod, *Gadus morhua*. Environmental Biology of Fishes 53, 455–460.

Gurnell, A.M., Petts, G.E., Hannah, D.M., Smith, B.P.G., Edwards, P.J., Kollmann, J., Ward, J.V., Tockner, K., 2001. Riparian vegetation and island formation along the gravel-bed Fiume Tagliamento, Italy. Earth Surface Processes and Landforms 26, 31–62.

Gurnell, A.M., van Oosterhout, M.P., de Vlieger, B., Goodson, J.M., 2006. Reach-scale interactions between aquatic plants and physical habitat: River Frome, Dorset. River Research and Applications 22 (6), 1535–1467.

Gurnell, A.M., Blackall, T.D., Petts, G.E., 2008. Characteristics of freshly deposited sand and finer sediments along an island-braided, gravel-bed river: the roles of water, wind, and trees. Geomorphology 99, 254–269.

Habersack, H.M., 2001. Radio-tracking gravel particles in a large braided river in New Zealand: a field test of the stochastic theory of bed load transport proposed by Einstein. Hydrological Processes 15, 377–391.

Harrison, S.S.C., Harris, I.T., 2002. The effects of bankside management on chalk stream invertebrate communities. Freshwater Biology 47, 2233–2245.

Jackson, W.L., Beschta, R.L., 1982. A model of two-phase bedload transport in an Oregon coast range stream. Earth Surface Processes and Landforms 7, 517–527.

Julien, P.Y., 1998. Erosion and Sedimentation. Cambridge University Press, New York, NY.

Kemp, J.L., Harper, D.M., Crosa, G.A., 2000. The habitat-scale ecohydraulics of rivers. Ecological Engineering 16 (1), 17–29.

Kouwen, N., Unny, T.E., 1975. Flexible roughness in open channels. Journal of the Hydraulics Division 101 (NHY1), 194–196.

Larsen, L.G., Harvey, J.W., 2011. Modeling of hydroecological feedbacks predicts distinct classes of landscape pattern, process, and restoration potential in shallow aquatic ecosystems. Geomorphology 126, 279–296.

Lawler, D.M., 2008. Advances in the continuous monitoring of erosion and deposition dynamics: Developments and applications of the new PEEP-3T system. Geomorphology 93 (1–2), 17–39.

Leonard, L.A., Luther, M.E., 1995. Flow hydrodynamics in tidal marsh canopies. Limnology and Oceanography 40 (8), 1474–1484.

Leonard, L.A., Reed, D., 2002. Hydrodynamics and sediment transport through tidal marsh canopies. Journal of Coastal Research S136, 459–469.

Li, S.S., Millar, R.G., 2010. A two-dimensional morphodynamic model of gravel-bed river with floodplain vegetation. Earth Surface Processes and Landforms 36 (2), 190–202.

Lisle, T.E., 1995. Particle size variations between bed load and bed material in natural gravel bed channels. Water Resources Research 31 (4), 1107–1118.

Lopez, F., Garcia, M., 1998. Open-channel flow through simulated vegetation: suspended sediment transport modeling. Water Resources Research 34 (9), 2341–2352.

Luna, Marco, C. M. de M., Parteli, E.J.R., Durán, O., Herrmann, H.J., 2011. Model for the genesis of coastal dune fields with vegetation. Geomorphology 129, 215–224.

Mars, R., Mathew, K., Ho, G.E., 1999. The role of the submergent macrophyte *Triglochin huegelii* in domestic greywater treatment. Ecological Engineering 12 (1–2), 57–66.

Nepf, H.M., 2012. Flow and transport in regions with aquatic vegetation. Annual Review of Fluid Mechanics 44, 123–142.

Nicolle, A., Eames, I., 2011. Numerical study of flow through and around a circular array of cylinders. Journal of Fluid Mechanics 679, 1–31.

Pihl, L., Wennhage, H., Nilsson, S., 1994. Fish assemblage structure in relation to macrophytes and filamentous epiphytes in shallow non-tidal rocky- and soft-bottom habitats. Environmental Biology of Fishes 38, 271–288.

Pollen, N., Simon, A., 2005. Estimating the mechanical effects of riparian vegetation on stream bank stability using a fiber bundle model. Water Resources Research 41 (7), W07025.

Pollen-Bankhead, N., Simon, A., 2010. Hydrologic and hydraulic effects of riparian root networks on streambank stability: is mechanical root-reinforcement the whole story? Geomorphology 116 (3–4), 353–362.

Rominger, J.T., Nepf, H.M., 2011. Flow adjustment and interior flow associated with a rectangular porous obstruction. Journal of Fluid Mechanics 680, 636–659.

Rominger, J.T., Lightbody, A.F., Nepf, H.M., 2010. Effects of added vegetation on sand bar stability and stream hydrodynamics. Journal of Hydraulic Engineering 136 (12), 994–1002.

Roni, P., Bennett, T., Morley, S., Pess, G.R., Hanson, K., van Slyke, D., Olmstead, P., 2006. Rehabilitation of bedrock stream channels: the effects of boulder weir placement on aquatic habitat and biota. River Research and Applications 22, 967–980.

Sand-Jensen, K., 1998. Influence of submerged macrophytes on sediment composition and near-bed flow in lowland streams. Freshwater Biology 39 (4), 663–679.

Sand-Jensen, K., Madsen, T.V., 1992. Patch dynamics of the stream macrophyte, *Callitriche cophocarpa*. Freshwater Biology 27 (2), 277–282.

Schulz, M., Kozerski, H.P., Pluntke, T., Rinke, K., 2003. The influence of macrophytes on sedimentation and nutrient retention in the lower River Spree (Germany). Water Research 37 (3), 569–578.

Simpson, R.L., 2001. Junction flows. Annual Review of Fluid Mechanics 33, 415–443.

Southard, J.B., 1991. Experimental determination of bed-form stability. Annual Review of Earth and Planetary Sciences 19, 423–455.

Tal, M., Paola, C., 2007. Dynamic single-thread channels maintained by the interaction of flow and vegetation. The Geological Society of America 35 (4), 347–350.
Tanino, Y., Nepf, H.M., 2008. Lateral dispersion in random cylinder arrays at high Reynolds number. Journal of Fluid Mechanics 600, 339–371.
Tooth, S., Nanson, G.C., 1999. Anabranching rivers on the northern plains of arid central Australia. Geomorphology 29 (3–4), 211–233.
Tritico, H.M., Hotchkiss, R.H., 2005. Unobstructed and obstructed turbulent flow in gravel bed rivers. Journal of Hydraulic Engineering 131 (8), 635–645.
Tsujimoto, T., 1999. Fluvial processes in streams with vegetation. Journal of Hydraulic Research 37 (6), 789–803.
van Katwijk, M.M., Bos, A.R., Hermus, D.C.R., Suykerbuyk, W., 2010. Sediment modification by seagrass beds: muddification and sandification induced by plant cover and environmental conditions. Estuarine, Coastal and Shelf Science 89 (2), 175–181.
Wang, C., Yu, J.Y., Wang, P.F., Guo, P.C., 2009. Flow structure of partly vegetated open-channel flows with eelgrass. Journal of Hydrodynamics 21 (3), 301–307.
Wilcock, R.J., Champion, P.D., Nagels, J.W., Crocker, G.F., 1999. The influence of aquatic macrophytes on the hydraulic and physico-chemical properties of a New Zealand lowland stream. Hydrobiologia 416, 203–214.
Wynn, T.M., Mostaghimi, S., 2006. Effects of riparian vegetation on stream bank subaerial processes in southwestern Virginia, USA. Earth Surface Processes and Landforms 31 (4), 399–413.
Zong, L., Nepf, H.M., 2010. Flow and deposition in and around a finite patch of vegetation. Geomorphology 116, 363–372.
Zong, L., Nepf, H.M., 2011. Spatial distribution of deposition within a patch of vegetation. Water Resources Research 47, W03516.
Zong, L., Nepf, H.M., 2012. Vortex development behind a finite porous obstruction in a channel. Journal of Fluid Mechanics 691, 368–391.

Chapter 3

Particle retention in a submerged meadow and its variation near the leading edge

Abstract

The retention of particles within a meadow of submerged aquatic vegetation (SAV) impacts the fate of suspended particles in marine systems, including organic matter, pollen, and larvae. Because flow conditions near the leading edge differ from those over the bulk of the canopy, the particle retention is likely to differ as well. Specifically, near the leading edge, current entering the meadow is decelerated over a distance of several meters, called the adjustment length-scale. In a wide meadow, this deceleration triggers a vertical updraft that has a maximum at the leading edge and decays over the adjustment length-scale. After the decay of the vertical updraft, the velocity profile evolves into an obstructed shear layer. Within the fully-developed canopy flow region, the upper canopy is flushed by canopy scale vortices, while the turbulence in the lower canopy is dominated by blade scale vortices. In this study we measured the retention of particles along the 10-m length of a model meadow (height $h = 0.1$m) and connect the trends in retention to the evolving flow field. Two sizes of silica particles, with settling velocity $w_{s50} = 0.00075, 0.021$ m/s, were released at two depths $\left(\frac{z_{rel}}{h} = 0.31, 0.81\right)$. The retention of particles was measured using microscope slides distributed along the bed of the flume. Retention increased with distance from the leading edge, reaching a maximum at the adjustment length-scale. Particle retention was greater for the particles with higher settling velocity. In the fully developed region, particle retention was lower for particles released in the upper canopy ($\frac{z_{rel}}{h} = 0.31$), where canopy scale vortices could enhance particle escape.

Keywords: particle transport, leading edge, capture, initial adjustment region, velocity ratio

3.1. Introduction

Suspended particles respond to the flow structure within and around aquatic vegetation, creating distinct patterns of deposition that influence the potential for future meadow growth and resilience (Sand-Jensen, 1998, Gurnell et al., 2001, 2008, Hughes and Stachowicz 2004, van Katwijk et al., 2016). Submerged aquatic vegetation, such as seagrasses, are foundational species of coastal habitats. Dense meadows stabilize sediment, lowering turbidity and sequestering carbon stocks, and increase biodiversity by providing sheltered regions (van Katwijk et al., 2016). The deposition of particles in and around vegetated regions has been previously investigated in the field and by laboratory experiments. For example, dense seagrass meadows have been observed to increase sedimentation and reduce resuspension relative to bare bed regions (Ward et al., 1984, Gacia et al., 1999, Terrados and Duarte, 2000, Gacia and Duarte, 2001, Agawin and Duarte, 2002), while erosion and resuspension have been observed in sparse meadows (Luhar et al., 2008, van Katwijk et al. 2010, Lawson et al., 2012). Enhanced fine particle deposition has also been observed in the wake of finite patches of vegetation (Gurnell et al., 2001, Tanaka and Yagisawa, 2010, Chen et al., 2012), while diminished deposition has been observed near the leading edge of emergent canopies (Zong and Nepf, 2010). In this paper we consider the retention of particles released in a long submerged meadow, making connections between the observed deposition and the flow structure at the leading edge and in the fully-developed regions of the meadow.

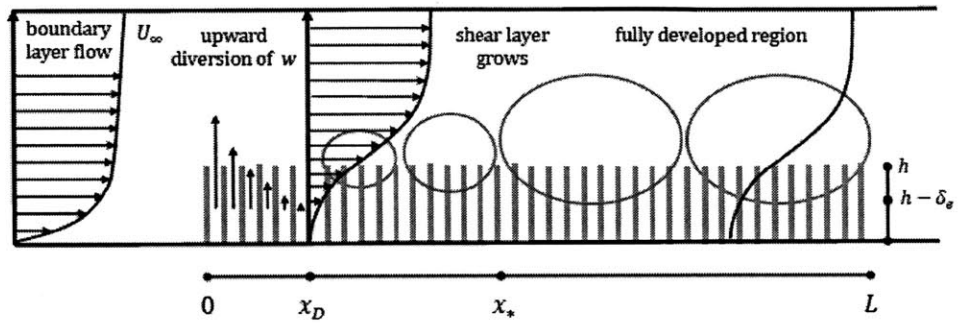

Figure 1 Schematic of the flow adjustment from flow over a bare bed to flow over submerged vegetation. The flow depth is H and the canopy height is h. Starting at the leading edge ($x = 0$), flow decelerates creating an updraft over length x_D. Beyond this adjustment length, the mixing layer grows and becomes fully developed at x_*, after which point the friction velocity at the top of the canopy (u_*) reaches a constant value. The characteristic vortex penetration in the fully developed region is δ_e.

Flow evolution over a submerged meadow is depicted in Figure 1. The streamwise and vertical coordinates are (x, z) and the corresponding velocity vector is $\vec{u} = (u, w)$, with $x = 0$ at the leading edge and $z = 0$ at the bed, and positive in the upward direction. Current entering the meadow at the leading edge is decelerated over a distance called the adjustment length-scale (Chen et al., 2013). In a meadow with width (B) much greater than height ($B \gg h$), this deceleration triggers a vertical updraft that has a maximum at the leading edge ($x = 0$) and decays exponentially over the adjustment length-scale, x_D (Belcher et al., 2003, Chen et al., 2013). The adjustment length, x_D, scales with the canopy drag length scale L_c (Belcher et al., 2003, Chen et al., 2013):

$$L_c = \frac{2(1-\phi)}{C_D a} \quad (1)$$

60 in which ϕ is the canopy solid volume fraction, C_D is the canopy drag coefficient, and a is the
61 frontal area per canopy volume. The adjustment length is

62 $$\frac{x_D}{L_c} = \beta(1 + \alpha C_D a h) \quad (2)$$

63 with scale factors $\alpha = 2.3 \pm 0.2$ and $\beta = 1.5 \pm 0.2$ determined from a range of terrestrial and
64 aquatic canopies with submergence ratios $H/h = 2$ to ∞ (Chen et al., 2013). A shear layer
65 profile (Figure 1) begins to take shape within the adjustment region, as flow above the canopy
66 accelerates and flow within the canopy decelerates. However, the development of the shear-
67 layer coherent structures at the top of the canopy (Raupach et al., 1996, Ghisalberti and Nepf,
68 2002) is constrained within the adjustment region by the vertical updraft (Irvine et al., 1997,
69 Morse et al., 2002). Beyond x_D, the shear-scale structures develop and grow with distance from
70 the leading edge, eventually reaching a constant size and strength at a distance x_* (Ghisalberti
71 and Nepf, 2002, Ghisalberti and Nepf, 2004). Beyond x_*, the mixing layer is considered fully
72 developed. Once fully developed, the shear layer vortices penetrate into the canopy a distance
73 $\delta_e = {}^{0.23}/_{C_D a}$ (Nepf et al., 2007). Turbulence in the upper canopy ($z > h - \delta_e$) is dominated
74 by the shear-layer vortices, which have velocity scale u_*. In the lower canopy ($z \leq h - \delta_e$),
75 below the penetration of the shear layer vortices, turbulence is locally generated in the wakes
76 of the individual shoots (Nepf and Vivoni, 2000).

77 In this study we measure the retention of particles within the leading edge and fully
78 developed region of a 10 m long canopy composed of rigid dowels, making connections to the
79 leading edge and fully developed flow structure described above. The particles were injected at

80 different longitudinal locations to assess how the evolving velocity field impacted particle
81 retention.

82

83 **3.2. Methods**

84 Experiments were conducted using a rigid, model canopy that was 10 m long, $h = 0.1$
85 m tall and spanned the width ($B = 0.38$ m) of a recirculating flume. The model canopy was
86 constructed of circular wooden rods ($n = 0.077$ rods/cm^2 bed $a = nd = 5$ m^{-1}, $d = 0.65$ cm).
87 Using $C_D = 1$, δ_e/h =0.46. For circular cylinders $\phi = \frac{\pi}{4}ad$ = 0.026. The three components of
88 velocity were recorded using an acoustic Doppler velocimeter (ADV, Nortek Vectrino). Each
89 records was collected for 4 minutes at 25 Hz. Silica seeding particles (Sphericel 110P8, Potters
90 Industries, Malvern, PA) were added to the water to enhance the ADV signal. Longitudinal
91 transects with 10-cm intervals were made at y/B = ¼ and at three vertical positions: above
92 (z/h =0.81, 1) and below ($z/h = 0.31$) the penetration distance of the canopy scale vortices,
93 δ_e/h =0.46. In addition, a lateral profile was recorded within the fully developed region
94 ($x > x_*$). For each measurement the ADV was centered between the staggered dowels in such
95 a way that the longitudinal velocity, vertical velocity, and Reynolds stresses were close to the
96 lateral average value over the element spacing (as described in Chen et al., 2013, Figure 2d in
97 that paper). The velocity records were decomposed into time average and fluctuating
98 components ($u = \bar{u} + u'$), respectively denoted by an overbar and prime. The Reynolds stress
99 ($-\overline{u'w'}$) was found by multiplying and subsequently time averaging the vertical and

longitudinal fluctuations. The turbulent kinetic energy was calculated as $TKE = \frac{1}{2}\left(\overline{u'^2} + \overline{v'^2} + \overline{w'^2}\right)$. The friction velocity at the top of the canopy was defined as $u_* = \sqrt{-\overline{u'w'}_{z=h}}$.

The influence of the leading edge flow development on particle fate was assessed by conducting a series of particle releases within the adjustment region and within the fully-developed region of the model canopy. Releases were done at two heights: within the upper canopy, where the particles were impacted by canopy-scale vortices ($z > h - \delta_e$) and below the penetration of the canopy scale vortices ($z \leq h - \delta_e$). Two sizes of silica particles (Potters Industries, Malvern, PA) were released inside the canopy and deposited on glass microscope slides. The particle size distribution was measured using laser diffraction (Beckman Coulter, Table 1). The settling velocity was found using Stokes' law ($w_s = \frac{g(\rho_p - \rho_w)\left(\frac{d}{2}\right)^2}{18\mu}$), with $\rho_p = 2500$ kg/m^3, ρ_w= 1000 kg/m^3,μ = 8.9e-4 kg/ms. The heavier particles (Spheriglass A2024, $w_{s50} =$ 0.021 m/s) were chosen to have settling velocity comparable to the shear velocity at the top of the canopy (u_*= 0.013 m/s), while the lighter particles (Spheriglass E3000, $w_{s50} = 0.00075$ m/s) were chosen to have a settling velocity smaller than u_*..

E3000: %	d (μm)	w_s (m/s)	A2024: %	d (μm)	w_s (m/s)
10	4.8	$2.1 * 10^{-5}$	10	130	$1.6 * 10^{-2}$
25	13	$1.6 * 10^{-4}$	25	140	$1.8 * 10^{-2}$
50	29	$7.5 * 10^{-4}$	50	150	$2.1 * 10^{-2}$
75	50.	$2.3 * 10^{-3}$	75	170	$2.6 * 10^{-2}$
90	77	$5.4 * 10^{-3}$	90	180	$3.0 * 10^{-2}$

115 **Table 1** Diameter and settling velocities of lighter (E3000) and heavier (A2024) particles. Values
116 are shown for the 10, 25, 50, 75, and 90th percentiles. Particle size distribution measured using
117 laser diffraction (Beckman Coulter).

118 Particles were injected into the canopy at different longitudinal locations within the
119 leading edge and the fully developed region ($x/h = 0, 2.4, 5, 13.7, 53.3$). Before the
120 experiment, 60 glass microscope slides (2.5" x 7.5") were labeled and weighed. The slides
121 (oriented with long side perpendicular to the mean flow) were placed in rows with centers at
122 $y/B = 0.25, 0.5, 0.75$, with rows at 20 streamwise locations. The rows were concentrated
123 immediately downstream of the injection location, but also with several rows upstream and far
124 downstream of the injection. Silica particles were mixed with water to form a dilute solution
125 (E3000: 175 g silica in 10L water; A2024: 75 g silica in 10L water). A smaller mass of A2024 was
126 released to prevent losses due to particles rolling off the slides, which occurred when large
127 initial masses were used. The particle/water solution was continually mixed by hand in a 5
128 gallon plastic bucket and injected through a 2 mm nozzle into the flume using a peristaltic
129 pump (Manostat Preston, Barrington, IL). The injection took one hour, which was long
130 compared to the timescale of the shear-layer vortices (10 s) and the flume recirculation time (5
131 minutes). The tubing was taped to a rigid rod inside the flume and attached to a two-way nozzle
132 pointing in the $\pm y$ directions, so that the plume was swept forward by the longitudinal flow,
133 minimizing effects of a mismatch between the injection and local velocity. After the injection,
134 the flume was slowly drained and the slides were allowed to dry for several days. After the
135 initial drying period, the slides were removed from the flume using tweezers. Slides with heavy
136 deposition were placed in aluminum boats to reduce particle loss. The slides were dried in an
137 oven (VWR) for one day. After drying, the slides were reweighed and the difference in weights

was assumed to be entirely due to the settled particles. Two blank experiments measuring the change in slide weight with no particles released determined that there was a negligible amount of other material in the flume water, $\Delta slide = 0.0004g \pm 0.0011$ (SD).

In order to estimate the total deposition within the model canopy, it was necessary to interpolate values of deposition in between the slides and the flume walls ($y = 0 - 5.75$ cm, $32.25 - 38$ cm). Based on visual inspection after the flume was drained and dried, the particle deposition was observed to be concentrated near the center of the flume. Particle deposition was observed to extend to the walls for E3000 particles, and to be zero at the walls for the heavier A2024 particles. Based on this, the deposition of E3000 particles at the side walls was assumed to be the average of the outermost slides, and deposition of A2024 particles was assumed to decrease linearly from the deposition measured on the outermost slides to 0 at the walls. The fraction of particles released that deposited within the canopy was then calculated as

$$F_{dep} = \frac{1}{M_{tot}} \iint (M_{slide} - M_{upstream}) dxdy \quad (3)$$

Where M_{tot} is the total mass of particles added to the slurry, M_{slide} is the measured deposition per cm^2 on an individual slide and $M_{upstream}$ is the average deposition per cm^2 of all upstream slides due to recirculated particles measured upstream of the injection site. The deposition within the region covered by each slide was assumed to be the average value of the deposition on the slide. Linear interpolation was used to estimate deposition outside of the region covered by the slides (Figure 2). The integration was approximated by trapezoidal sums. In order to evaluate uncertainty, replicate experiments were conducted for four of the releases (see Table

158 2) The difference between the replicate experiments was greater than the uncertainty from the

159 standard error on $M_{upstream}$, so the replicate error was used as the estimate of uncertainty.

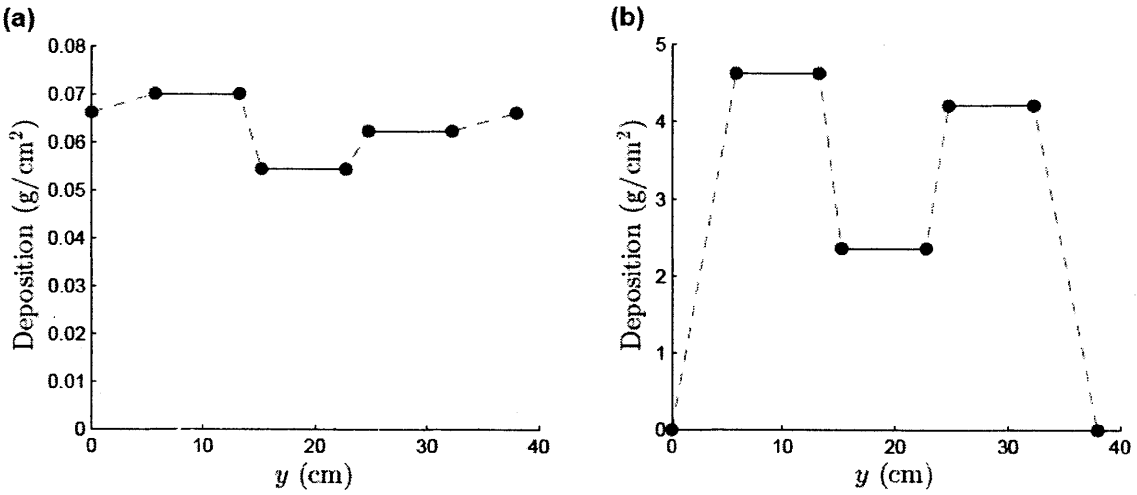

160

161 **Figure 2** Lateral profile of (a) E3000 deposition (g/cm^2) measured at x/h = 54.1 and (b) A2024
162 deposition(g/cm^2) measured at x/h = 53.8. Deposition was measured on 3 glass slides covering
163 the flume bed over y = 5.75-13.25 cm, 15.25-22.75 cm, and 24.75-32.25 cm. Deposition of
164 E3000 particles at the side walls of the flume was assumed to be the lateral average of the two
165 outer slides, based on visual observation that the deposition extended to the flume sides. For
166 the heavier A2024 particles, deposition was assumed to be 0 at the side walls of the flume,
167 based on visual observation. The deposition within the region covered by each slide (solid lines)
168 was assumed to be uniform with the average value of the deposition on the slide. Linear
169 interpolation (dashed lines) was used to estimate deposition outside of the region covered by
170 the slides.

171

172 **3.3. Results**

173 The velocity measurements were used to evaluate the length of the adjustment region, x_D, and

174 the distance to the fully developed region, x_*, which we used to select the release locations.

175 The time-mean longitudinal ($\overline{u}$) and vertical ($\overline{w}$) velocity decreased with distance from the

176 leading edge ($0 < x/h < x_D/h$, Figure 3 a,b). Based on the drag length scale ($L_c = 0.4$ m^{-1}, eq.

1, assuming C_D =1), we expected the adjustment region to end at $x_D/h = 13$ (eq. 2), which is denoted with a black vertical line in Figure 3. The vertical velocity had decayed to zero by this point (Figure 3b). Within the adjustment region ($x\ /h < x_D/h$) the Reynolds stress remains small (Figure 3c), but begins to increase beyond x_D, indicating the development of the shear layer and associated vortices. The Reynolds stress reached a constant value in the fully developed region ($x/h > x_*/h = 30$). The shear velocity at the top of the canopy ($u_* = 0.013$ m/s) was estimated from a lateral transect made in the fully developed region. In the fully developed region ($x/H\ > 30$) the turbulent stresses measured in the upper canopy (z/h = 0.81 and 1) are much higher than those measured in the lower canopy ($z/h\ = 0.31$), reflecting the limited penetration of turbulence into the canopy, and specifically the fact that the shear-layer vortices do not penetrate to the lower canopy.

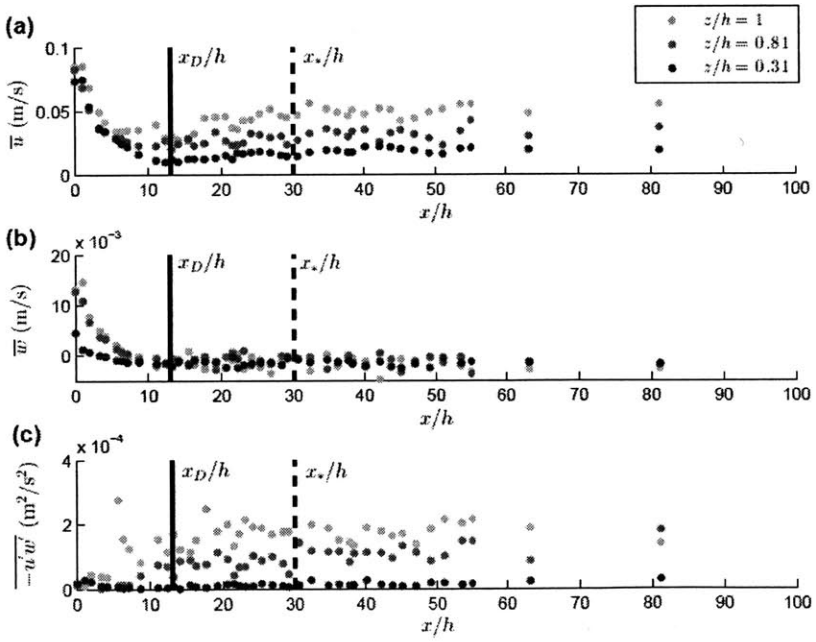

Figure 3 Longitudinal profiles showing (a) the time-averaged longitudinal velocity (m/s), (2) time-averaged vertical velocity (m/s), and (c) Reynolds stresses (m^2/s^2) at z/h =1, 0.81, and 0.31 (light gray, medium gray, and black dots). The length of the initial adjustment region, $x_D/h = 13$, is shown with a solid vertical line. The beginning of the fully developed region, $x_*/h = 20$, is shown with a dashed vertical line. The longitudinal transects were located above (z/h =0.81, 1, medium and light gray dots) and below ($z/h = 0.31$, dark grey dots) the penetration distance of the canopy scale vortices, δ_e/h =0.46. At some locations, the vertical velocity showed a slight negative value (≥-0.5 cm/s), which we attributed to the influence of acoustic streaming of the ADV acoustic pulses (Poindexter et al., 2011).

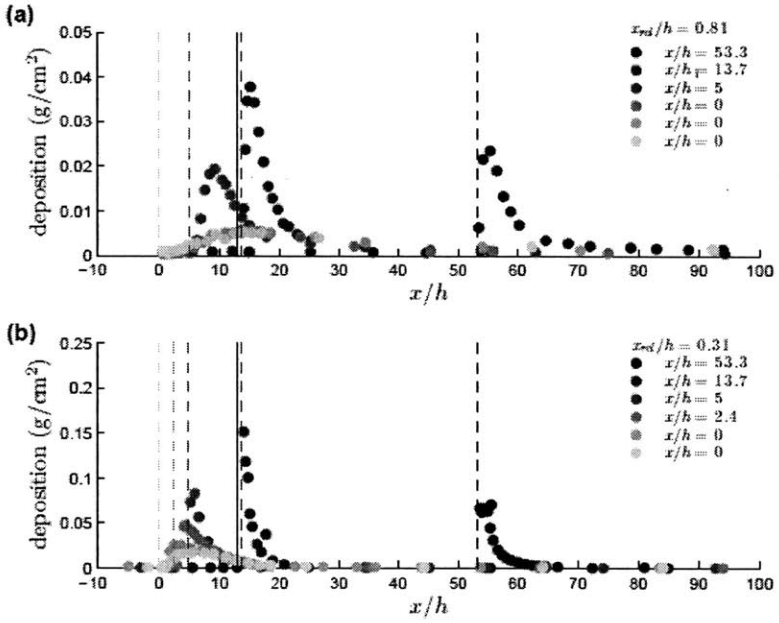

Figure 4 Longitudinal (x/h) patterns of deposition (g cm^{-2}) created by injections at nine locations within the canopy. Silica particles ($w_{s50} = 0.00075$ m/s were released at (a) $z_{rel}/h = 0.81, \frac{x_{rel}}{h} = 0, 5, 13.7, 53.3$ and (b) $\frac{z_{rel}}{h} = 0.31, \frac{x_{rel}}{h} = 0, 2.4, 5, 13.7, 53.3$. The dashed vertical lines indicate the longitudinal injection position. The solid vertical line denotes position of x_D/h.

Particles were released within the adjustment region near the leading edge ($x_{rel}/h =$ $0, 2.4, 5, 13.7$), and within the fully developed region ($x_{rel}/h = 53.3$). Releases were

conducted at two heights ($z_{rel}/h = 0.81,0.31$), above and below the vortex penetration distance $\left(z/h = 1 - \frac{\delta_e}{h} = 0.54\right)$. The shape and size of the deposition region changed across the adjustment region, due to the influence of the vertical updraft. For the releases at $x_{rel}/h = 0$ (Figure 4a,b light gray dots), 98% of the particles had settling velocity less than the values of $\overline{w}$ at the release point ($\overline{w} = 0.015, 0.013$ m/s, at $z_{rel}/h = 0.81$ and 0.31, respectively). The location of maximum deposition did not occur immediately after the release point, but at 250 ± 40 cm and 80 ± 10 cm downstream (for $z_{rel}/h = 0.81$, 0.31, respectively). The particles were initially carried upward by the updraft, and settled after the upward diversion had decayed, i.e. at $x_D = 130$ cm, which is indicated in Figure 4. For releases in which the updraft was weaker near the release point ($x_{rel}/h = 5$, $z_{rel}/h = 0.81$, $\overline{w} = 0.0022$ m/s, Figure 4a; $x_{rel}/h = 2.4$, $z_{rel}/h = 0.31$, $\overline{w} = 0.0005$ m/s, Figure 4b), the settling velocity of 73% and 42%, of the particles, respectively, was greater than the updraft. The distance between the point of release and the location of maximum deposition, L_{max}, was smaller than the value for releases at the leading edge and L_{max} decreased as the release point moved away from the leading edge (Table 2).

(a)

$z_{rel}/h = 0.81$

x_{rel}/h	0	5	13.7	53.3
$\overline{w}$ m/s	0.0128	0.0022	-0.0010	-0.0004
$x_{1/2}$ m	2.5 ± 0.4	0.78	0.39	0.54 ± 0.07
L_{max} m	1.5 ± 0.1	0.42	0.14	0.23 ± 0.03

(b)

$z_{rel}/h = 0.31$

x_{rel}/h	0	2.4	5	13.7	53.3
$\overline{w}$ m/s	0.0046	0.0005	-0.0006	-0.0015	-0.0015
$x_{1/2}$ m	0.80 ± 0.1	0.47	0.23	0.15	0.19 ± 0.01
L_{max} m	0.50 ± 0.1	0.2	0.11	0.03	0.12 ± 0.09

Table 2 Updraft ($\overline{w}$) at release point, distance over which half of the total deposition occurred ($x_{1/2}$), and distance between release and the point of maximum deposition for releases of spherical silica particles ($w_{s50} = 0.00075$ m/s) at (a) $z_{rel}/h = 0.81$, $x_{rel}/h = 0,5,13.7,53.3$ and (b) $z_{rel}/h = 0.31, x_{rel}/h = 0,2.4,5,13.7,53.3$. The standard error ($\pm 1SE$) was found from replicate experiments at x_{rel}/h =0,53.3. The standard error of the experiments at x_{rel}/h =2.4,5, 13.7 was assumed to be the average of the replicate error at x_{rel}/h =0,53.3 ($\overline{SE} = 6$, z_{rel}/h =0.31; $\overline{SE}$ =23, $z_{rel}/h = 0.81$).

As the updraft decayed with distance from the leading edge, the shape of the deposition mound also changed; the peak deposition became higher and the region of deposition shortened as the vertical velocity at the release point was diminished (Figure 4). The distance over which half of the measured deposition occurred ($x_{1/2}$) was longest for the releases in which the vertical updraft was strongest and shortened as the release points moved farther from the leading edge, until reaching the end of the adjustment zone, i.e. $x_{rel}/h = 13.7 \approx x_D/h$ (Table 2). For the release point at x_D the deposition pattern was shortest, because at this point, the upward diversion had decayed to 0 (Figure 3b), and the contribution from the shear-layer vortices was still small, as reflected in Reynolds stress values that are smaller than in the fully developed region ($x/h < x_*/h$, Figure 3c). For releases that occurred within the upper

canopy ($z_{rel}/h = 0.81$) within the fully developed region, $x_{1/2}$ increased relative to its value at x_D, due to the higher turbulence values (Figure 4b) associated with the fully developed canopy scale vortices.

The fraction of released particles (F_{dep}) that deposited to the bed (and were thus retained in the canopy) was calculated using eq. (3). F_{dep} was lowest for particles released at the leading edge, $x_{rel}/h = 0$, and increased with distance from the leading edge for release points within the initial adjustment region, reaching a maximum at x_D/h (Figure 5c). This is consistent with the expected influence of the updraft associated with the leading edge, which is maximum at the leading edge and decays to zero at x_D (Figure 5a). The updraft pulls particles out of the canopy, reducing the deposition. Beyond x_D/h, i.e. within the fully-developed region, F_{dep} decreased for releases at z_{rel}/h =0.81, due to the influence of the canopy scale vortices entraining particles and drawing them out of the canopy (Figure 5b). For all release locations, the release lower in the canopy at z_{rel}/h =0.31 had greater deposition than the release at z_{rel}/h =0.81. In addition to the shorter distance from the point of release to the bed, the TKE values at z_{rel}/h =0.81 were higher than the values at z_{rel}/h =0.31 at x_{rel}/h =13.7, 53.3, providing an additional mechanism of escape from the canopy.

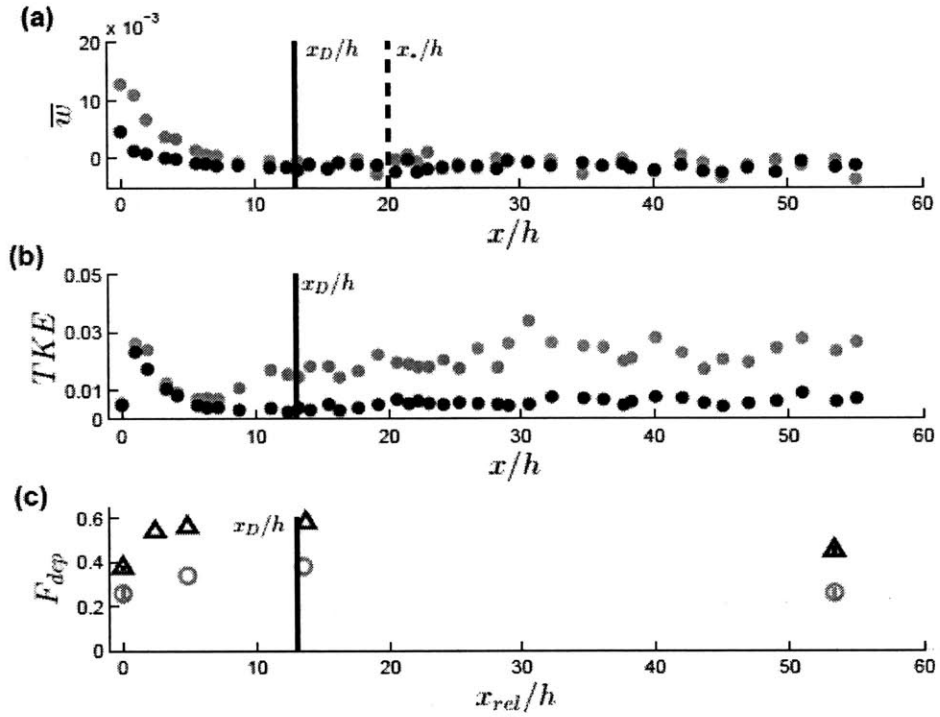

259

260 **Figure 5** (a) Longitudinal profile of the vertical velocity $\overline{w}$ at two measurement heights over the
261 model canopy (z/h =0.31,0.81, black and grey solid circles), (b) Longitudinal profile of the
262 turbulent kinetic energy at two measurement heights over the model canopy (z/h =0.31, 0.81,
263 black and grey solid circles), (c) Fraction of released particles ($w_{s50}/u_* = 0.058$) that deposited
264 to the bed for two release heights ($z_{rel}/h = 0.31$, black open circles; $z_{rel}/h = 0.81$, gray open
265 circles). The vertical lines on the points at x_{rel}/h =0,53.3 denote the difference between two
266 replicates, as measured from repeat experiments at these positions. The standard error of the
267 experiments at x_{rel}/h =2.4,5, 13.7 was assumed to be the average of the replicate error at
268 x_{rel}/h =0,53.3 ($\overline{SE} = 0.013$, z_{rel}/h =0.31; $\overline{SE}$ =0.03, $z_{rel}/h = 0.81$)

269

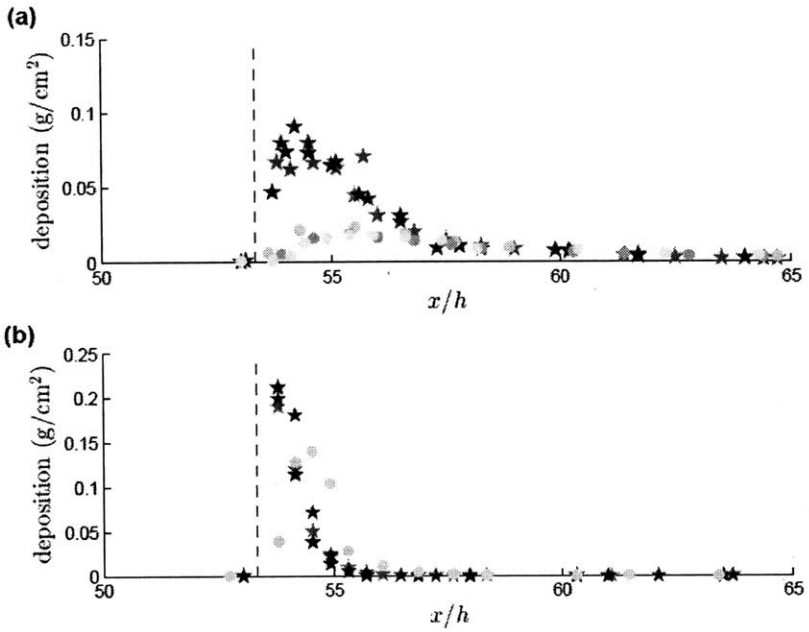

Figure 6 Deposition (g cm^{-2}) of two sizes of silica particles: (a) $w_{s50}/u_* = 0.058$ (E3000, circles) and (b) $w_{s50}/u_* = 1.6$ (A2024, stars) that were injected within the fully developed region of the model canopy ($x_{rel}/h = 53.3$). Particles were injected above $z = h - \delta_e$ ($z_{rel}/h = 0.81$, light gray), in the region routinely flushed by canopy scale vortices, and below $z = h - \delta_e$ ($z_{rel}/h = 0.31$, dark gray and black), in the region characterized by stem-scale vortices. Three replicates of the lighter particles (a) were released below $z = h - \delta_e$ (black and grey stars) and above $z = h - \delta_e$ (grey circles). Three replicates of the heavier particles were released below δ_e (black and grey stars), and one release was conducted above δ_e (grey circles)

Finally, in order to test the impact of settling velocity on particle deposition, two particle sizes ($w_{s50}/u_* = 0.058, 1.6$) were released in the fully developed region (Figure 6). The release points were above and below the maximum penetration of the canopy scale vortices ($z = h - \delta_e$), so that the canopy scale vortices routinely flushed the higher release point, while the turbulence near the lower release point, dominated by stem scale vortices, was of lower intensity (Figure 5b). The lighter particles (E3000) had a settling velocity about one order of magnitude less than the canopy shear velocity, so that the particle transport was expected to

287 be influenced by the canopy turbulence. A higher fraction of light particles deposited to the bed
288 from the release at $z_{rel}/h = 0.31$ than the release at $z_{rel}/h = 0.81$ (Figure 6, $F_{dep} = 0.45 \pm$
289 0.03, $z_{rel}/h = 0.31$, $F_{dep} = 0.26 \pm 0.04$ (SE), $z_{rel}/h = 0.81$). In addition, the deposition
290 occurred over a shorter distance for the release at $z_{rel}/h = 0.31$ than for the release at
291 $z_{rel}/h = 0.81$ ($x_{1/2} = 19 \pm 1, 54 \pm 7$m), respectively. In contrast, F_{dep} of heavier particles
292 (A2024) was the same, within error, for the release at $z_{rel}/h = 0.31$ and the release at
293 $z_{rel}/h = 0.81$ (Figure 6, $F_{dep} = 0.79 \pm 0.07$ (SE), $z_{rel}/h = 0.31$, $F_{dep} = 0.82$, $z_{rel}/h = 0.81$).

294 **3.4. Discussion**

295 The experimental studies demonstrated how flow deflection at the leading edge of a
296 canopy impacts particle retention. Our study considered a canopy with uniform frontal area
297 density. Vertical variation in frontal area density may alter the pattern of flow deflection and
298 thus its impact on particle fate. The importance of the vertical distribution of canopy density is
299 illustrated by a recent large eddy simulation (LES, Pan et al., 2015) used to investigate particle
300 capture at the leading edge of a corn canopy. The LES corn canopy had frontal area density that
301 varied with vertical position within the canopy, with the densest region between $z/h =$ 0.3-0.9
302 (h =2.1 m, $1 - \delta_e/h = 0.8$). At the leading edge, the oncoming flow diverged around the high
303 density zone ($z/h =$ 0.3-0.9), so that an updraft was present in the upper canopy ($z/h > 0.66$)
304 but a downdraft was present in the lower canopy ($z/h < 0.33$). Because the downdraft pushed
305 particles towards the bed, increasing capture, the fraction of particles captured by the bed was
306 elevated at the leading edge ($x_{rel}/h = 0$), opposite to the trend of reduced particle retention
307 near the leading edge of our model canopy. In the corn canopy, the particle retention reached a

minimum after the decay of the downdraft ($x_{rel}/h = 1.9$). Beyond this point, particle capture within the corn canopy increased as the vertical updraft in the upper canopy decayed ($1.9 < x_{rel}/h < 14.6$).

Similar to the present study, previous investigators have also noted a minimum deposition at the leading edge of an emergent canopy of finite width, and increasing deposition with distance from the leading edge within an adjustment region. Zong and Nepf (2010) investigated rigid emergent canopies ($\phi = 0.02, 0.1$) placed against a flume sidewall. A region of lateral flow deflection was observed near the leading edge, extending to distance x_D from the leading edge. Consistent with this flow pattern, Zong and Nepf (2010) observed an increase in deposition with increasing distance from the leading edge, up to a maximum deposition occurring at distance x_D. However, Zong and Nepf (2010) attributed the diminished deposition near the leading edge to both the elevated turbulence in this region, as well as to the flow deflection. Similarly, Cotton et al. (2006) observed that deposition began after the leading edge of *Ranunculus* canopies in chalk streams.

Canopies that are both submerged (height h) and have finite width (B) could display both vertical and lateral flow deflection within the adjustment region. Such a three-dimensional flow diversion was observed around submerged circular patches of model flexible vegetation (Ortiz et al., 2013). The relative magnitude of the vertical and lateral flow deflections depends on the aspect ratio of the patch. Wide patches ($B \gg h$) deflect flow vertically, while flow around narrower patches ($B \ll h$) would be dominated by lateral deflection.

328 Under some flow conditions, flexible canopies experience reconfiguration and, in faster
329 flows, synchronized waving (*monami*). Reconfiguration reduces the average canopy height,
330 while maintaining a relatively constant frontal area, because the plants bend over in a
331 streamlined shape. Due to these changes in the canopy morphology, the length of the
332 adjustment region would decrease, due to the decreased $C_D ah$ (eq. 2), increasing the extent of
333 the fully developed region.

334 The effect of canopy hydrodynamics, including diversion within the adjustment region,
335 could be considered when designing experimental studies. Based on field observations of
336 canopy frontal area density and canopy height (Chandler et al., 1996, Moore, 2004, McKone,
337 2009), the adjustment region of *Zostera marina* canopies would extend approximately 9*h*. In
338 continuous *Zostera marina* meadows, particle transport beyond about 9*h* would resemble the
339 fully developed releases, while particle transport within the adjustment region would be
340 influenced by the flow diversion present in this region. In patchy landscapes, for which the
341 length of the canopy is less than x_D, flow diversion would occupy the full patch length, such
342 that patchy seagrass meadows may show reduced deposition, relative to a contiguous meadow
343 of the same total area. Flow in gaps shorter than $1.75h$ displayed little to no change from in-
344 canopy flow (Ikeda and Kanzawa 1996), so that some patchy meadows may act as a continuous
345 canopy. During meadow decline, seagrass canopies have been observed to degrade from a
346 single large canopy to a patchy landscape (Jill Carr, personal communication, March 30, 2016).
347 Establishment of a patchy pattern could reduce sediment deposition and enhance
348 resuspension, with these negative feedbacks further contributing to meadow decline.

3.4. Conclusion

Submerged aquatic vegetation interacts with currents, creating a complex flow structure with distinct regions of flow deflection, canopy scale turbulence, and element scale turbulence. This flow structure influences the fate of particles within the canopy. At the leading edge flow is deflected away from the region of high drag, and in a wide meadow ($B \gg h$) this creates a vertical updraft within the initial adjustment region (Figure 3b). If particle settling velocity is comparable to the updraft magnitude, then particle capture will be diminished by the presence of the updraft. Because the updraft decays with distance from the leading edge, particle increases with distance from the leading edge, reaching a maximum at the end of the adjustment region (x_D), at which point there is no updraft, and the canopy scale vortices are still small. In the fully developed region, particles that were released below the region flushed by canopy scale vortices ($z_{rel} < h - \delta_e$) have higher retention than particles released within this region ($z_{rel} > h - \delta_e$). Because particle retention is diminished near the leading edge, estimates of meadow-scale particle retention should consider the spatial variation across this region, especially when x_D is comparable to the meadow size.

Acknowledgements:

This material is based upon work supported by the National Science Foundation under Grant No. AGS-1005480. Any opinions, findings, or recommendations expressed in this material are those of the authors and do not necessarily reflect the views of the National Science Foundation

373 **References**

374 Agawin, N.S.R., Duarte, G.M., 2002. Evidence of direct particle trapping by a tropical seagrass
375 meadow. Estuaries and Coasts 25, 1205-1209.

376 Belcher, S.E., Jerram, N., Hunt, J.C.R., 2003. Adjustment of a turbulent boundary layer to a
377 canopy of roughnesss elements. JFM 488, 369-398.

378 Chandler, M., Colarusso, P., Buchsbaum, R., 1996. A study of eelgrass beds in Boston Harbor
379 and northern Massachusetts bays. Office of Research and Development, US EPA, Narragansett,
380 RI.

381 Chen, Z., Jiang, C., Nepf, H., 2013. Flow adjustment at the leading edge of a submerged aquatic
382 canopy. Water Resour. Res. 49, 5537-5551, doi:10.1002/wrcr.20403.

383 Chen, Z., Ortiz, A., Zong, L., Nepf, H., 2012. The wake structure behind a porous obstruction and
384 its implications for deposition near a finite patch of emergent vegetation. Water Res. Res. 48,
385 W09517, doi:10.1029/2012WR012224.

386 Cotton, J.A., Wharton, G., Bass, J.A.B., Heppell, C.M., Wotton, R.S., 2006. The effects of seasonal
387 changes to in-stream vegetation cover on patterns of flow and accumulation of sediment.
388 Geomorphology 77, 320-334.

389 Gacia, E., Duarte, C.M., 2001. Sediment retention by a Mediterranean *Posidonia oceanica*
390 meadow: the balance between deposition and resuspension. Estuarine, Coastal, and Shelf
391 Science 52, 505-514.

392 Gacia, E., Granata, T.C., Duarte, C.M., 1999. An approach to the measurement of particle flux
393 and sediment retention within seagrass (*Posidonia oceanica*) meadows. Aquatic Botany 65,
394 255-268.

395 Ghisalberi, M., Nepf, H., 2002. Mixing layers and coherent structures in vegetated aquatic flows.
396 Journal of Geophysical Research 107 (C2), 3011.

397 Ghisalberti, M., Nepf, H., 2005. Mass transport in vegetated shear flows. Environmental Fluid
398 Mechanics 5, 527-551.

399 Ghisalberti, M., Nepf, H.M., 2004. The limited growth of vegetated shear layers. Water Res. Res.
400 40, W07502, doi: 10.1029/2003WR002776.

401 Gurnell, A.M., Blackall, T.D., Petts, G.E., 2008. Characteristics of freshly deposited sand and finer
402 sediments along an island-braided, gravel-bed river: The roles of water, wind, and trees.
403 Geomorphology 99, 254-269.

404 Gurnell, A.M., Petts, G.E., Hannah, D.M., Smith, B.P.G., Edwards, P.J., Kollmann, J., Ward, J.V.,
405 Tockner, K., 2001. Riparian vegetation and island formation along the gravel-bed Fiume
406 Tagliamento, Italy. Earth Surf. Process. Landforms 26, 31-62.

Hughes, A.R., Stachowicz, J.J., 2004. Genetic diversity enhances the resistance of a seagrass ecosystem to disturbance. PNAS 101 (24), 8998-9002.

Irvine, M., Gardiner, B., Hill, M., 1997. The evolution of turbulence across a forest edge. Boundary Layer Meteorol. 84 (3), 467-496.

van Katwijk, M.M., Bos, A.R., Hermus, D.C.R., Suykerbuyk, W., 2010. Sediment modification by seagrass beds: Muddification and sandification induced by plant cover and environmental conditions. Estuarine, Coastal and Shelf Science 89, 175-181.

van Katwijk, M., Thorhaug, A., Núria, M., Orth, R., Duarte, C., Kendrick, G., ... Verduin, J., 2016. Global analysis of seagrass restoration: the importance of large-scale planting. Journal of Applied Ecology 53, 567-578.

Lawson, S.E., McGlatherty, K.J., Wiberg, P.L., 2012. Enhancement of sediment suspension and nutrient flux by benthic macrophytes at low biomass. Mar. Ecol. Prog. Ser. 448, 259-270.

Luhar, M., Rominger, J., Nepf, H., 2008. Interaction between flow, transport, and vegetation spatial structure. Environ Fluid Mech 8 (5): 423-439.

McKone, K., 2009. Light available to the seagrass *Zostera marina* when exposed to currents and waves. University of Maryland, Ph.D. thesis, 189 pp.

Moore, K.A., 2004. Influence of seagrasses on water quality in shallow regions of the lower Chesapeake Bay. J Coast Res 20, 162-178.

Morse, A., Gardiner, B., Marshall, B., 2002. Mechanisms controlling turbulence development across a forest edge. Boundary Layer Meteorol. 103 (2), 227-251.

Nepf, H., Ghisalberti, M., White, B, Murphy, E., 2007. Retention time and dispersion associated with submerged aquatic canopies. Water Res. Res. 43, W04422.

Nepf, H., Vivoni, E.R., 2000. Flow structure in depth-limited, vegetated flow. Journal of Geophysical Research 105 (C12), 28547-28557.

Ortiz, A.C., Ashton, A., Nepf, H., 2013. Mean and turbulent velocity fields near rigid and flexible plants and the implications for deposition. J Geophys. Res.: Earth Surf. 118, 2585-2599

Pan, Y., Chamecki, M., Isard, S.A., Nepf, H., 2015. Dispersion of particles released at the leading edge of a crop canopy. Agric. For. Meteorol. 211-212, 37-47.

Poindexter, C.M., Rusello, P.J., Variano, E.A., 2011. Acoustic Doppler velocimeter-induced acoustic streaming and its implications for measurement. Exp Fluids 50, 1429-1442.

Raupach, M.R., Finnigan, J.J., Brunet, Y., 1996. Coherent eddies and turbulence in vegetation canopies: the mixing-layer analogy. Boundary-Layer Meteorology 25th anniversary volume, 1970-1995, pp. 351-382.

440 Sand-Jensen, K., 1998. Influence of submerged macrophytes on sediment composition and
441 near-bed flow in lowland streams. Freshwater Biology 39, 663-679.

442 Tanaka, N., and J. Yagisawa (2010), Flow structures and sedimentation characteristics around
443 clump-type vegetation, *J. Hydro-environment Res.*, *4*(1), 15–25, doi:10.1016/j.jher.2009.11.002

444 Terrados, J., Duarte, C.M., 2000. Experimental evidence of reduced particle resuspension within
445 a seagrass (*Posidonia oceanica*) meadow. Journal of Experimental Marine Biology and Ecology
446 243, 45-53.

447 Ward, L.G., Kemp, W.M., Boynton, W.R., 1984. The influence of waves and seagrass
448 communities on suspended particulates in an estuarine embayment. Marine Geology 59, 85-
449 103.

450 Zong, L., Nepf, H. 2010. Flow and deposition in and around a finite patch of vegetation.
451 Geomorphology 116, 363–372.

452

Chapter 4

Strong and weak, unsteady reconfiguration and its impact on turbulence structure within plant canopies[1]

[1]This chapter has been previously copyrighted by the American Institute of Physics and is therefore excluded from the MIT copyright covering other chapters of this thesis. Citation: Pan, Y., Follett, E., Chamecki, M., Nepf, H., 2014. Strong and weak, unsteady reconfiguration and its impact on turbulence structure within plant canopies. Physics of Fluids 26, 105102 doi: 10.1063/1.4898395

PHYSICS OF FLUIDS 26, 105102 (2014)

Strong and weak, unsteady reconfiguration and its impact on turbulence structure within plant canopies

Ying Pan,[1,a] Elizabeth Follett,[2] Marcelo Chamecki,[1] and Heidi Nepf[2]
[1]*Department of Meteorology, The Pennsylvania State University, University Park, Pennsylvania 16802, USA*
[2]*Department of Civil and Environmental Engineering, Massachusetts Institute of Technology, Cambridge, Massachusetts 02139, USA*

(Received 24 March 2014; accepted 6 October 2014; published online 21 October 2014)

Flexible terrestrial and aquatic plants bend in response to fluid motion and this reconfiguration mechanism reduces drag forces, which protects against uprooting or breaking under high winds and currents. The impact of reconfiguration on the flow can be described quantitatively by introducing a drag coefficient that decreases as a power-law function of velocity with a negative exponent known as the Vogel number. In this paper, two case studies are conducted to examine the connection between reconfiguration and turbulence dynamics within a canopy. First, a flume experiment was conducted with a model seagrass meadow. As the flow rate increased, both the mean and unsteady one-dimensional linear elastic reconfiguration increased. In the transition between the asymptotic regimes of negligible and strong reconfiguration, there is a regime of weak reconfiguration, in which the Vogel number achieved its peak negative value. Second, large-eddy simulation was conducted for a maize canopy, with different modes of reconfiguration characterized by increasingly negative values of the Vogel number. Even though the mean vertical momentum flux was constrained by field measurements, changing the mode of reconfiguration altered the distribution, strength, and fraction of momentum carried by strong and weak events. Despite the differences between these two studies, similar effects of the Vogel number on turbulence dynamics were demonstrated. In particular, a more negative Vogel number leads to a more positive peak of the skewness of streamwise velocity within the canopy, which indicates a preferential penetration of strong events into a vegetation canopy. We consider different reconfiguration geometry (one- and two-dimensional) and regime (negligible, weak, and strong) that can apply to a wide range of terrestrial and aquatic canopies.
[http://dx.doi.org/10.1063/1.4898395]

I. INTRODUCTION

Over the past two decades, the quantification and understanding of land-surface fluxes from vegetated surfaces such as forests and crops has been the focus of great research efforts. These studies have been motivated by the important exchanges of latent heat, water vapor, and carbon dioxide that take place at the canopy-atmosphere interface. These fluxes between the terrestrial vegetation and the atmosphere impact micro and mesoscale meteorology, regional and global climate change, carbon balance and cycling, as well as hydrology.[1,2] Fluxes of trace gases and aerosols at the canopy-atmosphere interface also determine the important role of vegetated surfaces on the removal of air pollutants (e.g., tropospheric ozone,[3,4] heavy metals,[5] and aerosols[6]). Transport of biogenic particles emitted from forests and crops such as pollens,[7] seeds,[8] and spores[9] also play an important role in ecological and agricultural processes. In aquatic systems, turbulent transport at the top of submerged

[a] Author to whom correspondence should be addressed. Electronic mail: yyp5033@psu.edu

vegetation may influence the availability of nutrients within the canopy as well as the release of seeds from the vegetation. In addition, the penetration of turbulence through the canopy to the bed determines the likelihood of sediment resuspension, an important feedback to vegetation health.[10,11] Specifically, resuspension negatively impacts light availability for photosynthesis and associated erosion may destabilize shoots. Dense canopies that reduce near-bed turbulence can enhance the supply of nutrients to the plants by promoting the retention of nutrient-rich fine sediment and organic matter.[12] From a fluid dynamical perspective, all these exchanges are driven by the complex turbulent flow field produced by the mechanical interactions between the flow and canopy elements. Thus, understanding these interactions and the properties of the turbulent flow produced at this interface is of great importance in all these fields.

When flow passes through vegetation canopies, surface forces acting on the interfaces between flow and canopy elements remove momentum and dissipate the kinetic energy of the flow. The bulk effect of these exchanges is a drag force acting on the mean flow within the canopy layer. For canopies of sufficient density, the discontinuity of drag at the top of the canopy leads to an inflectional mean velocity profile with the inflection point located near the canopy top. This velocity profile has a similar shape to that in a free shear layer, that is, a mixing layer formed between two uniform, parallel streams of different velocities.[13] The inflectional mean velocity profile triggers instabilities and coherent eddies within the canopy shear layer similar to the Kelvin-Helmholtz (KH) instabilities and coherent eddies observed in a free shear layer.[13] These canopy-scale coherent structures (denoted as "KH coherent structures" hereafter) dominate the transport of momentum from above the canopy to the canopy layer. For example, observations of aquatic[14] and terrestrial canopies[15] demonstrated that 80%–90% of the time-mean downward momentum transport ($\overline{u'w'} < 0$) occurred within short, intense events that occupied only 25%–35% of total time. The dominating events occurred at time-intervals consistent with the passage of the KH vortices. Here, the overbar denotes the time-average, and the primes denote instantaneous deviations, defined as $u'(t) = u(t) - \overline{u}$ and $w'(t) = w(t) - \overline{w}$, for streamwise ($u$) and vertical ($w$) velocities, respectively. Scalar flux at the canopy-free flow interface has also been linked to the passage of KH vortices in both aquatic[16] and terrestrial canopies.[17] Because of the importance of these coherent structures to the exchange of momentum and scalars, it is vital that their intensity and depth of penetration into the canopy be properly modeled.

Typically, a strong sweep ($u' > 0$, $w' < 0$) is observed as the leading edge of these coherent structures pass, and a weaker ejection ($u' < 0$, $w' > 0$) occurs as the trailing edge passes.[18] Physically, sweeps represent the vertical transport of fluid parcels with high momentum downward towards a boundary near which there is a region of lower average momentum, while ejections represent the vertical transport of fluid parcels with low momentum upward into a region of higher average momentum. Both sweeps and ejections result in a net downward flux of momentum ($\overline{u'w'} < 0$). Many studies within a variety of real and model canopies have observed non-zero velocity skewness, specifically $Sk_u > 0$ and $Sk_w < 0$, indicating the prevalence of events with strong positive streamwise velocity ($u' > 0$) and strong negative vertical velocity ($w' < 0$), i.e., sweeps. This implication is consistent with the idea that flux into the canopy is dominated by the canopy-scale coherent structures described above. Here, the values of velocity skewness are calculated as $Sk_u = \overline{u'^3}/\sigma_u^3$ and $Sk_w = \overline{w'^3}/\sigma_w^3$, where $\sigma_u = \sqrt{\overline{u'^2}}$ and $\sigma_w = \sqrt{\overline{w'^2}}$ are the standard deviation of streamwise and vertical velocities, respectively. Reproducing velocity skewness (Sk_u and Sk_w) as well as the momentum flux transported by sweeps and ejections is therefore the basic requirement for proper modeling of canopy-scale coherent structures. However, existing third-order closure models[19] and large-eddy simulation (LES) models[20–25] have underestimated velocity skewness (Sk_u and Sk_w) as well as the ratio between momentum flux transported by sweeps and ejections by more than 50%. Recent work has shown that including a model that represents the effects of plant reconfiguration (the bending of plant stems, branches, leaves, etc.) on the flow field greatly reduces these under-predictions.[26]

Both terrestrial and aquatic plants take advantage of elastic reconfiguration to reduce drag forces and avoid uprooting or breaking under high winds and currents.[27] The impact of reconfiguration on the drag force has been described by a modification to the quadratic drag law, which can be

modeled by introducing the Vogel number B. Specifically, the drag force $F_D \propto U^{2+B}$, with U a characteristic velocity scale acting on the plant element.[27,28] It is sometimes convenient in modeling to transfer the velocity dependence to the drag coefficient, i.e., we write $F_D \propto C_D U^2$, with $C_D \propto U^B$. In the asymptotic regime of negligible reconfiguration, $B \to 0$, and the quadratic increase of drag with velocity is recovered. In the asymptotic regime of strong reconfiguration, dimensional analysis balancing drag force and the plant's internal resistance to bending suggests specific values of B.[29,30] For linear elastic bending, $B = -2/3$, if reconfiguration is associated with the loss of one characteristic length, such as the bending of a beam or a rectangular plate along a single axis, and $B = -4/3$, if reconfiguration leads to the loss of two characteristic lengths, such as the crumpling of a paper or the rolling of a disk into a cone. For some aquatic plants, the primary restoring force is buoyancy, rather than rigidity. If buoyancy alone is considered as the restoring force $B = -4/3$; and the inclusion of buoyancy in addition to rigidity as restoring forces delays the asymptotic regime of strong reconfiguration to higher values of fluid velocity.[31] These theoretical models predict drag forces in good agreement with laboratory measurements of fibers in soap films,[32] rectangular plates in a wind tunnel,[33] and model seagrass blades in water.[31] The range $-2/3 \lesssim B \lesssim 0$ is also in rough agreement with many measured values for natural canopies in which one-dimensional (1D) bending is observed.[28,30,34] For example, de Langre *et al.* reported $B = -0.52$ to -0.80,[30] and Albayrak *et al.* reported $B = -0.5$ to -0.7.[34] Harder *et al.* observed two regimes of behavior for the giant reed (*Arundo donax L.*).[35] For wind speeds up to 1 m s^{-1}, little bending occurred, and the drag force was approximately quadratic ($B \approx 0$), as expected for an unyielding object. However, for wind speeds above 1.5 m s^{-1}, significant bending occurred, and the observed $B = -0.7$ was consistent with the scaling for a reconfigured beam ($B = -2/3$).

Although most previous studies have focused on time-averaged flow conditions and the associated mean reconfiguration,[30,34] some studies report instantaneous relationships between velocity and reconfiguration.[35,36] Indeed, the phenomena of *honami* and *monami* (progressive waves of canopy bending) are examples of plants bending in response to the passage of individual canopy-scale coherent eddies.[37,38] We hypothesize that the reconfiguration of plants at time-scales comparable to individual KH eddies can preferentially enhance the penetration of strong events into a vegetation canopy because the plants yield more to strong events. Specifically, we propose that the drag coefficient responds to the instantaneous velocity, $\boldsymbol{u} = (u, v, w)$ (a vector consisting of streamwise, spanwise, and vertical components), such that the characteristic velocity $U = |\boldsymbol{u}|$ and $C_D \propto U^B$ will be smaller for stronger events (higher $|\boldsymbol{u}|$). Note $|\boldsymbol{u}|$ is statistically positively correlated with its streamwise component, u, so that in general stronger events have higher u. The canopy-drag length-scale, $L_c \propto (C_D a)^{-1}$, describes the penetration of turbulent momentum flux into the canopy,[39,40] where a is the frontal canopy area per volume. If stronger events (higher u) experience a smaller $C_D \propto U^B$, then they can penetrate a greater distance into the canopy before being arrested by drag, compared to weaker events (smaller u). This impact of plant flexibility should be evident in the skewness of the streamwise and vertical velocities (Sk_u and Sk_w, respectively), which are statistical measures of bias toward larger events.

In this paper, we consider two case studies that examine the connection between reconfiguration and turbulence structure within a canopy, focusing on skewness as an indicator for bias toward large events. First, we consider a flume experiment with a model seagrass meadow. As flow speed over the meadow increases, both the mean and unsteady reconfiguration increase. We consider how these changes in reconfiguration are connected with both the magnitude and vertical position of the peak skewness, using expected changes in $C_D \propto U^B$ based on a force balance for individual model blades.[31] Second, we investigate the effects of different modes and degrees of reconfiguration on turbulence statistics using a LES for a maize canopy, in which reconfiguration is parameterized using a range of Vogel numbers. With mean vertical momentum flux constrained by field experimental data, increasingly negative B shifts the magnitude and vertical position of peak skewness, alters the stress fractions carried by strong events, and changes the distribution of stress fractions carried by sweeps ($u' > 0$, $w' < 0$) and ejections ($u' < 0$, $w' > 0$). These case studies suggest that the proper modeling of turbulence in plant canopies requires that instantaneous reconfiguration be incorporated into models through the use of a velocity-dependent drag coefficient.

II. RECONFIGURATION AND SKEWNESS IN A MODEL SEAGRASS

In this section, we consider a model seagrass meadow that is dynamically and geometrically similar to *Zostera marina*.[14] The measurements are interpreted through the lens of a recent theoretical model that predicts the impact of mean reconfiguration on the drag experienced by individual seagrass blades.[31] We propose that the mean reconfiguration model can be used to infer the impact of instantaneous reconfiguration associated with the arrival of individual turbulent events. It is important to note that, for aquatic plants, buoyancy, in addition to rigidity and drag, can influence plant posture in flow, because the material density of many aquatic plants is below that of water (e.g., seagrass blade density is 700 kg m^{-3}),[41] compared to typical coastal water densities of 1015 kg m^{-3} (Atlas of the Oceans, NOAA). In addition, aquatic plants often have small gas filled chambers, used to enhance buoyancy and maintain upright postures.[42,43] Luhar and Nepf extended previous work on reconfiguration by considering buoyancy, drag, and rigidity together.[31] They quantified the steady reconfiguration under steady (time-average) velocity $\overline{u}$, using an effective blade length, l_e, which represents the length of a rigid, vertical blade that generates the same horizontal drag (F_D) as a flexible blade of total length l. For blade width, b, and fluid density, ρ, the effective blade length (l_e) is given by the following definition:

$$F_D = \frac{1}{2}\rho C_D^o b l_e U^2. \tag{1}$$

In Eq. (1), the drag coefficient is assumed to be a constant, which is denoted by the superscript "o." Also note that, for generality, we use the characteristic velocity scale U, which in this section refers to the time-averaged velocity $\overline{u}$. Luhar and Nepf[31] used a numerical model to predict the total drag on a single blade (F_D), and from this they extract the ratio l_e/l as a function of the mean velocity $\overline{u}$. As velocity increased, the blade bent over further in the streamwise direction, which decreased the frontal area and also created a more streamlined shape. Both effects are reflected in the decreasing value of l_e/l. Many previous studies characterized reconfiguration of aquatic vegetation through changes in the drag coefficient,[44] for which the total drag is, $F_D = (1/2)\rho C_D b l U^2$, with C_D a function of U. Equating this drag expression to Eq. (1), one can show that $l_e/l = C_D/C_D^o \propto U^B$, and we see that the dependence of l_e/l on U can be expressed through the Vogel exponent B.

Blade posture in flow is governed by two parameters. The Cauchy number, Ca, describes the ratio of the drag force to the restoring force due to rigidity. The dimensionless buoyancy, R_B, describes the ratio of restoring forces due to buoyancy and rigidity

$$Ca = \frac{1}{2}\frac{\rho C_D^o b U^2 l^3}{EI}, \tag{2}$$

$$R_B = \frac{\Delta\rho g b t l^3}{EI}. \tag{3}$$

Here, $\Delta\rho$ is the difference in density between the fluid and the blade, g is the gravitational acceleration, E is the elastic modulus, and $I = bt^3/12$ is the second moment of area, with t the blade thickness. Because these two parameters control the blade posture in flow (i.e., the degree of bending), they also predict the dependence $l_e/l = C_D/C_D^o$, as described by Luhar and Nepf.[31] For example, Fig. 1(a) depicts the dependence of C_D/C_D^o for $R_B = 0$ (no buoyancy) and $R_B = 6.4$ (the dimensionless buoyancy of the model seagrass). For the lowest values of Ca, the blade remains essentially upright (negligible reconfiguration). Consistent with this posture, the drag is quadratic with U, i.e., $C_D/C_D^o \approx 1$ and $B \approx 0$, similar to the response of the giant reed at low wind speed.[35] The main impact of buoyancy is to delay the onset of blade reconfiguration, i.e., buoyant blades remain upright at higher velocities, which extends the range of Ca for which $B \approx 0$. For $Ca > 100$, strong reconfiguration occurs (Fig. 1(c)), and the effective length-scale over which drag occurs (l_e) is comparable to the length-scale over which bending occurs (l_b). For this degree of reconfiguration, specifically $l_b = l_e$, the balance of drag to the restoring force due to rigidity produces the scaling $l_e/l = Ca^{-1/3}$, $B = -2/3$, as previously derived by Alben *et al.*[29] The drag coefficient ratio (C_D/C_D^o) displays this dependency in Fig. 1(a) for $Ca > 100$. In the regime of strong reconfiguration ($Ca > 100$), buoyancy plays a

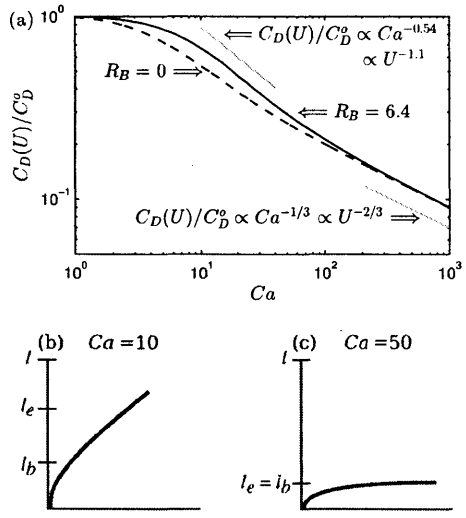

FIG. 1. (a) Dependence of normalized drag coefficient $C_D(U)/C_D^o$ with Cauchy number Ca for a simplified dense canopy flow profile, with buoyancy parameter $R_B = 6.4$ (black solid line; see Ghisalberti and Nepf[14]) and $R_B = 0$ (black dashed line). Grey solid lines with Vogel numbers $B = -1.1$ and $B = -2/3$ are noted for reference. The maximum Vogel exponent ($B = -1.1$) occurs in the weak reconfiguration regime ($Ca = 10$–50), in which the blades bend over length-scale l_b, but experience drag over length-scale $l_e > l_b$, as demonstrated with the corresponding blade posture (b). For strong reconfiguration ($Ca > 100$), as demonstrated with the corresponding blade posture (c), $l_e = l_b$, which leads to $B = -2/3$, as described by Alben *et al.*[29] This figure is a revised version of Fig. 2(c) in M. Luhar and H. M. Nepf, "Flow-induced reconfiguration of buoyant and flexible aquatic vegetation," Limnol. Oceanogr. **56**, 2003–2017 (2011). Copyright 2014 Association for the Sciences of Limnology and Oceanography, Inc.[31]

negligible role in plant posture, so that the scaling $C_D/C_D^o \propto Ca^{-1/3}$ is observed for all values of R_B (also discussed by Luhar and Nepf[31]). Finally, for weak reconfiguration, associated with intermediate values of Ca ($\approx$10–50), the blade is only slightly bent. In this posture (Fig. 1(b)), the effective length-scale for drag (l_e) is greater than the length-scale over which bending occurs (l_b) so that a balance of drag to rigidity yields the scaling $l_e/l = C_D/C_D^o = Ca^{-1/3}(l_e/l_b)^2$, with $l_e/l_b > 1$. In this regime, as the velocity increases the blade progressively bends further, so that l_e/l_b decreases with increasing Ca, until $l_e/l_b \to 1$, at which point the regime of strong reconfiguration is reached. Within the weak reconfiguration regime, $(l_e/l_b)^2 \sim Ca^m$, and thus $l_e/l = Ca^{-(1/3+m)}$, $B = -(2/3 + 2m)$, so that B is most negative in the weak reconfiguration regime. In other words, for a blade geometry (i.e., bending in one dimension) the deviation from the quadratic drag response is greatest in the regime of weak reconfiguration. For example, in Fig. 1(a) the maximum slope occurs at $Ca = 21$, with $C_D/C_D^o = Ca^{-0.54}$ (i.e., $B = -1.1$). Similarly, a maximum in $-B$ was also observed at the transition between negligible and strong reconfiguration of deforming plates and disks.[33] Finally, although the curves in Fig. 1(a) strictly describe steady reconfiguration under time-mean flow, we propose that the curves can be used to interpret the impact of reconfiguration on the drag experienced by individual sweeps penetrating the canopy. We anticipate that the highest skewness values will be observed in the weak reconfiguration regime, for which B is the most negative, creating the greatest bias for strong events. This could have important implications for suspended sediment within the canopy, because the penetration of individual strong events may resuspend more material than more persistent but weaker turbulence.

A. Experimental design

The effect of reconfiguration was evaluated by comparing the behavior of a single meadow of flexible blades at six flow rates (runs F1–F6 in Ghisalberti and Nepf[14]), which resulted in different levels of both mean and unsteady reconfiguration. Each model plant was constructed of a wooden

dowel stem (1.5 cm high) and six blades ($l = 20.3$ cm, $b = 3.8$ mm, $t = 0.20$ mm) cut from low-density polyethylene (LDPE) film ($E = 3.0 \times 10^8$ Pa, $EI = 7.5^{-7}$ N m^2, and density $\rho_s = 920$ kg m^{-3}). The model plants were designed to be dynamically and geometrically similar to eelgrass (*Zostera marina*), as described by Ghisalberti and Nepf.[38] The meadow was 6.5 m long and had a stem density of 230 plants m^{-2}. When undeflected, the meadow height was $h = 21.5$ cm (blade plus stem), and the frontal area per volume was $a = 5.2$ m^{-1}, assuming all blades were seen by the flow, so that the roughness density was $ah = 1.1$. This corresponds to a dense canopy ($ah > 0.1$) for which turbulent sweeps are not expected to penetrate through the entire height of the canopy.[10,45] For comparison, we also considered a completely rigid model canopy with comparable roughness density, $h = 13.8$ cm, $a = 8$ m^{-1}, and $ah = 1.1$ (run R8 in Ghisalberti and Nepf[14]).

Acoustic Doppler velocimetry (ADV) was used to measure the three velocity components (u, v, w) at four positions separated by 7.5 cm. At each point, vertical profiles were collected at 1-cm intervals over depth, using a record length of 10 min. A 12-cm space ($1.8\Delta S$, where ΔS is the average distance between stems) was made in the meadow to allow probe access without interference from blades. Ikeda and Kanazawa showed that the removal of canopy elements over a length less than $7\Delta S$ has little impact on flow statistics.[46] Given that our gap is smaller, we also expect the gap to have negligible impact on the velocity measurement (as discussed in detail by Ghisalberti and Nepf[14]). The Reynolds stress is defined as $\overline{u'w'}$. The maximum penetration of turbulence into the canopy was defined by the position at which the Reynolds stress dropped to 10% of the peak value observed at the top of the canopy. The distance to this point from the top of the canopy is called the penetration scale, δ_e. A video camera was used to determine the deflected meadow height h and *monami* amplitude A_w, defined by the vertical excursion of blades during a *monami* cycle (Table 1 in Ghisalberti and Nepf[14]). Using the standard deviation of the velocity record, σ_u, the skewness of u was defined as $Sk_u = \overline{u'^3}/\sigma_u^3$, and similarly for Sk_w. The turbulence statistics were first calculated for individual profiles and then averaged over four profiles at different locations within the meadow, using linear interpolation to match the vertical positions. The Cauchy number was estimated in two ways, to reflect both the impact of the surrounding canopy and the unsteady variation in the deflection of individual blades. A predictive equation for the time-averaged deflected height of a meadow (h), as a function of Ca and R_B (Eq. (4) in Luhar and Nepf[47]), was used to infer the value of Ca, based on the observed value of h, which we call Ca_h. For some flow conditions, the passage of shear-layer vortices generated an additional, time-varying deflection, called *monami*. Using the *monami* amplitude (A_w), a second estimation, Ca_{A_w}, was found using the canopy height at the point of maximum deflection ($h - A_w$) in Eq. (4) of Luhar and Nepf.[47] The second estimate captures the conditions associated with the strongest sweep events. Finally, to provide a direct comparison between skewness and Vogel number B, the value of $B = B(Ca)$ was extracted from the curve shown in Fig. 1(a) (Eq. (16) in Luhar and Nepf[31]), with $R_B = 6.4$, corresponding to the model seagrass. Because $Ca \propto U^2$, $C_D/C_D^o \propto Ca^{B/2}$, so that B is twice the slope of the curve.

B. Experimental results

To begin, we consider how the mean reconfiguration of the meadow impacts vertical profiles of mean velocity, Reynolds stress, and skewness (Fig. 2). We compare a case with negligible reconfiguration (F2; $h = 21.3$ cm, $A_w = 0$) to a case with weak reconfiguration (F5; $h = 17$ cm, $A_w = 4.1$ cm). For each profile, a horizontal line indicates the mean deflected height, h. Once reconfiguration was initiated, h progressively declined as the mean velocity at the top of the meadow ($\overline{u}_h$), and thus Ca, increased (Table I). The peak Reynolds stress coincided roughly with h, and thus descended toward the bed as the meadow was deflected (Fig. 2(b)). Note that Reynolds stress was linear above the meadow, consistent with open channel flow. The length-scale over which Reynolds stress penetrated into the meadow (δ_e) also increased with Ca, from 9.8 cm (F1) to 12.8 cm (F6, Table I), suggesting that with increasing mean reconfiguration the meadow also became more porous to the sweep events that carry most of the turbulent flux. The penetration of sweep events was also reflected in the *monami* amplitude (A_w), which also increased with increasing Ca (Table I). The increasing penetration length-scale and decreasing canopy height together caused the fraction of

TABLE I. Time-mean deflected canopy height h (cm above bed); *monami* amplitude A_w (dashed means no *monami* observed); time-mean velocity at top of canopy $\overline{u}_h$ (* as given in Table 1 of Ghisalberti and Nepf[14]). Undeflected meadow height is 21.5 cm. Penetration length-scale, δ_e, is distance from top of canopy to point at which Reynolds stress is reduced to 10% of maximum. Ca_h is Cauchy number estimated from time-mean deflected height (h) using Eq. (4) in Luhar and Nepf.[47] Ca_{A_w} uses maximum deflected height, $h - A_w$. Maximum magnitude of skewness values in u and w ($Sk_{u,\max}$ and $Sk_{w,\min}$) and vertical position of maximum skewness in u, $z(Sk_{u,\max})$, are the mean of values selected from four individual vertical profiles, and the uncertainty indicates one standard deviation between profile values.

	h^* [cm]	A_w^* [cm] ±25%	$\overline{u}_h^*$ [cm s^{-1}]	δ_e [cm] ±1.0	δ_e/h ±0.5	Ca_h	Ca_{A_w}	$z(Sk_{u,\max})$ [cm]	$Sk_{u,\max}$	$Sk_{w,\min}$
F1	21.5	...	1.7	9.8	0.46	1	1	13 ± 2	0.72 ± 0.16	−1.26 ± 0.09
F2	21.3	...	3.0	10.0	0.51	2	2	14 ± 2	1.13 ± 0.16	−1.16 ± 0.21
F3	20.0	2.7	3.7	11.0	0.55	6	16	10 ± 2	1.37 ± 0.15	−1.43 ± 0.12
F4	18.6	3.5	4.4	11.5	0.62	10	31	10 ± 1	1.36 ± 0.06	−1.45 ± 0.12
F5	17.0	4.1	5.7	12.3	0.72	17	61	7 ± 2	1.60 ± 0.15	−1.18 ± 0.18
F6	15.5	4.4	7.9	12.8	0.83	28	122	7 ± 1	1.38 ± 0.13	−1.34 ± 0.27
R8	13.8	...	4.0	7.8	0.57	0	0	9 ± 1	0.78 ± 0.26	−0.96 ± 0.25

canopy influenced by vertical turbulent flux (δ_e/h) to increase with increasing Ca, from 0.46 (F1) to 0.83 (F6, Table I).

The increasing preference for large sweep events with increasing Ca is evident in the skewness profiles. For both cases shown (F2 and F5, Fig. 2), the skewness of u (Sk_u) was elevated in the upper canopy, but returned to zero in the lower canopy, suggesting that sweep events did not penetrate to the bed for either flow condition, and this is consistent with the penetration length-scale (Table I) and other observations in dense canopies (e.g., Chen *et al.*[48]). The peak Sk_u moved closer to the bed with increasing Ca (see $z(Sk_{u,\max})$ in Table I), due both to the deflection of the meadow (h) and the increase in penetration length (δ_e), i.e., similar to the Reynolds stress. Specifically, the peak Sk_u occurred at $z = 14$ cm (F2) and $z = 7$ cm (F5), with the distance from the meadow interface (h) increasing from 7.3 cm (F2) to 10 cm (F5). Similar trends were seen in Sk_w; however, the vertical skewness did not always return to zero near the bed. A similar tendency has been observed in terrestrial canopies.[18] The greater penetration of Sk_w relative to Sk_u may reflect a preferential

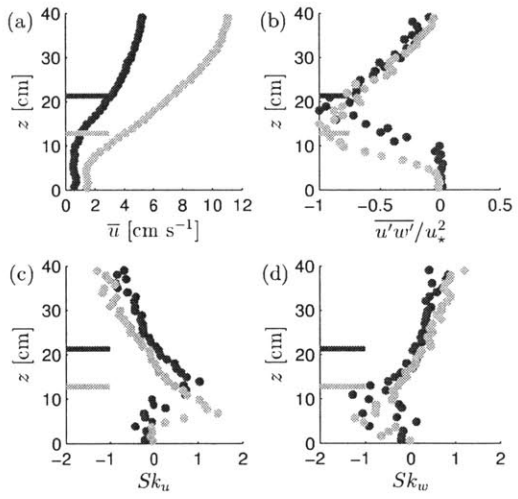

FIG. 2. Vertical profiles of (a) time-mean streamwise velocity ($\overline{u}$), (b) mean vertical momentum flux ($\overline{u'w'}$) normalized by the square of friction velocity (u_*^2), (c) skewness of u (Sk_u), and (d) skewness of w (Sk_w) for two flow rates over a flexible canopy, one case with negligible reconfiguration (F2; black dots) and the other case with weak reconfiguration (F5; grey dots). Each profile is a spatial average of four individual profiles.[14] The solid horizontal lines indicate the canopy height h.

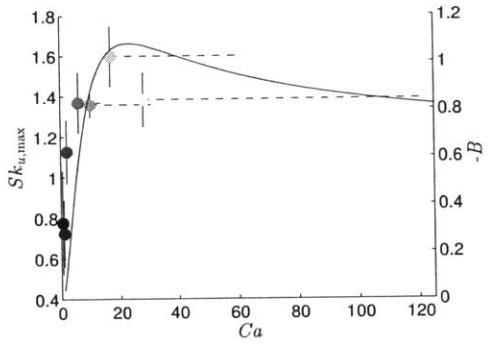

FIG. 3. Left-hand axis shows maximum skewness of u (Sk_u) observed within canopy for different values of Cauchy number, Ca. Circles indicate Ca_h and horizontal dashed lines extend to Ca_{A_w}, as defined in Table I. Vertical error bars represent the standard deviation between at least four individual profiles. Solid curve and right-hand axis show the value of Vogel exponent (plotted as $-B$) derived from the slope of the function C_D/C_D^o versus Ca shown in Fig. 1(a).

damping of the longitudinal velocity component relative to the vertical component, which may be due to asymmetries in the plant elements that produce asymmetries in the drag.

Finally, we consider how observed changes in peak skewness relate to the expected impact of reconfiguration on drag coefficient (Fig. 1). We anticipate that as the Vogel number (B) becomes increasingly negative, the difference between the drag coefficient acting on weak and strong events will become greater, $C_D \propto u^B$, with the result that stronger sweep events are increasingly favored, producing larger values of skewness. The Vogel number (plotted as $-B$ in Fig. 3) was derived from the slope of the function C_D/C_D^o versus Ca, shown in Fig. 1(a). A peak value of $-B = 1.1$ is observed at $Ca = 21$. As discussed with Fig. 1, this corresponds to the weak reconfiguration regime. For higher values of Ca (beyond that shown in Fig. 3), B asymptotes to the prediction for strong reconfiguration, $-B = 2/3$. The observed peak values of Sk_u are also shown in Fig. 3. Circles indicate Ca_h and horizontal dashed lines extend to Ca_{A_w}, as defined in Table I. The maximum skewness has a peak value at $Ca_h = 17$ (F5 in Table I), which is close to $Ca = 21$, the position at which B is the most negative. Note that the curve for $-B$ and the skewness points shown together in Fig. 3 are not directly related. In other words, we do not imply the line for $-B$ fits the points; we plot them together to visually reveal how the peak in $Sk_{u,\max}$ and $-B$ occur at similar values of Ca and within the regime of weak reconfiguration. We also note that for $Ca_h = 1$ (F1), the flexible canopy produces a skewness maximum ($Sk_{u,\max}$) that is the same as that observed in the rigid canopy (R8) within uncertainty, i.e., at $Ca = 1$ the flexible canopy interacts with the flow in analogy to a fully rigid canopy. Finally, it is interesting to note that field conditions for seagrass range from $Ca = 0$ (slack tide) to 2000 (based on values given in Table II and Fig. 7 of Luhar and Nepf[31]), so that all three regimes of behavior; rigid ($B = 0$), weak reconfiguration ($B < -1$), and strong reconfiguration ($B = -2/3$); are experienced by real meadows.

III. NUMERICAL SIMULATION OF PLANT RECONFIGURATION

In this section, we use a LES model to investigate the effects of different modes and degrees of plant reconfiguration on the turbulence characteristics inside a terrestrial canopy. The different modes and degrees of reconfiguration are modeled by varying the Vogel number B. We consider four cases: $B = 0$ (rigid canopy with no reconfiguration), $B = -2/3$ (strong reconfiguration for 1D linear elastic bending[29]), $B = -1$ (weak reconfiguration for 1D elastic bending described in Sec. II), and $B = -4/3$ (strong reconfiguration for two-dimensional (2D) linear elastic bending[33]).

A. Numerical model

The LES model employed here is described in detail by Pan *et al.*[26] The sink of flow momentum per unit volume induced by forces acting on the surfaces of canopy elements is parameterized as a

"drag force" (f_D) following the approach proposed by Shaw and Schumann,[20]

$$f_D = -C_D (a_c \mathbf{P}) \cdot (|\tilde{\boldsymbol{u}}| \tilde{\boldsymbol{u}}), \tag{4}$$

where $\tilde{\boldsymbol{u}}$ is the filtered velocity, and a_c is the two-sided leaf area density. Note that in Sec. II the frontal area per volume a is equivalent to one-sided leaf area density, and the roughness density ah is equivalent to one-sided leaf area index (LAI). The projection tensor $\mathbf{P} = P_x \boldsymbol{e}_x \boldsymbol{e}_x + P_y \boldsymbol{e}_y \boldsymbol{e}_y + P_z \boldsymbol{e}_z \boldsymbol{e}_z$ is used to split a_c into streamwise (x), spanwise (y), and vertical (z) directions, where $\boldsymbol{e}_j$ is the unit vector in the jth direction. Values of a_c and $\mathbf{P}$ are provided by Pan *et al.*[26] Please note the distinction between the volume average (f_D) and the drag on a single blade (F_D) defined by Eq. (1).

LES studies of forests[20–24,49] and crop canopies[25,50] typically treat C_D as a constant, implying $|f_D| \propto |\tilde{\boldsymbol{u}}|^2$. To reflect the impact of reconfiguration, the general expression $C_D = (U/A)^B$ was adopted, with $|\tilde{\boldsymbol{u}}|$ being the characteristic velocity scale U. Here, A is a velocity scale related to canopy geometry and rigidity,[26] and B is the Vogel number. The dependence of C_D on velocity can be estimated by fitting field experimental data to the mean momentum equation following the approach used by Cescatti and Marcolla.[51] Fitting C_D to data obtained in a large maize field near Mahomet, IL on July 10, 2011 ($h = 2.1$ m, LAI = 3.3, and for details of field experiment see Gleicher *et al.*[52]), Pan *et al.* obtained $A = 0.29$ m s^{-1} and $B = -0.74$.[26] This estimated Vogel exponent is within the range of theoretical values ($B = -2/3$ to $-4/3$) and other measured values ($B = -0.5$ to -0.8), described in Sec. I. Pan *et al.*[26] compared LES results using the velocity-dependent drag coefficient model to those using the constant drag coefficient model ($C_D = 0.25$, based on the data obtained by Wilson *et al.*[53]). Note that a constant drag coefficient assumes no reconfiguration ($B = 0$). The drag model that mimicked the impact of reconfiguration produced a remarkable improvement in the comparison between LES results and observed values of skewness (reducing the underprediction of Sk_u and Sk_w from 60% to 5% and 20%, respectively) and the stress fraction carried by strong sweep events (reducing the underprediction from 40% to 5%).

In this work, an upper limit ($C_{D,\max} = 0.8$, as suggested by the same experimental data) is used to cap the drag coefficient, reflecting the asymptotic regime of negligible reconfiguration in the limit of $\overline{u} \to 0$. LES runs are conducted using the constant drag coefficient model ($C_D = 0.28$, $B = 0$; case (1)) and the revised reconfiguration drag model (velocity-dependent drag coefficient model),

$$C_D = \min\left((|\tilde{\boldsymbol{u}}|/A)^B, C_{D,\max}\right), \tag{5}$$

considering a wide range of reconfiguration behavior, specifically, for cases (2) $A = 0.22$ m s^{-1}, $B = -2/3$, (3) $A = 0.38$ m s^{-1}, $B = -1$, and (4) $A = 0.48$ m s^{-1}, $B = -4/3$. In each of these four cases, the value of B is prescribed, and the values of C_D and A are found by fitting the experimental data. Recall that an increasingly negative value of B preferentially enhances the penetration of strong events into the canopy. In the fitting procedure, each value of C_D is weighted by the inverse of the velocity squared, so that higher weight is given to events of higher velocity, i.e., the conditions for which reconfiguration has the most impact on drag coefficient. Fig. 4 compares drag coefficient models with experimental data. The velocity-dependent drag coefficient model presents a similar shape to the theoretical model depicted in Fig. 1(a). Beginning at 0.3–0.6 m s^{-1}, C_D decreases with increasing velocity, and with higher dependence given by more negative values of B. In particular, note that in the high velocity range ($|\tilde{\boldsymbol{u}}| > 1.5$ m s^{-1}), C_D decreases with increasingly negative value of B, corresponding to an increased tendency for reconfiguration to reduce the drag experienced by stronger events. However, for the low velocity range ($|\tilde{\boldsymbol{u}}| < 1$ m s^{-1}), this trend is reversed, with C_D larger for more negative values of B.

B. Simulation results

LES results of turbulence statistics are compared with field experimental data computed using a period of 7.5 h (0930-1700 CDT) of steady turbulence obtained on July 10, 2011 near Mahomet, IL (dots indicating the average and error bars indicating the standard deviation for 30-min intervals in Figs. 5 and 6). Data obtained by Wilson *et al.*[53] (crosses in Fig. 5) are also shown as a consistency check, because the canopy type and structure are similar in both datasets. In addition to vertical profiles of turbulence statistics, mechanisms of momentum transport inside the canopy are

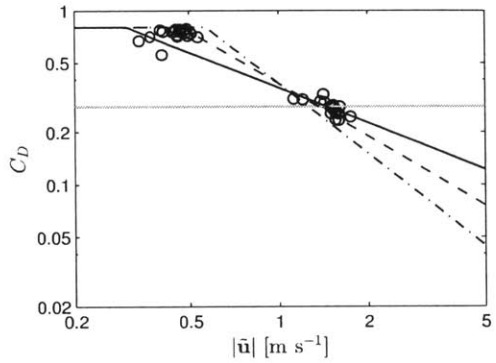

FIG. 4. Drag coefficient (C_D) against the magnitude of filtered velocity scale ($\tilde{\boldsymbol{u}}$) fitted using field experimental data (circles) and the models C_D = constant (*grey line*) and $C_D = \min\left((|\tilde{\boldsymbol{u}}|/A)^B, C_{D,\max}\right)$ (Eq. (5); black lines). Grey solid and black solid, dashed, and dashed-dotted lines indicate cases (1) $C_D = 0.28$, $B = 0$, (2) $A = 0.22$ m s^{-1}, $B = -2/3$, (3) $A = 0.38$ m s^{-1}, $B = -1$, and (4) $A = 0.48$ m s^{-1}, $B = -4/3$, respectively.

investigated using the quadrant analysis proposed by Lu and Willmarth.[54] Following the standard practices in LES studies, the mean stress $\overline{u'w'}$ (and consequently the friction velocity $u_\star = \sqrt{|\overline{u'w'}|_h}$) is determined using the resolved and subgrid-scale (SGS) parts. Standard deviations and skewness of velocity fluctuations are determined based only on the resolved scales. The vertical momentum flux is decomposed into four quadrants. Events in the first quadrant ($u' > 0$, $w' > 0$) are outward interactions, events in the second quadrant ($u'\langle 0$, $w'\rangle 0$) are ejections, events in the third quadrant ($u' < 0$, $w' < 0$) are inward interactions, and events in the fourth quadrant ($u' > 0$, $w' < 0$) are sweeps.[55] $S_{i,H}$ indicates the momentum flux carried by events in the ith quadrant that are H times stronger than the mean ($|u'w'|/|\overline{u'w'}| > H$); $S^f_{i,H} = S_{i,H}/|\overline{u'w'}|$ indicates the stress fractions carried by these events; and $S^f_H = \Sigma^4_{i=1} S^f_{i,H}$ indicates the stress fractions carried by all events that are H times stronger than the mean. In this analysis, the SGS component of the vertical momentum flux is excluded.

In Fig. 5(a), predictions of the streamwise component of time-averaged drag, $\overline{f}_{D,x}$, is negative for all four cases. The vertical integration of $\overline{f}_{D,x}$ is held approximately constant (with less than 0.5% difference across all cases), because parameters in the model $C_D = C_D(|\tilde{\boldsymbol{u}}|)$ (i.e., A and B in Eq. (5)) are fitted using the measured profile of mean vertical momentum flux (see Fig. 4). Increasingly negative values of B decrease the magnitude of $\overline{f}_{D,x}$ in the upper 20% of the canopy, where velocity falls in the high velocity range, and increase the magnitude of $\overline{f}_{D,x}$ in the lower 80% of the canopy, where velocity falls in the low velocity range. In Fig. 5(b), predictions of normalized, time-mean velocity, $\overline{u}/\overline{u}_h$, resulting from drag models with $B \neq 0$ (black lines) are distinct from those with $B = 0$ (grey line), showing better agreement with measurements inside the canopy. Specifically, using a constant C_D (assuming $B = 0$, no reconfiguration) produces an overestimation of the mean velocity inside the canopy by 100%. For second-order moments, increasingly negative values of B only slightly increases the downward momentum flux ($|\overline{u'w'}|$; Fig. 5(c)) and the standard deviation of u (σ_u; Fig. 5(e)). In other words, ignoring the effect of reconfiguration by assuming a constant C_D leads to only a slightly shallower estimation of the penetration of momentum into the canopy layer, consistent with the findings of Wilson *et al.*[53] The effects of reconfiguration on the standard deviation of v (σ_v; not shown) and w (σ_w; Fig. 5(f)) are negligible, implying that reconfiguration affects mostly the energy contained in the streamwise direction rather than spanwise or vertical directions.

The effects of the mode of reconfiguration, characterized by the negative value of B, are most pronounced for the sweep-ejection ratio ($S_{4,0}/S_{2,0}$; Fig. 5(d)) and the skewness of u (Sk_u; Fig. 5(g)) and w (Sk_w; Fig. 5(h)), with the magnitude of all three statistics increasing with increasingly negative B. The increasing magnitude of skewness arises directly from the reduction in drag coefficient with increasing velocity, which, as mentioned in Sec. I, allows stronger events to penetrate more easily

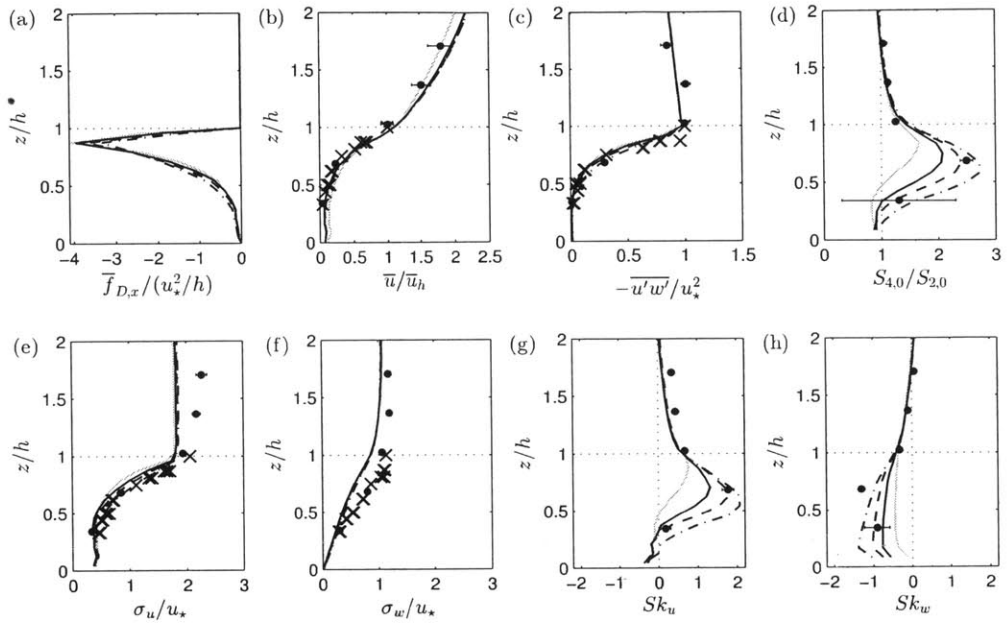

FIG. 5. LES results of (a) normalized streamwise component of mean drag ($\overline{f}_{D,x}/(u_\star^2/h)$), (b) normalized mean velocity ($\overline{u}/\overline{u}_h$), (c) normalized mean vertical momentum flux ($-\overline{u'w'}/u_\star^2$), (d) ratio between stress fractions carried by sweeps and ejections ($S_{4,0}/S_{2,0}$), (e) normalized standard deviation of u ($\sigma_u/u_\star$), (f) normalized standard deviation of w ($\sigma_w/u_\star$), (g) skewness of u (Sk_u), and (h) skewness of w (Sk_w) against normalized height (z). Here, $u_\star$ is the friction velocity, and h is the canopy height. Simulation results (lines, see Fig. 4 for representations) are evaluated against field experimental data (symbols). Dots with error bars indicate average and standard deviation for 30-min intervals of data obtained during 0900-1730 CDT on 10 July 2011 in a large maize field near Mahomet, IL,[26,52] and crosses indicate data obtained by Wilson *et al.*[53] The canopy type and structure are similar in both datasets.

into the canopy. For example, at $z/h = 2/3$, the stress fraction carried by events eight times stronger than the mean magnitude ($H = 8$) increases from 27% for $B = 0$ to 50% for $B = -1$ (Fig. 6(a)). As B becomes more negative, the deeper penetration of stronger events also makes the peak of Sk_u move towards the ground (Fig. 5(g)). Sweep events are associated with elevated streamwise velocity ($u' > 0$), and thus receive a preference in regimes for which C_D decreases with increasing U, becoming stronger when B is more negative. At $z/h = 2/3$, for example, the stress fractions carried by sweep events increase from 75% ($B = 0$) to 85% ($B = -1$) for $H = 0$ and from 25% ($B = 0$) to 50% ($B = -1$) for $H = 8$ (Fig. 6(c)). The enhancement in stress fractions increases with the strength of sweep events, showing that events with strong positive u' (large u and consequently large U) are preferentially allowed to penetrate the canopy by reconfiguration. On the other hand, ejection events associated with weaker streamwise velocity ($u' < 0$) are preferentially damped in this regime, and

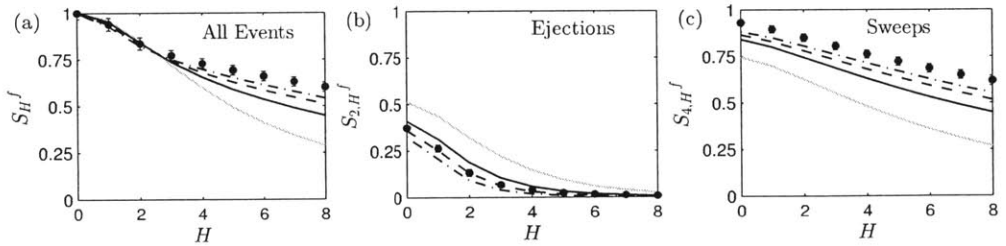

FIG. 6. Comparison of LES results and field experimental data of stress fractions carried by (a) all events (S_H^f), (b) ejections ($S_{2,H}^f$), and (c) sweeps ($S_{4,H}^f$) against hole size (H) at $z/h = 2/3$. See Fig. 5 for representations of lines and symbols.

thus become weaker when B is more negative. At $z/h = 2/3$, for example, the stress fractions carried by ejection events decrease from 50% ($B = 0$) to 35% ($B = -1$) for $H = 0$ and from 15% ($B = 0$) to negligible ($B = -1$) for $H = 4$ (Fig. 6(b)). The reduction of stress fractions occurs mostly for strong ejection events ($H \geq 4$), because ejections originate in the bottom of the canopy where lower velocity is associated with higher C_D (i.e., higher damping). The increase in sweeps and decrease in ejections both lead to the increase in the sweep-ejection ratio (Fig. 5(d)). The overall best agreement with observations across skewness and quadrant analysis occurs for $B = -1$ (black dashed lines in Figs. 5(d), 5(g), 5(h), and 6). Note that when B is fitted to data, Pan *et al.*[26] obtained $B = -0.74$. However, as seen in Fig. 4, the points calculated from the data do not constrain the fit very tightly. A new fit, which more heavily weights the large velocity portion of the data (which is more reliably measured in the field), yields $B = -0.83$. The idea that the reconfiguration of the maize plants falls in the regime of weak reconfiguration for the 1D elastic case (described in Sec. II) seems perfectly reasonable, because the simple bending observed in the field does not display deflection beyond the posture in Fig. 1(b).

IV. CONCLUSIONS

Results obtained from laboratory and numerical experiments demonstrate that concepts developed for mean reconfiguration can be extended to instantaneous reconfiguration, at least for time-scales over which the plant can respond. This provides a link between plant reconfiguration and turbulence dynamics. Although the laboratory and numerical experiments are quite different (e.g., in LAI, geometry, density, rigidity of the canopy, density of the fluid, and the rate of the flow), they show similar effects of Vogel number B on the velocity skewness. In particular, as the Vogel number becomes more negative, the peak Sk_u increases in magnitude. Specifically, LES of a maize canopy gives $Sk_{u,\max}$ of 0.8, 1.3, and 1.8 when B is specified to be 0, $-2/3$, and -1, respectively (Fig. 5(g)). Similarly, for the model seagrass meadow, the highest value of peak skewness ($Sk_{u,\max} = 1.60$, F5) occurs at the conditions associated with the most negative value of B (Fig. 3). In addition, as peak skewness (Sk_u) increases with more negative B, the peak skewness also penetrates deeper into the canopy (lower values of $z(Sk_{u,\max})/h$), as inferred from Table I and Fig. 5(d). Note that reconfiguration is not the only mechanism that affects skewness. For example, in a canopy of steel cylinders (no reconfiguration) the value of $Sk_{u,\max}$ increased from negligible to 0.8 when LAI was increased from 0.03 to 0.5.[56] In an orchard forest canopy, the value of $Sk_{u,\max}$ decreased from 1 to negligible when the atmospheric temperature stratification condition changed from neutral to free convection.[57] Our results show that, if other conditions remain unchanged, more negative values of B lead to a greater penetration of sweeps ($u' > 0$, $w' < 0$) and larger values of Sk_u. In submerged aquatic canopies, the penetration of strong sweeps to the bed could significantly elevate resuspension, so that reconfiguration (changes in B) may impact water clarity and particle retention within the bed. Further, the sweeps originating at the top of the canopy are associated with the KH coherent structures in the canopy-shear layer, so that these results are saying that plant reconfiguration may enhance the influence of these coherent structures on turbulent transport into the canopy. These modifications will certainly influence the turbulent transport of scalars and particles within the canopy, modulating the fluxes across the canopy-atmosphere or canopy-free stream interfaces. The increased dominance of sweeps over ejections in canopies with larger Vogel number is expected to favor transport of air pollutants and aerosols into vegetated regions, likely increasing the efficiency of these canopies in removing these pollutants from the atmosphere. However, further work is necessary to establish and quantify the potential impacts of canopy reconfiguration on fluxes of sensible heat, water vapor, and carbon dioxide.

For one-dimensional linear elastic reconfiguration, we highlight the importance of weak reconfiguration, which is the transition between the asymptotic regimes of negligible reconfiguration ($B = 0$) and strong reconfiguration ($B = -2/3$). In the weak reconfiguration regime, the bending length-scale is smaller than the drag length-scale, leading to a stronger dependence between drag coefficient and velocity than that observed during strong reconfiguration. In other words, the Vogel exponent is more negative ($B < -2/3$) in the weak reconfiguration regime, reaching a peak value of $B = -1.1$ at $Ca = 21$. Importantly, because weak reconfiguration produces the most negative

Vogel exponents, it also produces the strongest impact on skewness. All three regimes, including weak reconfiguration, are observed in the model seagrass meadow, and are likely present in natural canopies in which simple bending is observed, like seagrasses, stems, branches, maize, and wheat. Gosselin *et al.*[33] described a similar intermediate regime of bending for plates and disks. For strong reconfiguration, the Vogel exponent has been shown to be more negative for 2D bending ($B = -4/3$) than for 1D bending ($B = -2/3$)[29,30] and, as our LES results show, the 2D regime results in the largest predictions of skewness. A wide range of broad leaves can fold into cones and experience 2D reconfiguration, and thus enter the $-4/3$ regime.[58] Many terrestrial canopies have a Vogel number between $-2/3$ and $-4/3$,[28,30] suggesting that the classes of 1D and 2D reconfiguration identified by previous researchers for flexible strips, plates, and disks can be used to describe the reconfiguration of many plant canopies. However, a greater refinement of models may be needed for more complex plant geometries, and an exploration of the impact of canopy density on reconfiguration is also needed.

With the vertically integrated mean drag force held approximately constant, changing the mode of the reconfiguration (characterized by the Vogel number, B) has a strong impact on the mechanisms of momentum transport. The mean vertical momentum flux remains approximately the same, but the distribution, strength, and fractions of momentum carried by sweeps ($u' > 0$, $w' < 0$) and ejections ($u' < 0$, $w' > 0$) are altered significantly. Using a constant drag coefficient is capable of reproducing vertically integrated sink of momentum within the canopy layer, and consequently the first- and second-order turbulence statistics. However, accounting for the effect of reconfiguration is essential to reproduce the distribution of the momentum sink between weak ($u' < 0$) and strong ($u' > 0$) events. Therefore, higher order moments such as skewness, as well as the fractions of momentum transported by sweeps and ejections, are very sensitive to reconfiguration. These results confirm the inadequacy of describing the effects of canopy-scale coherent structures using just first- and second-order turbulence statistics. The current understanding of canopy turbulence is based on relating the properties of coherent structures to the mean drag force exerted by the canopy (one example is the penetration depth studied by Ghisalberti and Nepf[14]). Perhaps, further advances will result from understanding the drag reduction by reconfiguration and its effects on instantaneous turbulence structure.

ACKNOWLEDGMENTS

This research is supported by the National Science Foundation (NSF) Grant No. AGS1005363.

[1] S. B. Verma, D. D. Baldocchi, D. E. Anderson, D. R. Matt, and R. J. Clement, "Eddy fluxes of CO_2, water vapor, and sensible heat over a deciduous forest," Bound.-Layer Meteorol. **36**, 71–91 (1986).
[2] D. Baldocchi, "A Lagrangian random-walk model for simulating water vapor, CO_2 and sensible heat flux densities and scalar profiles over and within a soybean canopy," Bound.-Layer Meteorol. **61**, 113–144 (1992).
[3] J. D. Fuentes, T. J. Gillespie, G. Den Hartog, and H. H. Neumann, "Ozone deposition onto a deciduous forest during dry and wet conditions," Agric. For. Meteorol. **62**, 1–18 (1992).
[4] E. Lamaud, A. Carrara, Y. Brunet, A. Lopez, and A. Druilhet, "Ozone fluxes above and within a pine forest canopy in dry and wet conditions," Atmos. Environ. **36**, 77–88 (2002).
[5] S. E. Lindberg, T. P. Meyers, G. E. Taylor, R. R. Turner, and W. H. Schroeder, "Atmosphere-surface exchange of mercury in a forest: Results of modeling and gradient approaches," J. Geophys. Res. **97**, 2519–2528, doi:10.1029/91JD02831 (1992).
[6] G. Buzorius, Ü. Rannik, J. M. Mäkelä, T. Vesala, and M. Kulmala, "Vertical aerosol particle fluxes measured by eddy covariance technique using condensational particle counter," J. Aerosol Sci. **29**, 157–171 (1998).
[7] F. Di-Giovanni and P. G. Kevan, "Factors affecting pollen dynamics and its importance to pollen contamination: A review," Can. J. For. Res. **21**, 1155–1170 (1991).
[8] R. Nathan, G. G. Katul, H. S. Horn, S. M. Thomas, R. Oren, R. Avissar, S. W. Pacala, and S. A. Levin, "Mechanisms of long-distance dispersal of seeds by wind," Nature (London) **418**, 409–413 (2002).
[9] D. E. Aylor, "The role of intermittent wind in the dispersal of fungal pathogens," Annu. Rev. Phytopathol. **28**, 73–92 (1990).
[10] M. Luhar, J. Rominger, and H. Nepf, "Interaction between flow, transport and vegetation spatial structure," Environ. Fluid Mech. **8**, 423–439 (2008).
[11] S. E. Lawson, K. J. McGlathery, and P. L. Wiberg, "Enhancement of sediment suspension and nutrient flux by benthic macrophytes at low biomass," Mar. Ecol. Prog. Ser. **448**, 259–270 (2012).
[12] M. M. van Katwijk, A. R. Bos, D. C. R. Hermus, and W. Suykerbuyk, "Sediment modification by seagrass beds: Muddification and sandification induced by plant cover and environmental conditions," Estuar. Coast. Shelf Sci. **89**, 175–181 (2010).

[13] M. R. Raupach, J. J. Finnigan, and Y. Brunet, "Coherent eddies and turbulence in vegetation canopies: The mixing-layer analogy," Bound.-Layer Meteorol. **78**, 351–382 (1996).
[14] M. Ghisalberti and H. Nepf, "The structure of the shear layer in flows over rigid and flexible canopies," Environ. Fluid Mech. **6**, 277–301 (2006).
[15] R. H. Shaw, J. Tavangar, and D. P. Ward, "Structure of the Reynolds stress in a canopy layer," J. Clim. Appl. Meteorol. **22**, 1922–1931 (1983).
[16] M. Ghisalberti and H. Nepf, "Mass transport in vegetated shear flows," Environ. Fluid Mech. **5**, 527–551 (2005).
[17] C. Thomas and T. Foken, "Flux contribution of coherent structures and its implications for the exchange of energy and matter in a tall spruce canopy," Bound.-Layer Meteorol. **123**, 317–337 (2007).
[18] J. J. Finnigan, "Turbulence in plant canopies," Annu. Rev. Fluid Mech. **32**, 519–571 (2000).
[19] T. P. Meyers and D. D. Baldocchi, "The budgets of turbulent kinetic energy and Reynolds stress within and above a deciduous forest," Agric. For. Meteorol. **53**, 207–222 (1991).
[20] R. H. Shaw and U. Schumann, "Large-eddy simulation of turbulent flow above and within a forest," Bound.-Layer Meteorol. **61**, 47–64 (1992).
[21] H. B. Su, R. H. Shaw, K. T. Paw, C. H. Moeng, and P. P. Sullivan, "Turbulent statistics of neutrally stratified flow within and above a sparse forest from large-eddy simulation and field observations," Bound.-Layer Meteorol. **88**, 363–397 (1998).
[22] E. G. Patton, P. P. Sullivan, and K. J. Davis, "The influence of a forest canopy on top-down and bottom-up diffusion in the planetary boundary layer," Q. J. R. Meteorol. Soc. **129**, 1415–1434 (2003).
[23] S. Dupont and Y. Brunet, "Influence of foliar density profile on canopy flow: A large-eddy simulation study," Agric. For. Meteorol. **148**, 976–990 (2008).
[24] K. Gavrilov, D. Morvan, G. Accary, D. Lyubimov, and S. Meradji, "Numerical simulation of coherent turbulent structures and of passive scalar dispersion in a canopy sublayer," Comput. Fluids **78**, 54–62 (2013).
[25] W. Yue, M. B. Parlange, C. Meneveau, W. Zhu, R. Van Hout, and J. Katz, "Large-eddy simulation of plant canopy flows using plant-scale representation," Bound.-Layer Meteorol. **124**, 183–203 (2007).
[26] Y. Pan, M. Chamecki, and S. A. Isard, "Large-eddy simulation of turbulence and particle dispersion inside the canopy roughness sublayer," J. Fluid Mech. **753**, 499–534 (2014).
[27] S. Vogel, "Drag and flexibility in sessile organisms," Am. Zool. **24**, 37–44 (1984).
[28] B. Gaylord, C. A. Blanchette, and M. W. Denny, "Mechanical consequences of size in wave-swept algae," Ecol. Monogr. **64**, 287–313 (1994).
[29] S. Alben, M. Shelley, and J. Zhang, "Drag reduction through self-similar bending of a flexible body," Nature (London) **420**, 479–481 (2002).
[30] E. de Langre, A. Gutierrez, and J. Cossé, "On the scaling of drag reduction by reconfiguration in plants," C. R. Mec. **340**, 35–40 (2012).
[31] M. Luhar and H. M. Nepf, "Flow-induced reconfiguration of buoyant and flexible aquatic vegetation," Limnol. Oceanogr. **56**, 2003–2017 (2011).
[32] S. Alben, M. Shelley, and J. Zhang, "How flexibility induces streamlining in a two-dimensional flow," Phys. Fluids **16**, 1694–1713 (2004).
[33] F. Gosselin, E. de Langre, and B. Machado-Almeida, "Drag reduction of flexible plates by reconfiguration," J. Fluid Mech. **650**, 319–341 (2010).
[34] I. Albayrak, V. Nikora, O. Miler, and M. O'Hare, "Flow-plant interactions at a leaf scale: Effects of leaf shape, serration, roughness and flexural rigidity," Aquat. Sci. **74**, 267–286 (2012).
[35] D. L. Harder, O. Speck, C. L. Hurd, and T. Speck, "Reconfiguration as a prerequisite for survival in highly unstable flow-dominated habitats," J. Plant Growth Regul. **23**, 98–107 (2004).
[36] A. Koizumi, J. Motoyama, K. Sawata, Y. Sasaki, and T. Hirai, "Evaluation of drag coefficients of poplar-tree crowns by a field test method," J. Wood Sci. **56**, 189–193 (2010).
[37] J. J. Finnigan, "Turbulence in waving wheat," Bound.-Layer Meteorol. **16**, 181–211 (1979).
[38] M. Ghisalberti and H. M. Nepf, "Mixing layers and coherent structures in vegetated aquatic flows," J. Geophys. Res. **107**, 3-1–3-11, doi:10.1029/2001JC000871 (2002).
[39] S. E. Belcher, N. Jerram, and J. C. R. Hunt, "Adjustment of a turbulent boundary layer to a canopy of roughness elements," J. Fluid Mech. **488**, 369–398 (2003).
[40] J. Rominger and H. M. Nepf, "Flow adjustment and interior flow associated with a rectangular porous obstruction," J. Fluid Mech. **680**, 636–659 (2011).
[41] M. A. Abdelrhman, "Modeling coupling between eelgrass *Zostera marina* and water flow," Mar. Ecol. Prog. Ser. **338**, 81–96 (2007).
[42] M. W. Denny, B. P. Gaylord, and E. A. Cowen, "Flow and flexibility. II. The roles of size and shape in determining wave forces on the bull kelp *Nereocystis luetkeana*," J. Exp. Biol. **200**, 3165–3183 (1997).
[43] H. L. Stewart, "Morphological variation and phenotypic plasticity of buoyancy in the macroalga *Turbinaria ornata* across a barrier reef," Marine Biol. **149**, 721–730 (2006).
[44] B. Statzner, N. Lamouroux, V. Nikora, and P. Sagnes, "The debate about drag and reconfiguration of freshwater macrophytes: Comparing results obtained by three recently discussed approaches," Freshwater Biol. **51**, 2173–2183 (2006).
[45] H. M. Nepf, "Flow and transport in regions with aquatic vegetation," Annu. Rev. Fluid Mech. **44**, 123–142 (2012).
[46] S. Ikeda and M. Kanazawa, "Three-dimensional organized vortices above flexible water plants," J. Hydraul. Eng. **122**, 634–640 (1996).
[47] M. Luhar and H. M. Nepf, "From the blade scale to the reach scale: A characterization of aquatic vegetative drag," Adv. Water Resour. **51**, 305–316 (2013).
[48] Z. Chen, C. Jiang, and H. Nepf, "Flow adjustment at the leading edge of a submerged aquatic canopy," Water Resour. Res. **49**, 5537–5551, doi:10.1002/wrcr.20403 (2013).

[49] T. V. Prabha, M. Y. Leclerc, and D. Baldocchi, "Comparison of in-canopy flux footprints between large-eddy simulation and the Lagrangian simulation," J. Appl. Meteorol. Climat. **47**, 2115–2128 (2008).
[50] M. Kanda and M. Hino, "Organized structures in developing turbulent flow within and above a plant canopy, using a large eddy simulation," Bound.-Layer Meteorol. **68**, 237–257 (1994).
[51] A. Cescatti and B. Marcolla, "Drag coefficient and turbulence intensity in conifer canopies," Agric. For. Meteorol. **121**, 197–206 (2004).
[52] S. C. Gleicher, M. Chamecki, S. A. Isard, Y. Pan, and G. G. Katul, "Interpreting three-dimensional spore concentration measurements and escape fraction in a crop canopy using a coupled Eulerian-Lagrangian stochastic model," Agric. For. Meteorol. **194**, 118–131 (2014).
[53] J. D. Wilson, D. P. Ward, G. W. Thurtell, and G. E. Kidd, "Statistics of atmospheric turbulence within and above a corn canopy," Bound.-Layer Meteorol. **24**, 495–519 (1982).
[54] S. S. Lu and W. W. Willmarth, "Measurements of the structure of the Reynolds stress in a turbulent boundary layer," J. Fluid Mech. **60**, 481–511 (1973).
[55] W. W. Willmarth, "Structure of turbulence in boundary layers," Adv. Appl. Mech. **15**, 159–254 (1975).
[56] D. Poggi, A. Porporato, L. Ridolfi, J. D. Albertson, and G. G. Katul, "The effect of vegetation density on canopy sub-layer turbulence," Bound.-Layer Meteorol. **111**, 565–587 (2004).
[57] S. Dupont and E. G. Patton, "Influence of stability and seasonal canopy changes on micrometeorology within and above an orchard canopy: The CHATS experiment," Agric. For. Meteorol. **157**, 11–29 (2012).
[58] L. A. Miller, A. Santhanakrishnan, S. Jones, C. Hamlet, K. Mertens, and L. Zhu, "Reconfiguration and the reduction of vortex-induced vibrations in broad leaves," J. Exp. Biol. **215**, 2716–2727 (2012).

Chapter 5

Evaluation of a random displacement model for predicting particle escape from canopies using a simple eddy diffusivity model [1]

[1]This chapter has been previously copyrighted by Elsevier Ltd. and is therefore excluded from the MIT copyright covering other chapters of this thesis. Citation: Follett, E., Chamecki, M., Nepf, H., 2016. Evaluation of a random displacement model for predicting particle escape from canopies using a simple eddy diffusivity model. Agricultural and Forest Meteorology 224, 40-48

Agricultural and Forest Meteorology 224 (2016) 40–48

Contents lists available at ScienceDirect

Agricultural and Forest Meteorology

journal homepage: www.elsevier.com/locate/agrformet

Evaluation of a random displacement model for predicting particle escape from canopies using a simple eddy diffusivity model

Elizabeth Follett[a,*], Marcelo Chamecki[b], Heidi Nepf[a]

[a] Department of Civil and Environmental Engineering, Massachusetts Institute of Technology, 77 Massachusetts Avenue Room 1-290, Cambridge, MA, 02139, USA

[b] Department of Meteorology, The Pennsylvania State University, 503 Walker Building, University Park, PA, 16802, USA

ARTICLE INFO

Article history:
Received 23 December 2014
Received in revised form 31 March 2016
Accepted 6 April 2016

Keywords:
Particle transport
Escape of particles from canopy
Eddy diffusivity
Random displacement model
Maize

ABSTRACT

There is a need for more practical tools for estimating spore escape from crop canopies, which is essential in forecasting the propagation of disease to other fields. In this paper, we evaluated whether a random displacement model (RDM) parameterized with an eddy diffusivity $K_z(z)$ could be used to predict spore escape probability. The proposed RDM does not require detailed turbulence measurements for parameterization. Instead, it constructs profiles of velocity and eddy diffusivity from a simple set of parameters [canopy height, canopy density, vegetation length scale, and wind speed]. The RDM was validated using field measurements of spore concentration. On average, the model predictions matched the field measurements within 28% inside the canopy and 42% above it, comparable to LES results over the same canopy. Once validated, the RDM was used to explore particle escape across a range of canopy densities and particle settling velocities, in order to inform estimates of particle escape from crops of varying maturity or area density. Escape fraction as calculated by the RDM increased as canopy density decreased, as the ratio of particle settling velocity to turbulent shear velocity ratio decreased, and as the source height within the canopy increased.

1. Introduction

Fungicides are used in agricultural production to reduce losses due to fungal disease. Unfortunately, some fungicide components are transported into freshwater systems, causing sub-lethal effects on ecosystem processes, including fish reproduction and leaf decomposition (Elskus, 2014). Therefore, for both economic and ecologic reasons, it is desirable to reduce the amount of fungicides applied to crops, while maintaining their benefits to crop yield. Integrated Pest Management (IPM) reduces fungicide use by targeting applications to when the pathogen is most vulnerable (Roberts and Reigart, 2013). Because chemical treatments are most effective during the first stages of fungal infection, it is necessary to forecast the spread of fungal spores to effectively time fungicide applications (Aylor, 1999). Therefore, an understanding of spore aerial transport is essential to the development of IPM strategies (Aylor and Irwin, 1999). For example, by correctly forecasting low soybean rust inoculum production and transport, the Integrated Aerobiology Monitoring System (IAMS) saved US soybean producers between $11 and $229 million in fungicide costs in 2005 (Isard et al., 2007). Evaluation of long distance spore transport must integrate the fungal life cycle, including spore release, escape from the canopy, transport and survival in the atmosphere, deposition on a new host, and infection of the host to generate new spores (Aylor 1986, 1990). This paper examines spore escape from the canopy, which depends on physical factors that determine the relative importance of turbulent transport within the canopy, promoting escape, and spore settling, promoting deposition to the canopy and ground (e.g. Aylor and Taylor, 1983; Aylor, 1999; Aylor and Flesch, 2001; Nathan and Katul, 2005).

The vertical structure of turbulence within a canopy is dependent on the canopy morphology, which is characterized by the canopy height (h) and the plant frontal area per unit canopy volume (a_f). The dimensionless canopy density, or roughness density, is defined as $a_f h$. If the canopy density is high ($a_f h \gtrsim 0.1$), like most terrestrial crops, the drag imparted by the canopy is sufficient to generate an inflection point in the velocity profile, which leads to the generation of canopy-scale coherent structures at the top of the canopy through the Kelvin-Helmholtz instability (Raupach et al., 1996; Nepf, 2012). The canopy-scale vortices dominate the vertical turbulent transport of momentum and scalars, including

* Corresponding author.
E-mail addresses: emf@alum.mit.edu (E. Follett), chamecki@psu.edu (M. Chamecki), hmnepf@mit.edu (H. Nepf).

http://dx.doi.org/10.1016/j.agrformet.2016.04.004
0168-1923/

spores, at the top of the canopy (Shaw et al., 1983; Ghisalberti and Nepf, 2005, 2006; Thomas and Foken, 2007). The region of the canopy flushed by these vortices is termed the exchange zone. The exchange zone extends from the top of the canopy over a distance $\delta_e = (0.23 \pm 0.06) / (C_D a_f)$, called the penetration length scale, with C_D the canopy drag coefficient defined using a quadratic drag that includes the prefactor ½ (Nepf et al., 2007).

Below the exchange zone exists a relatively quiescent region, termed the wake zone, within which turbulence is dominated by stem scale wakes, so that the vertical transport is greatly diminished relative to that in the exchange zone (Nepf et al., 2007). Because of the difference in vertical turbulent transport, spores originating in the wake zone, i.e., below the penetration of canopy-scale vortices, should have less likelihood of escaping the canopy than spores originating in the exchange zone, which can be flushed out by the canopy-scale vortices. Since the exchange zone decreases with increasing canopy density, the escape fraction should also decrease with increasing canopy density. The likelihood of particle escape also depends on the particle's size and density, which dictate its settling velocity, w_s (Aylor, 1990, 1999).

Some researchers (e.g. Pan et al., 2014) have simulated particle transport in canopy flow using large eddy simulation (LES), which resolves large scales of turbulence, but represents the impact of small-scale turbulence using sub-grid scale parameterization. However, LES requires significant time and computational resources, precluding the investigation of a wide parameter space. For a less computationally intensive approach, researchers have proposed various forms of Lagrangian stochastic models (LSM), which produce ensembles of stochastic spore trajectories. Turbulence is represented through second or third-order turbulent correlations, which are typically parameterized using measured profiles of velocity variance, turbulent momentum flux, and TKE dissipation rate (Aylor, 1990; de Jong et al., 1991; Aylor and Flesch, 2001; de Jong, 1992; Andrade et al., 2009). In this paper we propose a random displacement model (RDM) that uses an eddy diffusivity to represent turbulent transport. The proposed RDM does not require the measurement of detailed velocity statistics or significant computational resources, so that it could be a valuable tool for driving models of long-range spore transport by providing rapid estimation of escape fraction from crops of varying maturity or area density. This approach assumes that turbulent motions are uncorrelated, so that the time averaged turbulent fluxes act as an enhanced Fickian diffusion, described by a turbulent diffusion coefficient K_z (Legg and Powell, 1979; Aylor, 1982, 1990; Aylor and Taylor, 1983; Denmead and Bradley, 1987). Because spores are released over hours, which is long compared to the duration of individual sweeps and ejections (6–10 s, Denmead and Bradley, 1987; Chamecki, 2013), an uncorrelated model should reasonably represent the time-averaged escape behavior. Previous work has estimated eddy diffusivity from a canopy heat balance, or by using second-order turbulence statistics to represent the time-mean eddy diffusivity, $K_z = \sigma_w^2 T_L$, with Lagrangian time scale $T_L = 2\sigma_w^2 / C_0 \varepsilon$, with C_0 a universal constant and ε the rate of turbulence dissipation (Durbin, 1983; Legg and Powell, 1979; Wilson and Sawford, 1996). However, these approaches require detailed, canopy-specific measurements of turbulence statistics. In the proposed RDM, the velocity and eddy diffusivity profiles within and above a canopy were constructed from existing equations for a neutral boundary layer using a simple set of parameters [canopy height, canopy density, vegetation length scale, and wind speed]. The RDM performance was evaluated through a comparison to measured field data. After validation, the RDM was used to explore the trends in escape fraction over a range of canopy densities ($C_D a_f h = 0.1$ to 7), a range of settling velocities ($w_s/u_* = 0$ to 1), and as a function of particle source height, z_{src}/h (0 to 1, subscript 'src' denotes 'source').

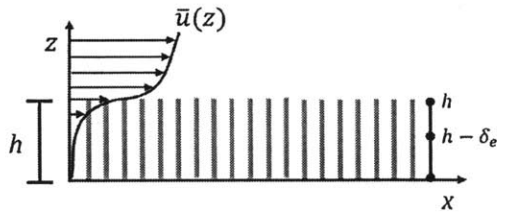

Fig. 1. Schematic diagram of the lower part of the model domain, which extends to $z = 10h$. The longitudinal direction is x, the vertical direction is z, with $z = 0$ at the ground, the canopy height is h, and the time-averaged longitudinal velocity is $\bar{u}(z)$.

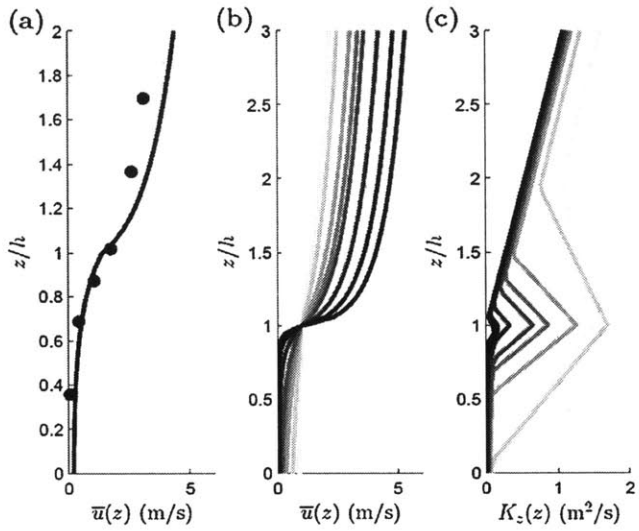

Fig. 2. (a) time-averaged velocity $\bar{u}(z)$ (m/s) predicted from eqs. (7) to (10) shown by solid line and measured over a maize field (Gleicher et al., 2014), shown by dots. Family of curves describing (b) time-averaged streamwise velocity $\bar{u}(z)$ (m/s) and (c) vertical turbulent diffusivity $K_z(z)$ (m²/s) predicted from eqs. (7) to (18). From light to dark, curves represent increasing canopy density, with $C_D a_f h$ = 0.1, 0.25, 0.5, 0.75, 1, 2, 4, and 7, respectively, with $u_* = 0.51$ m/s, $h = 2.1$ m, L_v = 0.1 m, and $C_D = 0.68$ for all curves, based on a maize canopy, as described in the text.

2. Methods

The RDM simulated a 2D domain (Figs. 1 and 2) with the coordinates x and z parallel and normal to the ground, respectively. The velocity vector $\vec{u} = (u, w)$ corresponded to the streamwise and vertical coordinates (x, z), respectively. The time average and turbulent components of velocity were denoted by an overbar (e.g. $\bar{u}$) and prime (e.g. u'), respectively. Individual particles originated at a specific source height, z_{src}, within the canopy ($0 < z_{src} < h$) and were tracked until they deposited on the canopy, settled to the ground, or left the modeling domain. Particles that reached $z/h = 10$ were assumed to have left the domain and were no longer tracked. The number of particles per run (1000) was selected based on the fact that results with 1000 particles differed from results with 10,000 particles by less than 5 percent. The size of the model domain (x, z) was $18h$ x $10h$. The sensitivity of results to domain size was evaluated by comparing 10 runs with a domain of $18h$ x $10h$ to 10 runs with a domain of $200h$ x $10h$. The difference between escape fraction values determined in the two domains was less than 2%, indicating that the domain size did not significantly affect model results.

In each constant time-step (Δt) the position of the particle (x_p, z_p) advanced longitudinally with the mean velocity $\bar{u}$ and vertically due to both settling (w_s) and turbulent transport (w'). The

equations used to model the particle position were (Wilson and Sawford, 1996):

$$x_{p,i+1} = x_{p,i} + \bar{u}\left(z_{p,i}\right)\Delta t \tag{1}$$

$$z_{p,i+1} = z_{p,i} + \left(\frac{dK_z}{dz}(z_{p,i}) - w_s\right)\Delta t + R\sqrt{2K_z(z_{p,i})\Delta t} \tag{2}$$

The last term in (2) represents transport by turbulent velocity $w' = R\sqrt{2K_z}/\sqrt{\Delta t}$, and R a random number drawn from a normal distribution with mean 0 and standard deviation 1. The vertical transport also included a drift correction, or pseudovelocity, associated with the vertical variation in diffusivity $\left(dK_z/dz\right)$. The pseudovelocity term prevented the artificial accumulation of particles in regions of low diffusivity (Durbin, 1983; Boughton and Delaurentis, 1987; Wilson and Sawford, 1996; Wilson and Yee, 2007). The formulations for the vertical profiles of time-mean streamwise velocity, $\bar{u}(z)$, and eddy diffusivity, $K_z(z)$ are described below in Section 2.1. The particle position was saved at every time-step. The model time-step, Δt, was constrained so that the vertical particle excursion within each time-step was much smaller than the scale of vertical gradients in the diffusivity and velocity (Israelsson et al., 2006). Within the model canopy, both the velocity and diffusivity varied over length scales of approximately 0.1 h. For each run the time-step satisfied the following condition:

$$\Delta t < \min\left(\frac{0.1h}{\left|\frac{\partial K_z}{\partial z} - w_s\right|_{max}}, \frac{(0.1h)^2}{K_z|_{max}}\right) \tag{3}$$

Within each time-step, after a particle was moved, the position was assessed to determine if the particle had settled to the ground $\left(z_{p,i} = 0\right)$; escaped the canopy $\left(z_{p,i} > h\right)$ escaped the model domain $\left(z_{p,i} > 10h \text{ or } x_{p,i} > 18h\right)$; or deposited to the canopy. For a continuous release, as considered here, the fraction of spores escaping the canopy is a function of distance from the source, but not time. As described in Pan et al. (2014), the escape fraction initially increases with distance from the source, reaching a maximum at $x/h = 2$ to 6, depending on settling velocity (Fig. 7 in Pan et al., 2014). Since the canopy is a sink for particles, over longer distances particles may return to the canopy through turbulent transport or settling and be deposited, so that at larger distances the escape fraction exhibits a slow decline with distance. To provide a single, consistent metric with which to compare different scenarios in Section 3.2, we adopt the escape fraction metric (EF) defined by Pan et al. (2014) as the maximum fraction of the released particles observed above the canopy.Canopy deposition was described using a modified version of the model given in Aylor and Flesch (2001). Deposition on vertical facing and upward facing surfaces was possible if the velocity was less than the critical velocity $u_{crit} = 0.45$ m/s, determined by Aylor (2005) for pollen capture in a maize canopy. Particle rebound and re-entrainment was expected if the particle velocity was greater than u_{crit}. We caution that the value of u_{crit} may vary with particle type (pollen versus spores), and also with canopy rigidity and morphology. Following Pan et al. (2014), deposition on downward facing surfaces was neglected. Deposition on upward facing surfaces was possible if the particle had a negative vertical particle excursion, $z_{p,i+1} - z_{p,i} < 0$. The rate of deposition on an upward facing surface (S_u) was calculated as the product of the two-sided leaf area density, $a(z)$, the fractional projected leaf area normal to the vertical direction (P_z), and the settling velocity:

$$S_u = P_z a(z) w_s \tag{4}$$

(Pan et al., 2014, eq. A2) described particle deposition to vertical surfaces in a three-dimensional domain. Here, we modified the formulation for the two-dimensional domain ($x - z$) of this RDM. Specifically, the projected area in the x direction was assumed to be the sum of the measured projected leaf area facing the x (P_x) and y $\left(P_y\right)$ directions in 3D space $\left(P_{x,2D} = P_x + P_y\right)$, and the rate of impaction depended only on the mean longitudinal velocity ($\bar{u}$) since $\bar{v} = 0$ in the 2D domain. The rate of deposition on vertical surfaces (S_v) is then given by:

$$S_v = EI\left(P_{x,2D}\right) a(z) \bar{u} \tag{5}$$

with impaction efficiency (EI),

$$EI = 0.86\left(1 + 0.442St^{-1.967}\right)^{-1} \tag{6}$$

based on Aylor (1982). In Eq. (6), St is the Stokes number $St = w_s\bar{u}/gL_v$, with L_v the characteristic length scale of the canopy elements and g the gravitational acceleration. Because the RDM tracked individual particles, the time rate of deposition given by (4) through (6) was converted to a probability for individual particle deposition during one time-step. Following Aylor and Ferrandino (1989), the rate of deposition, $S_u + S_v$, was multiplied by Δt, resulting in a number between 0 and 1 that represented the probability of deposition during that time-step. The need to keep the fraction of particles deposited in each time-step less than 1 imposed an additional constraint on the time-step; however, this condition was satisfied by the more stringent constraints on the vertical particle excursion (Eq. (3)). To determine if the particle deposited during the time-step, a random number, R_c, was chosen from a uniform distribution between 0 and 1. If R_c was less than or equal to the probability of deposition, the particle deposited to the canopy.

2.1. Velocity and eddy diffusivity profiles to parameterize RDM

Several previous studies were combined to describe $\bar{u}(z)$ and $K_z(z)$ as functions of only u_*, $a_f h$, h, L_v, and C_D. The friction velocity (u_*) is defined at the top of the canopy, $u_*^4 = \left(\overline{u'w'}\right)_h^2 + \left(\overline{v'w'}\right)_h^2$ (In this paper, the velocity field is assumed to be aligned with x and uniform in y, so that $\overline{v'w'} = 0$). Profiles were only constructed for dense canopies $\left(a_f h \gtrsim 0.1\right)$, representative of most terrestrial crops. Within the canopy the profiles are divided into two regions. In the wake zone $\left(z < h - \delta_e\right)$, both K_z and $\bar{u}$ are small, so particle transport is likely dominated by settling (w_s). In the exchange zone $\left(z \geq h - \delta_e\right)$, canopy-scale vortices elevate K_z and contribute to greater momentum penetration from above, and thus higher $\bar{u}$, so that both turbulent transport and capture to the canopy may become important processes for spore transport.

First, the profile for the mean longitudinal velocity is described. Above a dense canopy, there is a displaced boundary-layer profile:

$$\bar{u}(z) = \frac{u_*}{\kappa} ln\left(\frac{z - z_m}{z_0}\right) \tag{7}$$

in which $\kappa = 0.4$ is the von Kármán constant (Raupach, 1994; Thom, 1971). The displacement height (z_m) and roughness height (z_0) are both functions of canopy density (e.g. Schlichting 1936; Grimmond and Oke, 1999). Following Luhar et al. (2008), the displacement height z_m and roughness height z_o can be described in terms of $C_D a_f h$,

$$\frac{z_m}{h} = 1 - \frac{0.12}{C_D a_f h} \tag{8}$$

$$\frac{z_o}{h} = 0.04\left(C_D a_f h\right)^{-1} \qquad C_D a_f h \geq 0.1 \tag{9}$$

The velocity inside the canopy follows an exponential decay, e.g. combining Harman and Finnigan (2007) and Nepf (2012):

$$\bar{u}(z) = u_1 + (u_h - u_1) e^{\frac{\beta(z-h)}{l}} \tag{10}$$

in which u_h is the velocity at the top of the canopy, and u_1 is the velocity in the lower canopy (wake zone), below the penetration of vertical turbulent momentum flux. The ratio u_1/u_h decreases with

Table 1
Description of parameters used for each set of simulations.

Figure	w_s/u_*	$a_f h$	h(m)
2a	–	1.65	2.1
2b,c	–	0.15 – 10.29	2.1
3	0.04	1.65	2.1
4	0.01 – 1	1.65	2.1
5a–d	0, 0.1, 1, 5	0.15 – 10.29	2.1
5e,f	0, 0.1	0.15 – 10.29	0.067 – 4.67
Gleicher et al. (2014)	0.04	1.65	2.1

$C_D = 0.68$, $u_* = 0.51$ m/s, $L_v = 0.1$m in all figures

increasing canopy density, and the following relation was determined by fitting data from terrestrial canopies reported in Fig. 1 and Table 1 in Finnigan (2000):

$$u_1/u_h = 0.16\left(a_f h\right)^{-0.68} \tag{11}$$

Given u_*, Eq. (7) to (9) predict the velocity at the top of the canopy, $u_h = u(h)$. Specifically, $u_h/u_* = 2.7$ for all values of a_f, which is consistent with observations made across a wide range of dense aquatic and terrestrial canopies (Ghisalberti, 2009). The velocity-decay length-scale (l/β in 10) can be determined using a mixing length (l) characterization of eddy viscosity, which leads to $\beta = u_*/u_h$ and $l = 2\beta^3/C_D a_f$ (Harman and Finnigan, 2007).

Next, consider the vertical profile of eddy diffusivity. Previous parameterizations of eddy diffusivity, such as Massman and Weil (1999), do not reflect the contributions of the coherent structures at the top of the canopy, or the role of the plant-scale vortices within the canopy, both of which have been recently shown to provide important controls on the magnitude of diffusivity within the canopy (Poggi et al., 2004; Tanino and Nepf, 2008). The models used here incorporate both of these important length-scales. In the wake zone $\left(z < h - \delta_e\right)$ the diffusivity is dominated by plant-scale turbulence, and K_z scales on the characteristic vegetation length scale (L_v) and the velocity scale $\sqrt{k_t}$ associated with the turbulent kinetic energy (k_t) generated in the plant wakes (Raupach et al., 1996; Finnigan, 2000; Tanino and Nepf, 2008). Tanino and Nepf (2008) developed models for k_t and K_z as functions of canopy morphology (L_v and a_f) and local velocity ($\bar{u}$). Most crops have a low solid volume fraction ($\phi = a_f t$, with t the blade thickness), such that plant-scale eddies can exist throughout the canopy and have scale L_v, so that equations (2.12) and (2.15) in Tanino and Nepf (2008) reduce to:

$$\frac{K_z}{\bar{u}L_v} = 4.5\left(\frac{\sqrt{k_t}}{\bar{u}}\right) \tag{12}$$

$$\frac{\sqrt{k_t}}{\bar{u}} = 1.1\left(C_D\frac{a_f L_v}{2}\right)^{1/3} \tag{13}$$

in which the scale coefficients (1.1 and 4.5) were determined in laboratory experiments (Tanino and Nepf, 2008).

In the upper canopy $\left(h - \delta_e < z < h\right)$, the flow resembles a mixing layer (Raupach et al., 1996), within which the eddy diffusivity follows a mixing length model (e.g. Poggi et al., 2004),

$$K_z(z) = \left(\frac{1}{Sc}\right) {l_{eff}}^2 \partial\bar{u}/\partial z \tag{14}$$

with effective eddy length-scale l_{eff}. The turbulent Schmidt number, Sc, was assumed to be equal to 0.5, as in a mixing layer (Raupach et al., 1996). This is consistent with recent laboratory experiments for which Sc equal to 0.47 was measured within and above a model canopy in a neutrally stable flow (Ghisalberti and Nepf, 2005). A range of Sc values between 0.5 and 1 has been observed above crop canopies, with Sc increasing with atmospheric stability and dependent on scalar species (Wilson, 2013).

Using $u_h/u_* = 2.7$ (determined above), the velocity-decay length-scale in (10) is $l/\beta = 2\beta^2/C_D a_f = 0.27/\left(C_D a_f\right) \approx \delta_e$, such that it is reasonable to approximate $\partial u/\partial z|_{z=h} = u_h/\delta_e$ in (14). Thus, the diffusivity at the top of the canopy ($z = h$) is $K_h = 2{l_{eff}}^2 u_h/\delta_e$, which is the local maximum in diffusivity. For simplicity, a linear transition was assumed between K_h at $z = h$ and the lower canopy value given by Eq. (12) at $z = h - \delta_e$. The contribution of the mixing-layer vortices to K_z was assumed to be symmetric about $z = h$, such that the eddy diffusivity decays over the same length scale, δ_e, above the canopy.

Following Poggi et al. (2004), the effective eddy length-scale $\left(l_{eff}\right)$ is a combination of the mixing-layer (l_{ML}) and boundary-layer (l_{BL}) length scales:

$$l_{eff} = (1-\alpha)\, l_{BL} + \alpha l_{ML} \tag{15}$$

$$l_{BL} = \kappa(z - z_m) \tag{16}$$

$$l_{ML} = \frac{2}{C_D a_f}\beta^2 \tag{17}$$

The relative contribution of the mixing layer length scale (α) is a function of $C_D a_f h$. Figs. 8 and 9 from Poggi et al. (2004) showed that α reached an asymptote of $\alpha = 0.45$ for $C_D a_f h \geq 0.6$, and $\alpha = 0.25$ to 0.45 over the range $C_D a_f h = 0.1 - 0.6$. Using $u_h/u_* = 2.7$ (determined above), $\beta = u_*/u_h = 0.37$, which leads to $l_{ML} = 0.27\left(C_D a_f\right)^{-1} \approx \delta_e$; i.e., the eddy length scale in the mixing layer corresponds to the length scale of turbulence penetration into the canopy. Note that as $C_D a_f$ approaches zero, (17) implies that l_{ML} is unbounded, which is not physically reasonable. To correct this, l_{ML} is constrained to be the minimum of Eq. (17) and h. Finally, above $z = h + \delta_e$, the eddy diffusivity follows the boundary-layer form,

$$K_z(z) = \left(\frac{1}{Sc}\right)\kappa u_*(z - z_m) \qquad z > h + \delta_e \tag{18}$$

with $Sc = 0.8$ for a boundary layer (Launder, 1976; Hassid, 1983; Koeltzsch, 2000).

Fig. 2a shows velocity measured in a maize field (dots) and the time-averaged velocity constructed from Eqs. (7) through (10) using parameters from that maize field, specifically $u_* = 0.51$ ms^{-1}, $h = 2.1$ m, and $LAI = 3.3$. (Gleicher et al., 2014). Following Finnigan (2000), the frontal area density was assumed to equal ½ the one-sided leaf area index, $a_f h = \frac{1}{2}$LAI. Wilson et al. (1982) measured $C_D = 0.17$ for maize, but used a drag formulation that excludes the factor of 1/2, which we include, and used the single-sided leaf area, whereas we use $\frac{1}{2}LAI$. To compensate, we adjusted C_D by a factor of 4, such that $C_D = 0.68$. Using only the reported values of u_*, h, C_D and LAI the constructed velocity profile (solid line in Fig. 2a) agreed with the measured velocity (dots in Fig. 2a) to within 0.26 m/s inside the canopy $\left(z/h \leq 1\right)$, and to within 0.85 m/s above the canopy $\left(1 < z/h \leq 1.7\right)$.

Fig. 2b and c show the family of curves constructed from Eqs. (7) through (18) using $C_D a_f h = 0.1$–7. The velocity profiles resemble the family of measured velocity profiles shown in Fig. 1 of Finnigan (2000). Recall that only dense canopies have been considered $\left(C_D a_f h > 0.1\right)$, and consistent with this each velocity profile resembles a mixing layer, with a velocity inflection point at the top of the canopy. Importantly, the model captures the peak in diffusivity at the top of the canopy (Fig. 2c) associated with the coherent structures formed in the mixing-layer, a feature that is not captured by the model proposed by Massman and Weil (1999), but which is clearly evident in measured profiles of K_z (Ghisalberti and Nepf, 2005). At the lowest densities considered (lightest lines), the coherent structures penetrate to the ground $\left(\delta_e = h\right)$, elevating diffusivity over the full canopy. As canopy density increases, the exchange zone decreases in size $\left(\delta_e \sim (C_D a_f)^{-1}\right)$. The mixing

layer eddy length-scale, $l_{ML} \sim (C_D a_f)^{-1}$, also decreases, leading to a diminished diffusivity at the top of the canopy.

3. Results and discussion

3.1. Validation using field data from maize canopy

The RDM was validated against measurements from a field release of *Lycopodium* spores ($w_s = 1.94$ cms^{-1}) in a maize canopy (Gleicher et al., 2014), which is the same study used for comparison in Fig. 2a. Gleicher et al. (2014) report $u_* = 0.51$ m/s, $h = 2.1$ m, $LAI = 3.3$.The characteristic vegetation length scale is the leaf width, $L_v = 0.1$ m (Silva et al., 2012). Gleicher released spores from a single pole at three source heights $z_{src}/h = 1, 2/3, 1/3$ and captured spores using a grid of 9 poles, with 5 rotorods per pole ($x/h = 0.94, 1.9, 3.8, y/h = -0.36, 0, 0.36$, $z/h = 0.34, 0.68, 1.0, 1.4, 1.7$, $h = 2.1$ m). Rotorod data was missing from three locations $x/h = 1.9, 3.8$, $y/h = 0.36$, so data for these three rotorod locations was taken from the corresponding rotorods at the opposite poles $x/h = 1.9, 3.8$, $y/h = -0.36$.

We calculated concentration and airborne flux in the RDM using a method similar to Gleicher et al. (2014). A vertical column of interrogation boxes (0.2 m long x 0.1 m high) was defined, centered at the field data collection points. The particle concentration was found by dividing the number of airborne particles in each box by the box area. Particles were continuously released until a steady-state particle concentration was established in each box. Because RDM is two dimensional in x-z, it cannot represent the lateral dispersion present in the field. Therefore, the field data was adjusted to correct for the fraction of particles lost from the control volume by lateral dispersion. Specifically, the field data was normalized by the equivalent two-dimensional flux represented within the measurement volume, $Q_x = \int_{-0.76m}^{0.76m}\int_{0.7m}^{3.5m} \bar{u}C dz dy$), with the integral approximated by trapezoidal summation. A laterally-integrated concentration was found from the measurements at the three y locations $\left(\langle C\rangle = \int_{-0.76m}^{0.76m} C(x,y,z)dy\right)$, which has units of spores m^{-2}. The concentration within the 2-D RDM was, by definition, the laterally-integrated value, C. The RDM concentration was scaled by the two-dimensional flux at each x location ($Q_x = \int_{0.7m}^{3.5m} \bar{u}\langle C\rangle dz$, which has units of spores s^{-1}), with the integral approximated by trapezoidal sums. Using this method, both the RDM and field normalized flux profiles $\bar{u}\langle C\rangle/Q_x$ integrate to 1.

The field measurement and predicted spore concentrations are shown in Fig. 3. With $\bar{u}(z)$ and $K_z(z)$ predicted from Eqs. (7) to (18) using the measured canopy parameters from Gleicher (summarized in Table 1), 73% of the predicted spore concentrations were within a factor of 2 of the field observations ($FAC2 = 73\%$; fraction of data that satisfy $0.5 \le C_p/C_f \le 2.0$), with (C_p) and (C_f) representing the predicted and field values, respectively (Chang and Hanna, 2008). The agreement improved with distance from the source (Fig. 3g,h,i; Table 2), which is consistent with the expectation that the RDM makes better predictions in the far-field. At the farthest measurement point $(x/h = 3.8)$, and for all source heights, the prediction concentrations were, on average, 1.28 times the field measurements within the canopy and 0.58 times the field measurements above it. The underprediction of concentration above the canopy may have been related to the overprediction of $\bar{u}$ in this region (see Fig. 2a).

For additional comparisons, the geometric mean bias (VG) and ratio of geometric means, or mean geometric bias (MG) were also assessed (Hanna, 2003; Chang and Hanna, 2004):

$$VG = e^{\left(\widetilde{\ln\frac{C_f}{C_p}}\right)^2} \quad (19)$$

Table 2
Fraction of RDM predictions within a factor of 2 of field observations (Gleicher et al., 2014) ($FAC2$), ratio of geometric means (MG), and geometric mean bias (VG) at three x/h locations and three source heights. Quantitative statistics representing the average value of the comparison to field data at all longitudinal locations $(x/h = 0.95, 1.9, 3.8)$ are included for an LES model (Pan et al., 2014) and a first order Lagrangian stochastic model (Gleicher et al., 2014).

z_{src}/h	statistic	$x/h = 0.95$	$x/h = 1.9$	$x/h = 3.8$	LES	LSM
1	*FAC2*	80%	80%	80%	93%	55%
	MG	1.52	1.43	1.17	1.02	1.87
	VG	1.79	1.27	1.20	1.17	2.05
2/3	*FAC2*	60%	80%	80%	70%	67%
	MG	2.07	1.56	1.09	0.70	1.13
	VG	19.5	2.18	1.37	1.42	1.80
1/3	*FAC2*	40%	80%	80%	66%	71%
	MG	2.78	1.51	1.09	1.09	1.02
	VG	153	2.50	1.39	2.18	1.45

$$MG = e^{\widetilde{\ln C_f} - \widetilde{\ln C_p}} \quad (20)$$

in which the tilde indicates the spatial average over all rotorod heights. Chang and Hanna (2004) suggest that a "good" model should have greater than 50% of model predictions within a factor of 2 of observations ($FAC2 > 50\%$), a geometric mean bias (VG) less than 1.6, and a ratio of geometric means within 30% ($0.7 < MG < 1.3$). The $FAC2$, VG, and MG values for each measurement location and release height are shown in Table 2. All statistics improved with x/h, approaching or exceeding the recommendation from Chang and Hanna (2004). The geometric mean bias, which reflected the ratio between C_f and C_p on a logarithmic scale, was unacceptably large for $x/h = 0.95, 1.9$, suggesting an initially lower dispersion of the RDM relative to the field measurements. By $x/h = 3.8$, all statistics were within the range of a "good" model (Chang and Hanna, 2004).

Recently, an LES model (Pan et al., 2014) and a first-order LSM with memory terms (Gleicher et al., 2014) were compared to the same field release of *Lycopodium* spores. The performance of all three models is compared in Table 2. At $x/h = 3.8$, the RDM performed similarly to the LES and better than the LSM. Note that the LES performance declined with source height (Table 2), and that the RDM performed better for $z_{src}/h = 2/3$ and 1/3. This is because the RDM included the contribution of plant-scale eddies in the lower canopy (see Eq. (12) and (13)). The LES model used a distributed drag to represent the canopy, which did not produce leaf-scale eddies and their contribution to mass flux in the lower canopy, such that the LES underestimated the diffusivity in the lower canopy. Consistent with this, below the penetration of canopy scale vortices $(z \le h - \delta_e)$, the far field eddy diffusivity (derived by dividing the LES local mean vertical flux by the vertical gradient in mean concentration) was 6 times smaller than the eddy diffusivity predicted by Eqs. (12) and (13), which was used in the RDM. Because the region below the penetration of canopy scale vortices comprises a significant fraction of dense canopies, it is important to correctly represent vertical transport in this region. The performance of the LES in the lower canopy might be improved by incorporating Eq. (13) to represent the contribution of unresolved, plant-scale eddies.

Because the RDM does not resolve individual sweeps and ejections, it can only model far field particle behavior, after particles have been in transport for more than 10 Lagrangian timescales ($\tau_l \cong 0.28 - 0.63$ s, based on velocity measurements of the Eulerian integral time scale made during the same maize field study, Chamecki, 2013). To explore at what point far field conditions began in the RDM, the transport time for airborne particles to reach several x locations was tracked. The far-field condition was reached at $x/h = 5$, at which point over 95% of the airborne particles had been in transport for more than 10 Lagrangian timescales. Because the

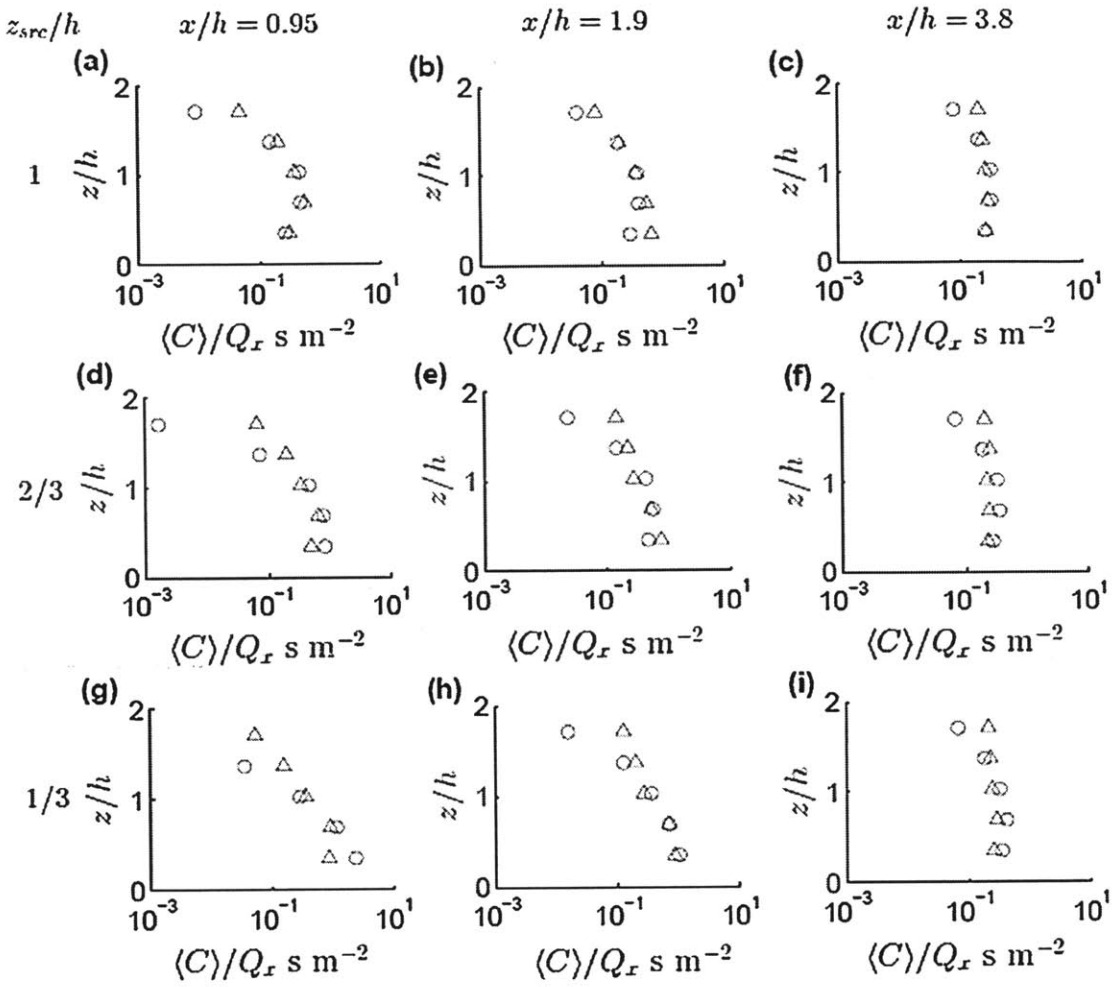

Fig. 3. Comparison of the concentration predicted by RDM (open circles) with measured concentration of *Lycopodium* spores released in a maize canopy (Gleicher et al., 2014), shown with open triangles. The laterally integrated concentration (C) is normalized by the equivalent source flux (Q_x), and vertical coordinate (z) is normalized by canopy height h. Spores were released at $z_{src}/h = 1/3$ (a, b, c), 2/3 (d, e, f), and 1 (g, h, i). The spores were collected at $x/h = 0.95$ (a,d,g), 1.9 (b,e,h), 3.8 (c,f,i).

maximum escape in the RDM occurred beyond this point, an eddy diffusivity-based approach should adequately represent *EF*. This, together with the agreement between the modeled and measured spore concentrations, built confidence in the RDM model, which was next used to evaluate trends in *EF* with particle size (w_s/u_*) and canopy density $(C_D a_f h)$.

3.2. Exploration of escape trends over w_s/u_*, $C_d a_f h$, h

RDM was used to explore how the velocity ratio (w_s/u_*), canopy density, and canopy height impacted escape fraction, an investigation of 1788 simulations (Figs. 4 and 5) that would have been computationally prohibitive using LES methods. First, RDM was used to explore how the velocity ratio impacted escape fraction (Fig. 4, model parameters given in Table 1). The solid horizontal line indicates the expected penetration of shear-layer turbulence from above the canopy, i.e. $z = h - \delta_e$. Consider particles with settling velocity comparable to the turbulent velocity $(w_s/u_* = 1)$. These particles only escaped if they originated in the exchange zone $(z_{src} > h - \delta_e)$, i.e. the region within which turbulent transport is enhanced by the canopy-scale vortices formed at the top of the canopy. Escape from the wake zone $(z_{src} < h - \delta_e)$ was unlikely (< 10%), because of the significantly lower K_z associated with the

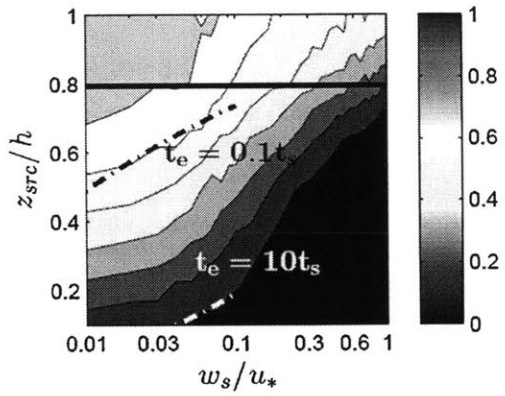

Fig. 4. Particle escape fraction (*EF*, values shown in color bar) from a maize canopy (*LAI* = 3.3) as a function of the source height, z_{src}, normalized by canopy height h, and particle settling velocity w_s, normalized by friction velocity u_*. The solid black horizontal line denotes the depth of turbulence penetration from above $(z = h - \delta_e)$. Lines comparing the time-scale of escape (t_e, Eq. (20)) and of settling (t_s, Eq. (21)) are also shown. The lines represent the locus in $(z_{src}/h, w_s/u_*)$ space for which $t_e = \gamma t_s$ with $\gamma = 0.1$ (black dashed line) or 10 (white dashed line). The solid black contour lines separating regions of different color represent successively the *EF* contours 0.1–1 in intervals of 0.1.

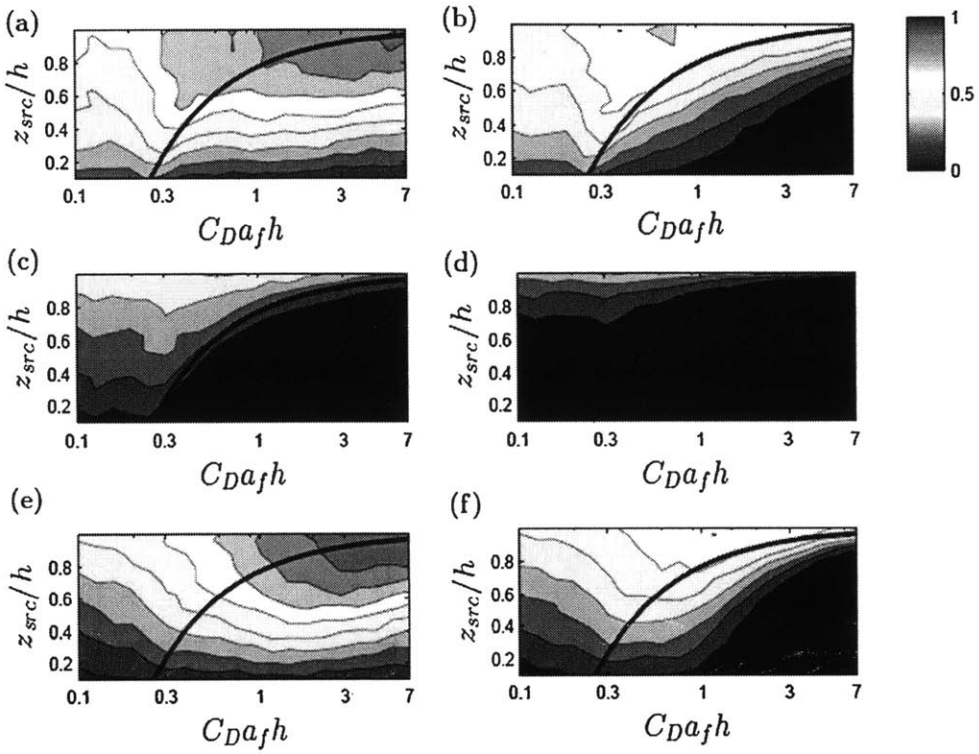

Fig. 5. Escape fraction (EF = 0–1, as shown in color bar) as a function of source height z_{src} normalized by canopy height h and non-dimensional canopy density $C_D a_f h$. The penetration of turbulence from above extends to $z = h - \delta_e$, denoted by the thick black line in each subplot. For (a) to (d), $h = 2.1$ m with varying a_f, and $w_s/u_* = 0$ (a), $w_s/u_* = 0.1$ (b), $w_s/u_* = 1$ (c), $w_s/u_* = 5$ (d). For (e) and (f), $a_f = 0.79$ m^{-1} with varying h, and $w_s/u_* = 0$ (e), $w_s/u_* = 0.1$ (f).

stem-scale vortices that dominate transport in this region (Eq. (12)). In contrast, particles with relatively small settling velocity $\left(w_s/u_* < 0.1\right)$ could be moved significant distances by the lower canopy turbulence, allowing escape even for particles originating deep within the canopy. For these light particles $\left(w_s/u_* < 0.1\right)$, canopy deposition was less important (impacting less than 20% of the particles, data not shown), so that the trends in escape fraction could be predicted by comparing the time scale for turbulent transport to the top of the canopy (t_e) and the time scale for settling to the ground (t_s):

$$t_e = \frac{(h - z_{src})^2}{K_z(z_{src})} \tag{21}$$

$$t_s = \frac{z_{src}}{w_s} \tag{22}$$

Fig. 4 depicts the locus in $\left(z_{src}/h, w_s/u_*\right)$ space for which $t_e = \gamma t_s$with $\gamma = 0.1$ (black dashed line) and 10 (white dashed line). Escape was rare (<10%) if $t_e/t_s >> 1$, corresponding to particles originating below the lower dashed line. Escape was common (>60%) if $t_e/t_s << 1$, corresponding to the region above the upper dashed line.

Next, RDM was used to examine escape fraction over a range of canopy densities (Fig. 5). Four values of velocity ratio were considered $\left(w_s/u_* = 0, 0.1, 1, 5\right)$. To explore the individual influences of a_f and h, Fig. 5a through 5d hold canopy height constant ($h = 2.1$ m) and vary $a_f = 0.07 - 4.9$ m^{-1}, but Fig. 5e and f hold the frontal area constant ($a_f = 0.79$ m^{-1}) and vary $h = 0.19 - 13$ m. As expected, the escape fraction decreased with decreasing source height $\left(z_{src}/h\right)$ in all cases. In addition, the escape fraction (EF) decreased as the settling velocity ratio $\left(w_s/u_*\right)$ increased, illustrated by the progression from $w_s/u_* = 0$ to 5 (Fig. 5a to 5d).

The trends with canopy density $\left(a_f h\right)$ were clearly influenced by the penetration length scale, δ_e. The lower limit of the exchange zone $\left(z = h - \delta_e\right)$is indicated in each subplot by a thick black curve. Particles were more likely to escape if they originated above $z = h - \delta_e$. This trend was most clear for $w_s/u_* = 0.1$ and 1 (Fig. 5b, c, f), for which the contours of escape fraction track the line denoting δ_e. A similar relationship would be expected for z_m, which is also a function of $C_D a_f h$, $z_m = \frac{1}{2}\delta_e$. For $w_s/u_* = 5$ (Fig. 5d), the pattern was less obvious, because escape fraction was so low over most of the canopy. In this case ($w_s/u_* = 5$), escape fraction was 0% over most of the canopy, but rose to as much as 40% for particles originating above $h - \delta_e$. Generally, for all particles with non-negligible settling velocity $\left(w_s/u_* = 0.1, 1, 5\right)$, as the depth of the region with elevated turbulence $\left(\delta_e\right)$ decreased $\left(C_D a_f h > 0.23\right)$, the canopy average escape fraction also decreased (circles in Fig. 6). For these particles, both settling to the ground and capture to the canopy were important mechanisms for detention within the canopy, with the region $z_{src}/h \geq 0.5$ dominated by deposition on the canopy, and the region $z_{src}/h \leq 0.5$ dominated by settling to the ground (data not shown).

Neutrally buoyant particles $\left(w_s/u_* = 0\right)$ exhibited different escape behavior (Fig. 5a, f), because these particles could only deposit to the ground or to the canopy via turbulent diffusion. For neutrally buoyant particles, the canopy average escape fraction increased with increasing canopy density (triangles in Fig. 6). This can be explained by the trends in deposition by turbulent diffusion. At low values of $C_D a_f h$, diffusivity was elevated across the full canopy height (Fig. 2), so that particles from any source height could reach the ground and deposit by diffusion. As $C_D a_f h$ increased, diffusivity within the canopy decreased (Fig. 2), with a coincident decrease in deposition to the ground, leaving more particles available to escape, so that canopy average escape increased.

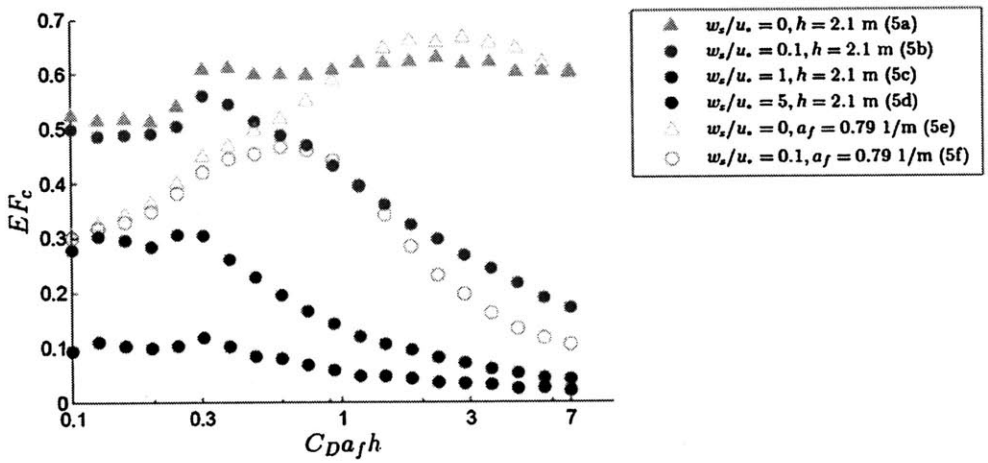

Fig. 6. Canopy average escape fraction (EF_c) for canopies shown in Fig. 5, as a function of the non-dimensional canopy density $C_D a_f h = 0.1 - 7$. Filled symbols denote canopies with $h = 2.1$ m and varying a_f; open symbols denote canopies with $a_f = 0.79\ \mathrm{m}^{-1}$ and varying h.

The trends in escape fraction were similar for constant h and constant a_f. For example, the difference in escape fraction (ΔEF) between each $\left(C_D a_f h, z_{src}/h\right)$ pair in Fig. 5a (constant h) and e (constant a_f) was $\Delta EF = 0.06 \pm 0.006$ (SE); between Fig. 5b (constant h) and f (constant a_f), the difference in escape fraction was $\Delta EF = 0.08 \pm 0.006$ (SE). This demonstrated that escape was more strongly dependent on the non-dimensional parameter $\left(C_D a_f h\right)$ than on the individual parameters of a_f and h. However, secondary influences from the individual contributions of a_f and h were apparent at low canopy density. Specifically, for $C_D a_f h \leq 0.5$, higher escape fractions were observed for the canopies with constant $h = 2.1$ m (Fig. 6, solid symbols) than for the canopies with constant $a_f = 0.79\ \mathrm{m}^{-1}$, for which $h = 0.19 - 0.93$ m over the range $C_D a_f h = 0.1 - 0.5$ (Fig. 6, open symbols). In other words, for the same value of $C_D a_f h$ higher escape fraction was observed for the taller canopy. This may be explained by the difference in the pseudo-velocity term $\left(\frac{dK_z}{dz}\right)$ in Eq. (2), which was larger for the taller canopies (data not shown). We caution, however, that this effect may arise from the oversimplified representation of the vertical profile of diffusivity. More detailed measurements of diffusivity profiles are needed to consider the real impact of the pseudo-velocity.

4. Conclusion

Forecasting infections from fungal disease can facilitate a reduction of fungicide application while maintaining crop yield (Aylor, 1999). This paper presented a practical tool for predicting spore escape fraction, a required input to forecast the long-range transport of spores. The proposed RDM predicted escape fraction from a simple set of parameters [canopy height, canopy density, spore settling velocity, vegetation length scale, and wind speed] and did not require detailed velocity or turbulence measurements as input. The model was validated against field measurements of spore concentration downwind from a source within a maize canopy, and it was shown to perform as well as, or better than, more complex LES and LSM models. Although the RDM did not explicitly represent individual turbulent events (sweeps and ejections), it can predict escape fraction, because maximum particle escape, which was used to define escape fraction, occurred in the far-field, that is after transport over several integral time scales. The RDM demonstrated that escape fraction increased as canopy density $\left(a_f h\right)$ decreased, as the settling velocity ratio $\left(w_s/u_*\right)$ decreased, and as the source height $\left(z_{src}/h\right)$ increased, confirming earlier studies (Aylor and Ferrandino, 1989; Aylor, 1990, 1999; Gleicher et al., 2014). The influence of the canopy density was largely reflected in the penetration length scale $\left(\delta_e\right)$, which segregated the canopy into regions of high and low escape probability. As a canopy matures, both canopy height and LAI increase, decreasing δ_e/h and creating a larger region within the lower canopy from which spore escape is inhibited.

Acknowledgements:

This material is based upon work supported by the National Science Foundation under Grant No. AGS-1005480. Any opinions, findings, or recommendations expressed in this material are those of the authors and do not necessarily reflect the views of the National Science Foundation

References

Andrade, D., Zaitao, P., Dannevik, W., Zidek, J., 2009. Modeling soybean rust spore escape from infected canopies: model description and preliminary results. J Appl. Meteorl. Climatol. 48, 789–803.
Aylor, D.E., Flesch, T.K., 2001. Estimating spore release rates using a Lagrangian stochastic simulation model. J. Appl. Meteorol. 40, 1196–1208.
Aylor, D.E., Irwin, M.E., 1999. Aerial dispersal of pests and pathogens: implications for integrated pest management. Agric. For. Meteorol. 97, 233–234.
Aylor, D.E., Taylor, G.S., 1983. Escape of *Peronospora tabacina* spores from a field of diseased tobacco plants. Phytopathol 73, 525–529.
Aylor, D.E., 1982. Modeling spore dispersal in a barley crop. Agric. Meteorol. 26, 215–219.
Aylor, D.E., 1986. A framework for examining the inter-regional aerial transport of fungal spores. Agric For Meteorol 38 263–288. Bound.-Layer Metorol. 46, 257–273.
Aylor, D.E., Ferrandino, F.J., 1989. Dispersion of spores released from an elevated line source within a wheat canopy. Bound.-Layer Metorol. 46, 251–273.
Aylor, D.E., 1990. The role of intermittent wind in the dispersal of fungal pathogens. Annu. Rev. Phytopathol. 28, 73–92.
Aylor, D.E., 1999. Biophysical scaling and the passive dispersal of fungus spores: relationship to integrated pest management strategies. Agric. For. Meteorol. 97, 275–292.
Aylor, D.E., 2005. Quantifying maize pollen movement in a maize canopy. Agric. For. Meteorol. 131, 247–256.
Boughton, B.A., Delaurentis, J.M., 1987. A stochastic model of particle dispersion in the atmosphMere. Bound.-Layer Meteorol. 40 (1), 147–163.
Chamecki, M., 2013. Persistence of velocity fluctuations in non-Gaussian turbulence within and above plant canopies. Phys. Fluids 25, 115110.
Chang, J.C., Hanna, S.R., 2004. Air quality model performance evaluation. Meterol. Atmos. Phys. 87, 167–196.
Denmead, O.T., Bradley, E.F., 1987. On scalar transport in plant canopies. Irrig. Sci. 8, 131–149.
Durbin, P.A., 1983. Stochastic differential equations and turbulent dispersion. NASA Reference Publ. 1103.
Elskus, A.A., 2014. Toxicity, sublethal effects, and potential modes of action of select fungicides on freshwater fish and invertebrates, U.S. Geological Survey Open-File Report 2012-1213, 42 p.

Finnigan, J.J., 2000. Turbulence in plant canopies. Annu. Rev. Fluid Mech. 32, 519–571.
Ghisalberti, M., Nepf, H., 2005. Mass transport in vegetated shear flows. Env. Fluid Mech. 5, 527–551.
Ghisalberti, M., Nepf, H., 2006. The structure of the shear layer in flows over rigid and flexible canopies. Env. Fluid Mech. 6, 277–301.
Ghisalberti, M., 2009. Obstructed shear flows: similarities across systems and scales. J. Fluid Mech. 641, 51–61.
Gleicher, S., Chamecki, M., Isard, S.A., Pan, Y., Katul, G.G., 2014. Interpreting three-dimensional spore concentration measurements and escape fraction in a crop canopy using a coupled Eulerian-Lagrangian stochastic model. Agric. Forest Meteorol. 194, 118–131.
Grimmond, C.S.B., Oke, T.R., 1999. Aerodynamic properties of urban areas derived from analysis of surface form. J. Appl. Meteorol. 38 (9), 1262–1292.
Hanna, S.R., 2003. Uncertainties in air quality model predictions. Bound. Layer Meteorol. 62, 3–20.
Harman, I.N., Finnigan, J.J., 2007. A simple unified theory for flow in the canopy and roughness sublayer. Bound.-Layer Meteorol. 123 (2), 339–363.
Hassid, S., 1983. Turbulent Schmidt number for diffusion models in the neutral boundary, boundary layer. Atmos. Environ. 17 (3), 523–527.
Isard, S.A., Russo, J.M., Ariatti, A., 2007. The integrated aerobiology modeling system applied to the spread of soybean rust into the Ohio River valley during September 2006. Aerobiologia 23, 271–282.
Israelsson, P.H., Kim, Y.D., Adams, E.E., 2006. A comparison of three Lagrangian approaches for extending near field mixing calculations. Environ. Model. Softw. 21, 1631–1649.
de Jong, M.D., Wagenmakers, P.S., Goudriaan, J., 1991. Modelling the escape of *Chondrostereum purpureum* spores from a larch forest with biological control of *Prunus-serotina*. Neth. J. Plant Pathol. 97, 55–61.
de Jong, M.D., 1992. Risk assessment for the application of biological control of a forest weed by a common plant pathogenic fungus. Risk Anal. 12, 465–466.
Koeltzsch, K., 2000. The height dependence of the turbulent Schmidt number within the boundary layer. Atmos. Environ. 34, 1147–1151.
Launder, B., 1976. Topics in applied physics. Heat and Mass Transport, vol. 12. Springer-Verlag, pp. 231–287 (Chapter 6).
Legg, B.J., Powell, F.A., 1979. Spore dispersal in a barley crop: a mathematical model. Agric. Meterorol. 20, 47–67.
Luhar, M., Rominger, J., Nepf, H., 2008. Interaction between flow, transport, and vegetation spatial structure. Environ. Fluid Mech. 8, 423–439.
Massman, W.J., Weil, J.C., 1999. An analytical one-dimensional second-order closure model of turbulence statistics and the Lagrangian time scale within and above plant canopies of arbitrary structure. Bound.-Layer Meteorol. 92, 81–107.
Nathan, R., Katul, G.G., 2005. Foliage shedding in deciduous forests lifts up long-distance seed dispersal by wind. Proc. Natl. Acad. Sci U.S.A. 102 (23), 8251–8256.
Nepf, H.M., Ghisalberti, M., White, B., Murphy, E., 2007. Retention time and dispersion associated with submerged aquatic canopies. Water Res. 43, W04422.
Nepf, H.M., 2012. Flow and transport in regions with aquatic vegetation. Annu. Rev. Fluid Mech. 2012 (44), 123–142.
Pan, Y., Chamecki, M., Isard, S.A., 2014. Large-eddy simulation of particle dispersion inside the canopy roughness sublayer. J. Fluid Mech. 753, 499–534.
Poggi, D., Porporato, A., Ridolfi, L., Albertson, J.D., Katul, G.G., 2004. The effect of vegetation density on canopy sub-layer turbulence. Bound.-Layer Meteorol. 111, 565–587.
Raupach, M.R., Finnigan, J.J., Brunet, Y., 1996. Coherent eddies and turbulence in vegetation canopies: the mixing-layer analogy. Bound.-Layer Meteorol. 78, 351–382.
Raupach, M., 1994. Simplified expressions for vegetation roughness length and zero-plane displacement as functions of canopy height and area index. Bound.-Layer Meteorol. 71, 211–216.
Roberts, J.R., Reigart, J.R., 2013. Recognition and Management of Pesticide Poisonings, 6th ed. United States Environmental Protection Agency, Office of Pesticide Programs, pp. pp. 272 http://www2epa.gov/pesticide-worker-safety/recognition-and-management-pesticide-poisonings.
Schlichting, H., 1936. Experimental investigation of the problem of surface roughness. Ingenieur-Archiv 7 (1), 1–34.
Shaw, R.H., Tavangar, J., Ward, D.P., 1983. Structure of the Reynolds stress in a canopy layer. J. Clim. Appl. Meteorol. 22, 1922–1931.
Silva, P.S.L., Silva, K.M.B., Silva, P.I.B., Oliveira, V.R., Ferreira, J.L.B., 2012. Green ear yield and grain yield of maize cultivars in competition with weeds. Planta Daninha 28 (1), 77–85.
Tanino, Y., Nepf, H.M., 2008. Lateral dispersion in random cylinder arrays at high Reynolds number. J. Fluid Mech. 600, 339–371.
Thom, A., 1971. Momentum absorption by vegetation. QJR Meteorol. Soc. 97, 414–428.
Thomas, C., Foken, T., 2007. Flux contribution of coherent structures and its implications for the exchange of energy and matter in a tall spruce canopy. Bound.-Layer Meteorol. 123, 317–337.
Wilson, J.D., Sawford, B.L., 1996. Review of Lagrangian stochastic models for trajectories in the turbulent atmosphere. Bound.-Layer Meteorol. 78, 191–210.
Wilson, J.D., Yee, E., 2007. A critical examination of the random displacement model of turbulent dispersion. Bound.-Layer Meteorol. 125, 399–416.
Wilson, J.D., Ward, D.P., Thurtell, G.W., Kidd, G.E., 1982. Statistics of atmospheric turbulence within and above a corn canopy. Bound.-Layer Meteorol. 24, 495–519.
Wilson, J.D., 2013. Turbulent Schmidt numbers above a wheat crop. Bound.-Layer Meteorol. 148, 255–268.

Chapter 6

Pollen dispersion as a function of canopy and particle characteristics

Abstract

Seagrass ecosystems are threatened worldwide, and continue to decline annually. The health and resilience of seagrass meadows has been shown to increase with intraspecies genetic diversity (Hughes and Stachowicz, 2004), which depends on successful transport of pollen particles between reproductive shoots. This chapter explores particle transport in seagrass canopies using a random walk model parameterized with profiles of mean velocity and eddy diffusivity constructed based on previous studies as functions of canopy area density, canopy height, canopy shear velocity, drag coefficient, and element length scale. The modeled concentration profiles agreed with experimental measurements (Ghisalberti and Nepf, 2005) in the far field. Modeled particle fate was also compared to a field release of monofilament particles in a seagrass canopy (Ackerman, 2002). The model and measured particles had similar trends for the release at the top of the canopy, but the model particles were captured lower in the canopy than observed in the field measurements, suggesting that the model had lower turbulent transport in the lower canopy, relative to the field measurements. Finally, particle capture by the canopy was explored for the velocity and water depth variation observed during a flooding tide (Grizzle et al., 1996). The distance over which half of the particles were retained on canopy elements decreased with decreasing mean longitudinal velocity, with a decrease observed due to the reduced vertical mixing for canopies with an observed *monami*. Future work should consider the release of pollen slightly above the canopy, with capture on a grid of reproductive shoots.

6.1. Introduction

Seagrass meadows act as a foundation species in coastal ecosystems, creating environmental conditions conducive to biodiversity (Bruno and Bertness, 2001). Dense seagrass meadows reduce bed shear stress (Sand-Jensen, 1998), stabilizing the sediment bed, and in some situations promoting carbon sequestration (Duarte et al. 2013a). Dense seagrass meadows mediate flow and provide shelter in coastal ecosystems, increasing biodiversity and sediment retention (Unsworth et al., 2010). A recent meta-analysis of meadow restoration found that only 37% of restoration efforts were successful, highlighting the importance of supporting existing meadows before collapse occurs (van Katwijk et al., 2016). Successful pollination of seagrass flowers is critical to the establishment of new meadows and the enhancement of meadow resilience (Hughes and Stachowicz, 2004). The submarine movement of seagrass pollen, vegetative fragments, and neutral or negatively buoyant seeds is highly dependent on the location of release within the canopy and canopy- and landscape-scale hydrodynamics, similar to the terrestrial dispersion of pollen and fungal spores (Kendrick et al., 2012). In this chapter, particle transport in a seagrass canopy is considered in the context of the canopy flow profile and canopy and particle physical parameters.

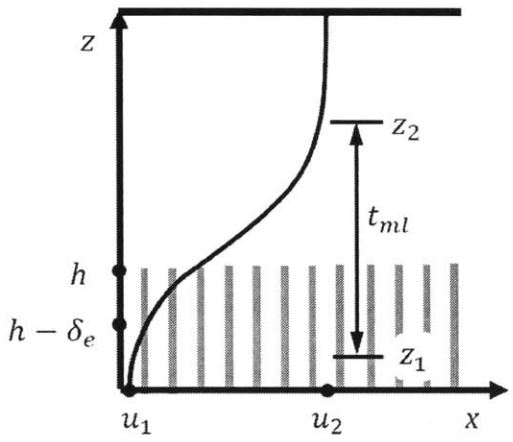

Figure 1 Schematic of mixing layer profile over a submerged canopy. The canopy height is h. The time-mean velocity is $\bar{u}$. The average low- and high-stream velocities are denoted u_1 and u_2, respectively. The mixing layer extends between z_1 and z_2 ($t_{ml} = z_2 - z_1$), with endpoints defined by $(\bar{u} - u_1)/\Delta u = 0.01$ and $(u_2 - \bar{u})/\Delta u = 0.01$ ($\Delta u = u_2 - u_1$).

The drag produced by seagrass blades attenuates flow within the canopy, creating a zone of low velocity close to the bed (Ackerman and Okubo, 1993, Ghisalberti and Nepf, 2002, Nepf et al., 2007, Nepf, 2012). The magnitude of flow diversion depends on the canopy frontal area density (a) and the canopy height (h). This study considered a 2D system, with coordinates (x, z) parallel and normal to the bed, respectively (Figure 1). The velocity vector $\vec{u} = (u, w)$ corresponded to the streamwise and vertical coordinates (x, z). The velocity was decomposed in to time-average and fluctuating components, respectively denoted by an overbar ($\bar{u}$) and prime (u'). When the canopy has sufficient density ($ah > 0.1$), the velocity profile resembles a mixing layer, with a hyperbolic tangent profile (Figure 1, Ghisalberti and Nepf, 2002). The blade density of seagrass canopies has been observed to occur within this dense regime ($ah = 0.4$-13, based on data provided in Chandler et al., 1996, McKone, 2009, Moore, 2004, Infantes, 2012). The mixing layer extends upward above the canopy, reaching endpoints at $z = z_1, z_2$. The

difference between the low-stream (u_1) and high-stream (u_2) velocities of the mixing layer is $\Delta u = u_2 - u_1$. The average distance of turbulence penetration, and the intensity of turbulent fluctuations is dependent upon the canopy density, $C_D ah$ (Nepf et al., 2007). As the canopy density increases, the canopy scale vortices are increasingly damped by the vegetative drag, reducing the extent of the mixing layer, (increasing z_1) and the thickness of the mixing layer (t_{ml}). In the upper canopy, the turbulence is dominated by the canopy-scale vortices, which form in the shear layer at the top of the canopy and have a velocity scale, $u_* = \sqrt{-\overline{u'w'}_h}$. However, these structures do not penetrate into the lower canopy, so that in the lower canopy the turbulence is dominated by stem-generated vortices.

In this chapter, the dispersion of tracer and negatively buoyant particles is explored using a random displacement model (RDM) parameterized with eddy diffusivities $K_z(z)$ and velocity profile, $u(z)$, based on canopy physical properties [canopy height, canopy density, vegetation length scale, and canopy shear velocity] (Follett et al., 2016). Experimental observations of velocity and turbulent diffusivity in a series of rigid and flexible submerged model canopies (Ghisalberti and Nepf, 2002, 2004, 2005, 2006) are used to describe the mean velocity and eddy diffusivity within a confined vegetated shear layer. The model is validated by comparison to a tracer study (Ghisalberti and Nepf, 2005). The modeled particle fate is also compared to field measurements of particle capture (Ackerman, 2002). Finally, the influence of increasing velocity and canopy reconfiguration on particle capture is evaluated over a flooding tide, using observations of canopy posture and velocity reported in Grizzle et al. (1996).

6.2. Methods

Individual particles originated at a specific source height within the meadow ($0 < z < h$) and were tracked until they deposited on the canopy, settled to the bed, or left the modeling domain. Particles that reached the water surface ($z = H$) were assumed to reflect off of the boundary, i.e. the water surface was a no-flux boundary. The size of the model domain (x, z) was $20h$ x H. In each constant time-step (Δt) the position of the particle (x_p, z_p) advanced longitudinally with the mean velocity $\bar{u}$ and vertically due to both settling (w_s) and turbulent transport (w'). The equations used to model the particle position were (Wilson and Sawford, 1996):

$$x_{p,i+1} = x_{p,i} + \bar{u}(z_{p,i})\Delta t \quad (1)$$

$$z_{p,i+1} = z_{p,i} + \left(\frac{dK_z(z_{p,i})}{dz} - w_s\right)\Delta t + R\sqrt{2K_z(z_{p,i})\Delta t} \quad (2)$$

The last term in (2) represents transport by turbulent velocity $w' = R\sqrt{2K_z}/\sqrt{\Delta t}$, and R a random number drawn from a normal distribution with mean 0 and standard deviation 1. The vertical transport also included a drift correction, or pseudovelocity, associated with the vertical variation in diffusivity (dK_z/dz). The pseudovelocity term prevented the artificial accumulation of particles in regions of low diffusivity (Durbin, 1983, Wilson and Yee, 2007). The formulations for the vertical profiles of time-mean streamwise velocity, $\bar{u}(z)$, and eddy diffusivity, $K_z(z)$ are described below in Section 3.1. The particle position was saved at every time-step. The model time-step, Δt, was constrained so that the vertical particle excursion within each time-step was much smaller than the scale of vertical gradients in the diffusivity and velocity (Israelsson et al.,

2006). Within the model canopy, both the velocity and diffusivity varied over length scales of approximately $0.1h$. Within each time-step, after a particle was moved, the position was assessed to determine if the particle had settled to the bed ($z_{p,i} = 0$); traveled beyond the model domain ($x_{p,i} > 20h$); or deposited to the canopy.

Canopy deposition was described as the probability of capture of one particle in one time-step, found from the probability that the particle is located in the plane of a blade, multiplied by the capture efficiency, or the fraction of particles in the plane of the blade that go on to deposit on the blade. The probability that the particle is in the projected area of a blade was equal to the blade width L_v divided by the average center to center spacing between blades (ΔS). In addition to being located within the plane of the blade, the particle needed to be located close enough to the blade so that it could impact the blade within one time-step, which was equal to the longitudinal particle excursion ($\Delta x_{p,i}$) divided by the average longitudinal spacing between blades (ΔS). The capture efficiency (η) was measured for particle impaction on rigid cylinders coated with Vaseline (Palmer et al., 2004). In order to estimate the impaction efficiency on straplike blades, we assume that the blade width can be substituted for the cylinder diameter:

$$\eta = 0.224 {Re_c}^{0.718} {R_p}^{2.08} \quad (3)$$

with the collector Reynolds number $Re_c = \bar{u}L_v/\nu$, with L_v=0.0055 m (McKone, 2009) the blade width and ν the kinematic viscosity of water. The particle ratio R_p is the ratio of the particle diameter to the blade width. The capture efficiency increases with increasing particle diameter. Multiplying the capture efficiency by the probability that the particle is in the plane of the blade

120 and close enough to contact the blade in one time-step, the probability of particle impaction on
121 vertical surfaces in one time-step is:

122 $$dp_x = \eta \frac{L_v}{\Delta S^2} \Delta x_{p,i} = \eta a_x \Delta x_{p,i} \quad (4)$$

123 with (a_x) the component of the one-sided blade area projected in the x direction. Similarly, the
124 probability of particle impaction on horizontal surfaces is $dp_z = \min(0, \eta a_z \Delta z_{p,i})$, with the
125 impact of gravitational settling and turbulent transport included in the vertical particle
126 excursion (eq. 2). In order to find the component of the blade area projected in the x and z
127 directions, the curved blade posture was broken up into linear segments, such that the blade
128 position was converted to a series of vectors. The projected area in the x direction, $P_x(z)$, was
129 found by multiplying the magnitude of the vector segment by the cosine of the angle ($\cos\theta$)
130 between the blade position ($k(z)$) and the vertical vector (j), found by dividing the dot product
131 of j and $k(z)$ by the magnitudes of both vectors ($\cos\theta(z) = \frac{j \cdot k(z)}{|j||k(z)|}$, Figure 2). Similarly, the
132 projected area in the z direction, $P_z(z)$, was found by multiplying the magnitude of the vector
133 segment by the sine of the angle ($\sin(\theta)$) between the blade position and the vertical vector.
134 The component of the blade area projected in the x and z directions was found by multiplying
135 the one-sided blade area (a) by $P_x(z)$ and $P_z(z)$, respectively. The blade posture could be found
136 from observation (e.g. Grizzle et al., 1996) or calculated from the blade physical properties and
137 mean current speed (e.g. Luhar and Nepf, 2011). The total probability of particle deposition
138 was the sum of the probability of particle impaction on vertical and horizontal surfaces
139 $(dp = dp_x + dp_z)$. To determine if the particle deposited during the time-step, a random

number, R_c, was chosen from a uniform distribution between 0 and 1. If R_c was less than or equal to the probability of deposition, the particle deposited to the canopy.

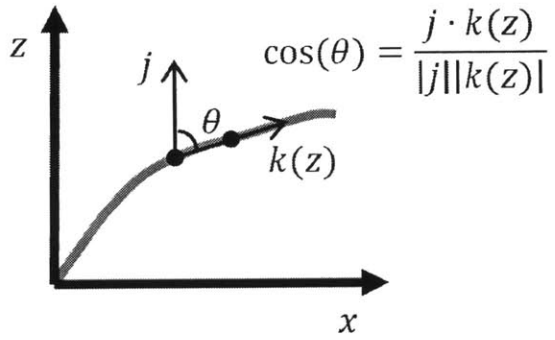

Figure 2 Diagram of blade posture and determination of projected area in the x direction. The the cosine of the angle between the blade position ($k(z)$) and the vertical vectors (j) was found by dividing the dot product of j and $k(z)$ by the magnitudes of both vectors.

(a) u profile:

$u = \frac{1}{2}\Delta u * tanh(\frac{z-h+(h-z_1)/4.73}{(h-z_1)/1.2}) + \frac{1}{2}(u_1 + u_2)$

rigid canopies:

$\Delta u = \frac{u_*}{0.14}$, $\frac{z_1}{h} = 0.39 - \frac{0.078}{C_D a h}$, $\frac{u_1}{u_h} = 0.38(C_D a h)^{-0.26}$, $\frac{\Delta u}{u_h} = 6.8(ad)^{0.42}$

flexible canopies:

$\Delta u = \frac{u_*}{0.11}$, $\frac{z_1}{h} = 0.63 - \frac{0.29}{C_D a h}$, $\frac{u_1}{u_h} = 0.21(C_D a h)^{-0.45}$, $\frac{\Delta u}{u_h} = 6.8(ad)^{0.42}$

using these relations, $u = f(u_*, h, C_D, a, b)$

(b) K_z profile:

$K_z = (0.17 \pm 0.08)ub, \qquad z/h < z_1/h$

$K_h = 0.096\Delta u(h - z_1), \qquad z/h = 1$

$K_z = 0.039\Delta u(h - z_1), \qquad z/h > z_2/h$

using these relations, $K_z = f(u_*, h, C_D, a, b)$

(c) canopy parameters:

study	u_* (cm/s)	Δu (cm/s)	h (m)	C_D	a (m^{-1})	b (mm)	H (m)
GN05 A	.45	3.2	0.139	.81	2.5	6.4	.467
GN05 C	.74	4.9	0.139	.77	3.4	6.4	.467
GN05 D	.53	3.5	0.139	.85	3.4	6.4	.467
GN05 E	1.33	9.5	0.139	.67	4.0	6.4	.467
GN05 F	.84	6.0	0.139	.71	4.0	6.4	.467
GN05 G	.50	3.3	0.139	.82	4.0	6.4	.467
GN05 H	1.57	11.2	0.139	.61	8.0	6.4	.467
GN05 I	.96	7.4	0.139	.66	8.0	6.4	.467
A02	0.5	-	1	1	0.91	5.0	5.5
G96 2.8	-	4.75	1.25	1	4	5.5	1.6
G96 6.4	-	10.64	1.3	1	4	5.5	2.2
G96 6.5	-	13.94	1.04	1	4	5.5	2.5
G96 6.9	-	12.41	1.78	1	4	5.5	3

146

147 **Table 1** Equations describing the curves of (a) mean longitudinal velocity and (b) eddy
148 diffusivity, which require the canopy shear velocity, canopy height, drag coefficient, frontal

149 area, and blade width. Physical parameters (c) of the canopies considered in this chapter
150 (Ghisalberti and Nepf, 2005, Ackerman, 2002, Grizzle et al. 1996) are presented.

151 **2.1. Velocity and Eddy Diffusivity Profiles to Parameterize RDM**

152 Several previous studies were combined to describe $\bar{u}(z)$ and $K_z(z)$ as functions of u_*, a, h,
153 L_v, and C_D. Profiles were only constructed for dense canopies ($ah \gtrsim 0.1$), representative of
154 observed seagrass canopies (Chandler et al., 1996, Moore, 2004, McKone, 2009, Infantes et al.,
155 2012, $ah = 0.4$-13). The velocity profile within and above the canopy resembles a mixing layer,
156 with a hyperbolic tangent profile centered $0.5t_{ml}/7.1$ above the top of the canopy (Ghisalberti
157 and Nepf, 2002):

158 $$\bar{u} = 0.5\Delta u * \tanh\left(\frac{z-(h+0.5t_{ml}/7.1)}{2t_{ml}/7.1}\right) + 0.5(u_1 + u_2) \quad (5)$$

159 The mixing layer profile was related to canopy physical parameters using a series of flow
160 measurements over 9 rigid and 6 flexible canopies, with varying area density and flow velocity
161 (Ghisalberti and Nepf 2002, 2004, 2005, 2006). The difference between the low- and high-
162 stream velocities (Δu) was correlated with the magnitude of velocity shear at the top of the
163 canopy, characterized by the canopy shear velocity. Specifically, $\Delta u = \frac{u_*}{0.14}$ for rigid canopies
164 (Ghisalberti and Nepf, 2005), and $\Delta u = \frac{u_*}{0.11}$ for flexible canopies (based on data presented in
165 Table 1, Ghisalberti and Nepf, 2006). The relative height of the lower endpoint of the mixing
166 layer, z_1/h, increased with canopy density, with z_1/h dependent on $C_D ah$. Specifically,
167 $\frac{z_1}{h} = 0.39 - \frac{0.078}{C_D ah}$ for rigid canopies, and $\frac{z_1}{h} = 0.63 - \frac{0.29}{C_D ah}$ for flexible canopies, based on data
168 presented in Table 1, Ghisalberti and Nepf, 2006). The ratio of the low-stream velocity to the
169 velocity at $z = h$ decreased with canopy area density ($\frac{u_1}{u_h} = 0.38(C_D ah)^{-0.26}$, rigid canopies;

170 $\frac{u_1}{u_h} = 0.21(C_D ah)^{-0.45}$, flexible canopies, Ghisalberti and Nepf, 2006). The normalized shear
171 $(\Delta u/u_h)$ increased with the dimensionless plant density ($\frac{\Delta u}{u_h} = 6.8(ad)^{0.42}$, Ghisalberti and
172 Nepf, 2004). While a proportional relationship to $C_d ad$ was expected, Ghisalberti and Nepf
173 (2004) found that the experimental date depended only on ad. Because only $C_D a$ was
174 measured over flexible canopies, a separate relation could not be obtained from the flexible
175 data set, so the relation from the rigid dataset was used.

176 Within the canopy the profiles are divided into two regions. In the lower canopy ($z <$
177 z_1), the eddy diffusivity scales on the size of the vegetation elements ($K_z = (0.17 \pm 0.08) u L_v$,
178 $uL_v/\nu > 100$, Lightbody and Nepf, 2006).. Within the mixing layer ($h \geq z \geq z_1$), canopy-scale
179 vortices elevate K_z. The eddy diffusivity peaks at $z = h$ and scales on the mixing layer thickness
180 and Δu ($K_h = 0.032 \Delta u t_{ml}$, Ghisalberti and Nepf, 2005). Above the mixing layer ($z > z_2$), the
181 eddy diffusivity has a constant value ($K_z = 0.013 \Delta u t_{ml}$, Ghisalberti and Nepf, 2005). The eddy
182 diffusivity was assumed to follow a linear function between the regions of constant diffusivity
183 ($z < z_1, z > z_2$) and $z = h$.

184 The family of curves for mean longitudinal velocity and eddy diffusivity across a range of
185 canopy density is shown for the eight experimental cases in which an eddy diffusivity was
186 measured (Figure 2, Ghisalberti and Nepf, 2005). Because the endpoints of the mixing layer, the
187 low-stream velocity, the mixing layer thickness, the eddy diffusivity at $z = h$, and the high-
188 stream eddy diffusivity were chosen to fit the dataset, this comparison is not a validation of the
189 model. On average, the measurements were a factor of 0.9 of the constructed $\bar{u}$ and K_z
190 profiles.

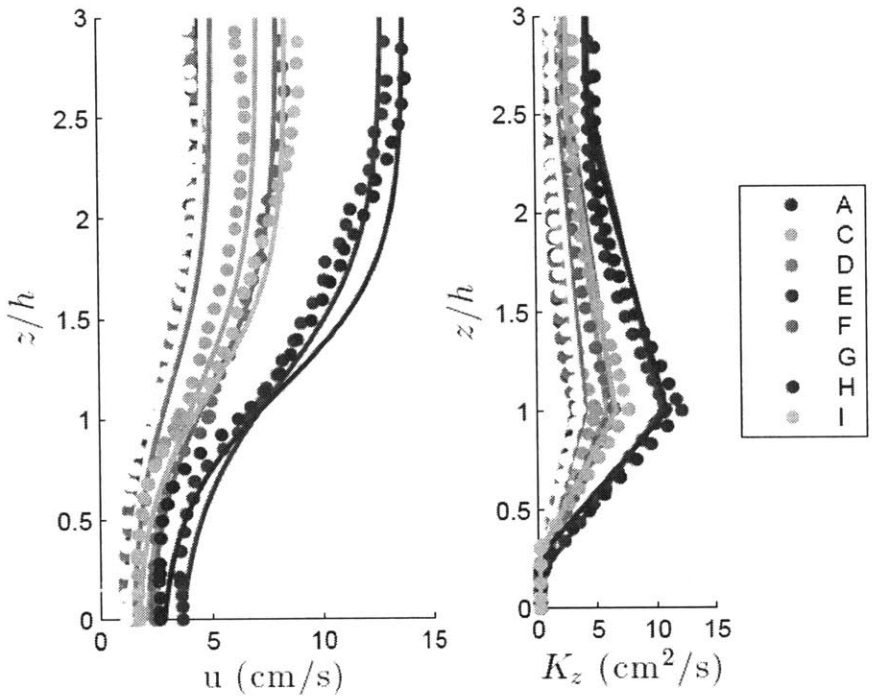

191

192 **Figure 2** Family of curves of the mean longitudinal velocity and eddy diffusivity for a series of
193 experiments over a submerged rigid canopy (Ghisalberti and Nepf, 2005). The open circles
194 represent measured values over the model canopy. The constructed profiles are shown by solid
195 lines. In alphabetical order, the canopy height $h = 13.9$ cm, $L_v = 0.64$ cm, $u_* =$
196 0.45,0.74,0.53,1.33,0.84,0.50,1.57,0.86,0.55 cm/s, $C_D = 0.81$,0.77, 0.85, 0.67, 0.71, 0.82, 0.61,
197 0.66, 0.79, and $a = 0.025$, 0.034, 0.034, 0.040, 0.040, 0.040, 0.080, 0.080, 0.080 cm^{-1}. Because
198 the endpoints of the mixing layer, the low-stream velocity, the mixing layer thickness, the eddy
199 diffusivity at $z = h$, and the high-stream eddy diffusivity were extracted from the experimental
200 data, this comparison is not a validation of the model.

201

202 **6.3. Results**

203 First, the RDM results were compared to profiles of dye concentration (case I in Ghisalberti and
204 Nepf, 2004) released at $z/h = 1$ and measured at six longitudinal locations over a rigid canopy
205 ($x/h = 1.4$, 3.9, 6.6, 10.8, 18.0, 27.3). In order to represent a neutrally buoyant tracer, the RDM
206 particles had neutral buoyancy, the retention on canopy elements was omitted, and the bed
207 was treated as a no-flux boundary. In order to calculated concentration and waterborne flux in

208 the RDM, a vertical column of interrogation boxes (0.02 m long x 0.01 m high) was defined,
209 centered at the field data collection points (Ackerman, 2002). Particles were continuously
210 released until a steady-state particle concentration was established in each box. The particle
211 concentration was found by dividing the steady-state number of waterborne particles in each
212 box by the box area. The waterborne flux was found by integrating the flux at each box over the
213 water depth, $Q_x = \int \bar{u}(z)C(z)dz$. In the near field, the model exhibited higher dispersion than
214 the measured concentration (Figure 3). Initially, the dye plume could be spread only by vortices
215 at the plume scale, which was smaller than the canopy scale vortices, so that the canopy-scale
216 vortices did not immediately aid dispersion (Ghisalberti and Nepf, 2004). The RDM represented
217 vertical movement using an average eddy diffusivity, so that the dispersion of the model
218 particles immediately reflected the influence of the larger turbulence scales. The model and
219 measured data were in agreement by the far field ($x/h \geq 8.9$, Ghisalberti and Nepf, 2005); past
220 this point, the average ratio of measured and modeled observations was 93%.

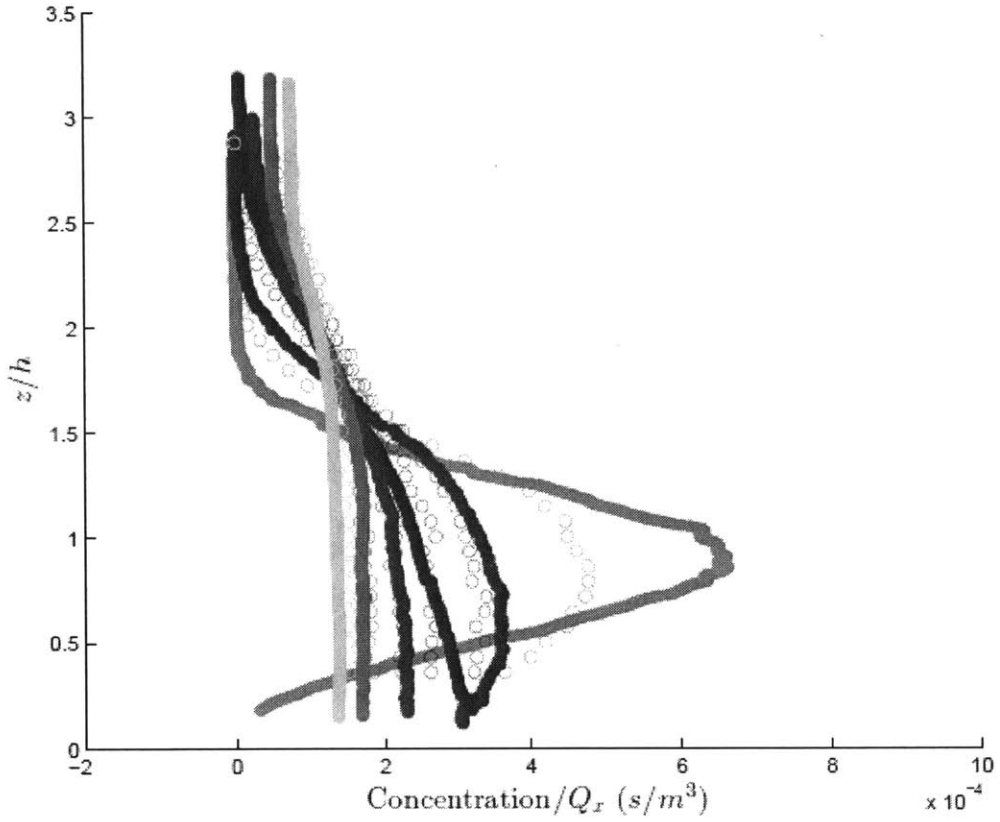

Figure 3 Comparison of concentration normalized by total flux for RDM particles (open dots) and dye concentration (solid dots, case I, Ghisalberti and Nepf, 2005) at six longitudinal locations (x/h = 1.4, 3.9, 6.6, 10.8, 18.0, 27.3). The concentration (g/m^2) was normalized by the longitudinal flux, $Q_x = \int \bar{u}(z)C(z)dz$ (g/s).

The RDM was next compared to field releases of spherical and filamentous particles cut from fishing line ($\rho \approx 1.17e3$, Ackerman, 2002). The particles were released within a *Zostera marina* canopy (Woods Hole, MA) and captured on an array of plexiglass plates (5 x 120 x 0.5 cm) greased with petroleum jelly. Ackerman (2002) captured only 0.2% of the released particles. Despite the low overall rate of capture, the relative distribution of capture within the canopy should remain valid, forming a reasonable basis to test the RDM. The settling velocity of spherical particles was 2 mm/s, with particle diameter 0.2 mm (Ackerman, 2002). The settling

velocity of filamentous particles was 4.7 mm/s, with longest dimension 4 mm. The canopy height was 100 ± 3 cm, with water depth H approximately 5 m. The shoot density was 91 ± 7 shoots/m^2. The frontal area was estimated to be 0.91 m^{-1}, based on shoot density and one-sided leaf area index measurements of the same *Zostera marina* canopy five years earlier (200 shoots/m^2, $a = 2$ m^{-1}, $h = 1$ m, Dennison and Alberte, 1982). We assumed that the shoot density was proportional to a. The blade width was assumed to be 5 mm (McKone, 2009). The canopy shear velocity ($u_* = 0.5$ cm/s) was estimated from laboratory measurements of u_*/u_h for which the model canopy was approximately erect, similar to the field conditions (Ackerman, 2002). Because the Ackerman canopy was described as "more or less erect," the blade posture was assumed to be similar to case (b) in Grizzle et al. (1996) (Figure 6 in this chapter).

The drag coefficient was assumed to equal 1, based on measurements that C_D is of order 1 for rigid vegetation and flow past a flat plate (Vogel 1984, Ghisalberti and Nepf, 2006, Luhar and Nepf, 2011). The constructed and measured profiles (Ackerman, 2002) of mean velocity are shown in Figure 4. The model profile was within 1.22 cm/s of the measurements (a factor of 2.47).

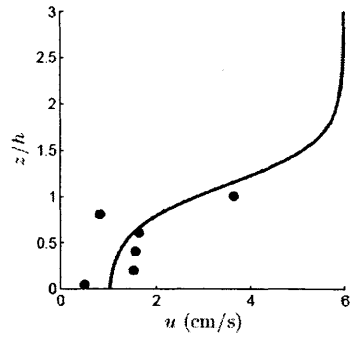

Figure 4 Comparison of measured (solid black dots, Ackerman, 2002) and model (black line) mean longitudinal velocity within a *Zostera marina* canopy ($h = 1$ m, $a = 0.91$ m^{-1}, $u_* = 0.5$ cm/s, $C_D = 1$, $L_v = 5$ mm).

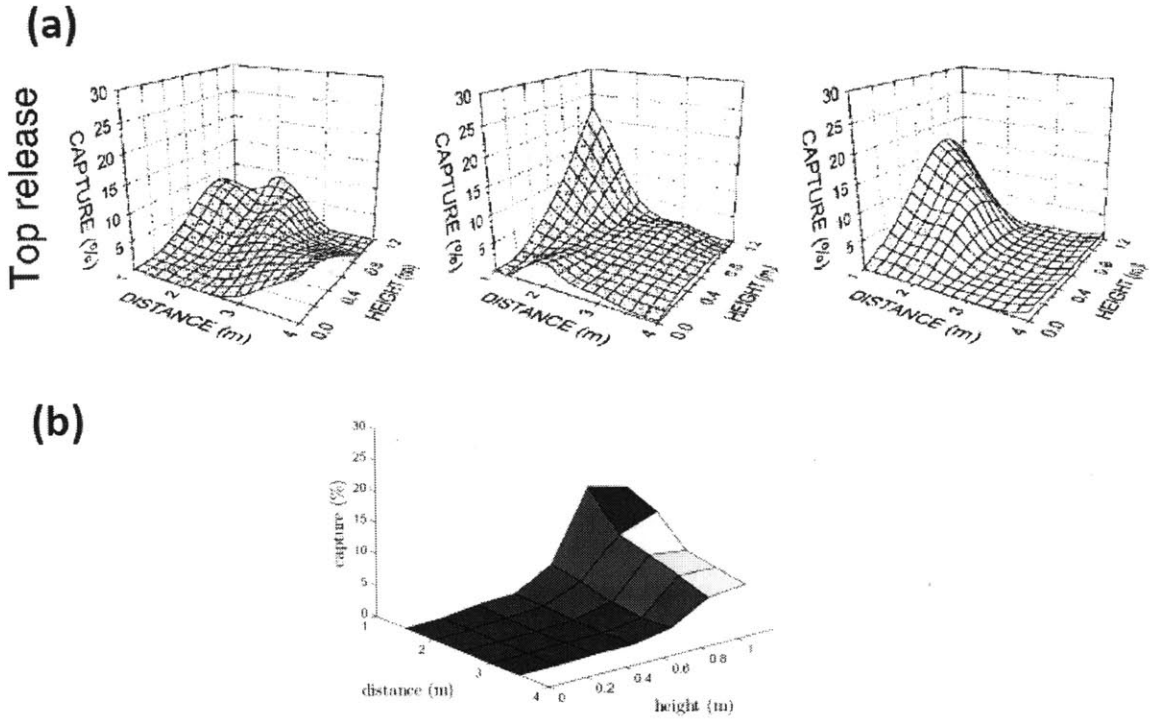

Figure 5 Percent of releases of three repeat experimental (a, published as part of figure 4 in Ackerman, 2002) and modeled (b) filamentous particles captured between $x = 1 - 4$ m and $z = 0$—1.2 m from particles released at z/h =1. The capture at discrete (x, z) points was interpolated using a nearest neighbor method; the color of each square represents the average capture percentage in each square (0-14.8%), with red and orange denoting higher capture percentages.

In the field experiments, particles were released at two heights and captured on a grid of poles (x = 1.5,2,2.5,3,3.5 m, y = -.5,-.25,0,.25,.5 m). The capture trends were laterally averaged, and the percent of all captured particles present at an (x, z) location was presented (Ackerman 2002, Figure 4 in that paper). Because only the laterally averaged trends were available for comparison, a 2D model is appropriate for assessing the general particle transport trends. The RDM recorded the vertical position of each particle passing a longitudinal pole

268 location, resulting in a distribution of vertical positions for particles passing each pole. A
269 histogram of particle locations was created, with box centers (z = 0.1,0.3,0.5,0.7,0.9,1.1 m and
270 box width 0.2 m. The trends of capture in x and z, reported as the percent of all captured
271 particles measured at each (x, z) pair, is shown for the experimental and RDM filamentous
272 particles released at $z = h$ in Figure 5. Three repeat experimental releases were conducted on
273 August 10, 1986, July 31, 1987, and August 2, 1987. The experimental releases showed
274 significant variation, but the general capture trends were similar for both the modeled and
275 measured filamentous particles at the higher release point. The modeled particle transport
276 varied from the experimental results for filamentous particles released inside the canopy ($0.6h$)
277 and spherical particles (data averaged over both release heights, Ackerman, 2002). Modeled
278 filamentous particles released within the canopy ($0.6h$) had significant canopy capture, so that
279 the 1.4% of particles that were still waterborne within $x = 1 - 4$ m were located in the lower
280 canopy, for which the capture efficiency was lowered due to the reduced velocities in this
281 region. In contrast, modeled spherical particles had very low probability of canopy capture, so
282 that the particle distribution was more uniform than the Ackerman data, resulting in a lower
283 capture probability for any point (RDM capture percentage 0-4.4%, Ackerman 2002 0-30%). The
284 discrepancy may be due to the particle ratio R_p, which had a second-order influence on the
285 particle capture efficiency.

286 Finally, the particle retention trends were explored for a large (400 hectare) seagrass
287 meadow described by Grizzle et al. (1996), for which mean longitudinal velocity profiles were
288 measured during a flooding tide (t =1.1, 2.1, 2.8, 3.2 h after low slack tide). A velocity profile

and drawing of the canopy was reported for each time point (Figure 6, h =1.25, 1.31, 1.04, 1.78 m, H =1.6, 2.15, 2.52, 3 m).

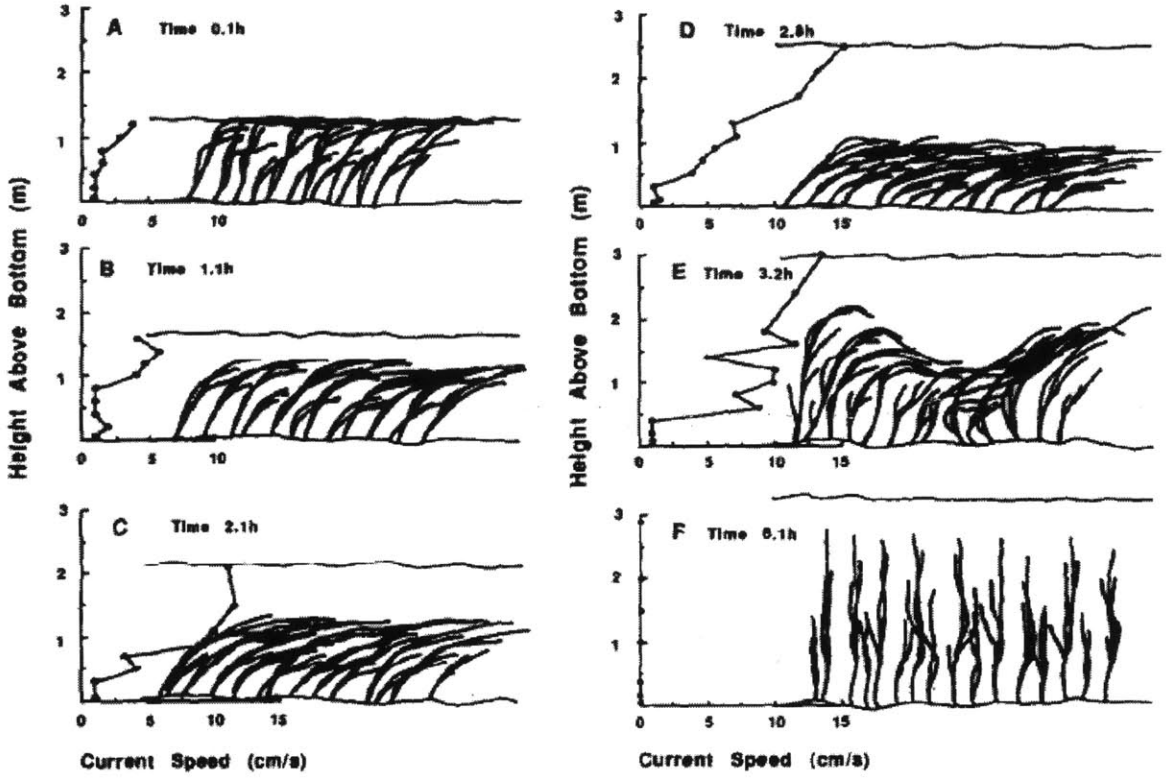

Figure 6 Velocity profiles with drawings of eelgrass blade responses, based on underwater visual observation on July 25, 1989 (Grizzle et al. 1996, Figure 1 in that paper). A-F show measurements made at different times during a flooding tide, beginning at 0.1 h after low slack tide (A) and continuing until high slack tide (F).

A *monami* was observed for the final time point (t = 3.2 h, maximum flood current). The presence of the *monami* reduces the turbulent stress at the top of the canopy by approximately one half relative to a rigid canopy (Ghisalberti and Nepf, 2006), suggesting that the coherent structures are weakened in the presence of the *monami*. The eddy diffusivity at $z = h$ was reduced by one half in the RDM for cases in which a *monami* was present. The leaf area density was not known, but was estimated to equal $a = 6\ \mathrm{m}^{-1}$, based on the shallow

submergence site in Dennison and Alberte (1982) for which $H/h = 2.6$. The drag coefficient was assumed to equal 1, and the blade width was assumed to equal 5 mm (McKone, 2009). The constructed and measured velocity profiles for each time point are shown in Figure 6. Over all measurement points, the model and measured points agreed within a factor of 3.8. On average, the model and measured profiles agreed within a factor of 1.4.

The retention trends were explored by releasing particles with settling velocity ($w_s = 3.5$ μm/s) and length ($l = 4$ mm) similar to *Z. marina* pollen (Ackerman, 2002) at 9 vertical positions within the canopy ($z/h = 0.1—1$, Figure 7). The timescale of the flooding tide ($6h$) was much longer than the timescale for particle capture (<5 minutes), suggesting that the flow was quasi steady during the capture process. For the cases in which the *monami* was not present, the distance over which half of the particles were retained by the canopy decreased with increasing velocity, reflecting the increase in capture efficiency ($\eta \sim u^{0.718}$). The particles representing conditions at the maximum flood current, $\bar{u} = 0.14$ m/s, for which a *monami* was observed, had the shortest median capture distance, reflecting the decrease in vertical mixing due to the *monami*. Conceptually, if the median capture distance is less than the meadow length (L), most particles would be captured by the meadow, while if $x_{1/2} > L$, most particles would be exported from the meadow. *Z. marina* releases pollen from reproductive shoots located within 0.3-1.05h, with reproductive shoots slightly taller than the canopy height (h_{shoot}/h =1.05, Ackerman, 2002), with successful capture on female flowers located on similar shoots (de Cock, 1980). In order to investigate the influence of canopy hydrodynamics on seagrass pollination, future work should consider the capture on a series of reproductive shoots.

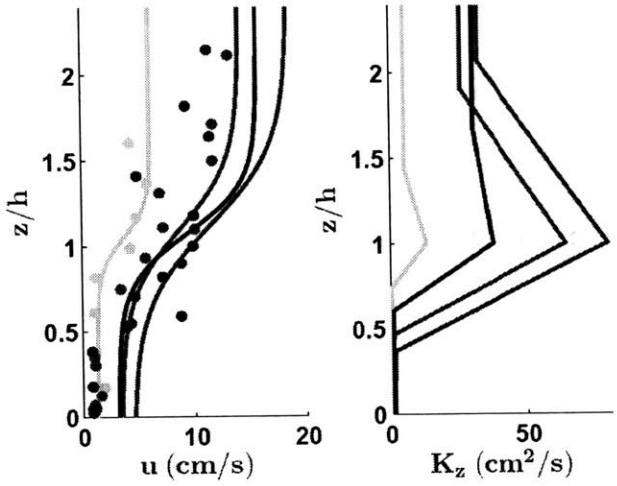

Figure7 Profiles of mean longitudinal velocity and eddy diffusivity at four time points during a flooding tide (light-dark blue, t = 1.1, 2.1, 2.8, 3.2 h after low slack tide). The measured points are represented by solid dots (Grizzle et al., 1996). The model points are represented by solid lines. For each of the four time points, respectively, h = 1.25, 1.31, 1.04, 1.78 m, H = 1.6, 2.15, 2.52, 3 m, Δu = 4.8,10.6,13.9,12.4 cm/s. C_D was assumed to be 1, a = 4 m^{-1}, and L_v = 4 mm.

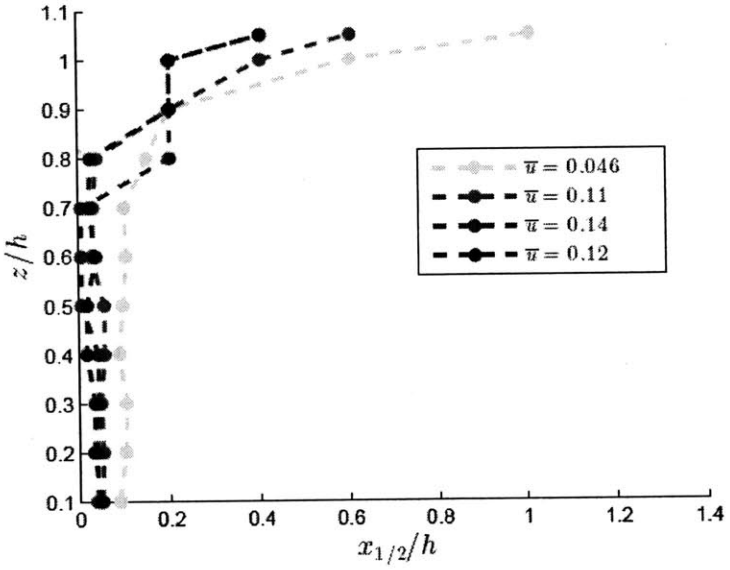

Figure 8 Distance over which half of particles released at z/h = 0.1—1.05 were retained by the canopy, at four time points during a flooding tide (light-dark blue, $\bar{u}$ = 0.046, 0.11, 0.14, 0.12 m/s).

335 **6.4. Conclusion**

336 Intraspecies genetic diversity, which relies on successful pollination of seagrass flowers,
337 is critical to the establishment of new meadows and enhancement of meadow resilience
338 (Hughes and Stachowicz, 2004, Hughes et al., 2008). Successful pollination depends on the
339 transport of pollen between male and female flowers of separate seagrass clones, a process
340 which takes place within the canopy mediated flow. In order to produce a viable seed, pollen
341 must be transported outside the area dominated by its parent clone and be captured by a
342 mature flower of a separate genetic individual. Pollen that is captured on reproductive
343 structures of its parent plant (small $x_{1/2}$) or nonreproductive blades will fail to produce seeds,
344 while pollen that escapes the canopy and is transported downstream (large $x_{1/2}$) may have a
345 lower likelihood of successful pollination, because it must first contact another seagrass canopy
346 before pollination is possible. Because hydrodynamic transport is a crucial link in this process,
347 pollination depends on the canopy physical parameters that influence the canopy flow profile,
348 such as the canopy frontal area density, canopy height, and submergence depth.

349 This chapter used an RDM to explore trends in particle fate and transport over
350 submerged model meadows representative of *Z. marina*. The RDM correctly predicts far field
351 measurements of dye concentration (Ghisalberti and Nepf, 2004). The capture of RDM
352 particles was also compared to a field release of polyethylene particles in a *Zostera marina*
353 canopy (Ackerman, 2002). Similar to the field results, the RDM capture declined with
354 longitudinal and vertical distance from the source for the release of particles with $d_p = 4$ mm
355 at $z/h = 1$. However, the RDM particles were captured more efficiently than field
356 measurements for the release at $z/h = 0.6$. Smaller particles ($d_p = 0.2$ mm) were captured

357 less efficiently than field measurements, resulting in a more uniform distribution than was
358 measured (Ackerman, 2002). Finally, capture trends were explored for 400 hectare seagrass
359 meadow during different periods within a tidal cycle (Grizzle et al., 1996). The distance over
360 which half of the released particles were retained by the canopy generally decreased with
361 depth-averaged velocity, and was further reduced in the presence of a *monami*, because
362 vertical mixing was reduced by one half compared to the cases without a *monami*.
363
364
365
366
367
368
369
370
371
372
373
374

375 **References**

376 Ackerman, J.D., 2002. Diffusivity in a marine macrophyte canopy: implications for submarine
377 pollination and dispersal. American Journal of Botany 89(7), 1119-1127.

378 Ackerman, J.D., Okubo, A., 1993. Reduced mixing in a marine macrophyte canopy. Funct Ecol 7:
379 305-309.

380 Aylor, D.E., Flesch, T.K., 2001. Estimating spore release rates using a Lagrangian stochastic
381 simulation model. J Appl Meteorol 40, 1196-1208.

382 Bruno, J.F., Bertness, M.D., 2001. Positive interactions, facilitations, and foundation species.
383 Sunderland: Sinauer Associates, pp. 201-218.

384 Chandler, M., Colarusso, P. and Buchsbaum, R. (1996) A study of eelgrass beds in Boston Harbor
385 and northern Massachusetts bays, Office of Research and Development, U.S. Environmental
386 Protection Agency, Narragansett, RI.

387 de Cock, A.W.A.M., 1980. Flowering, pollination, and fruiting in *Zostera marina* L. Aquatic
388 Botany 9, 201-220.

389 Dennison, W.C., Alberte, R.S., 1982. Photosynthetic responses of Zostera marina L. (eelgrass) to
390 in situ manipulations of light intensity. Oecologia 55 (2), 137-144.

391 Duarte, C.M., Losada, I.J., Hendriks, I.E., Mazarrasa, I., Marbà, M., 2013a. The role of coastal
392 plant communities for climate change mitigation and adaptation. Nature Climate Change 3,
393 961-968.

394 Durbin, P.A., 1983. Stochastic differential equations and turbulent dispersion. NASA Reference
395 Publication 1103.

396 Follett, E., Chamecki, M., Nepf, H., 2016. Evaluation of a random displacement model for
397 predicting particle escape from canopies using a simple eddy diffusivity model. Agricultural and
398 Forest Meteorology 224, 40-48.

399 Ghisalberi, M., Nepf, H., 2002. Mixing layers and coherent structures in vegetated aquatic flows.
400 Journal of Geophysical Research 107 (C2), 3011.

401 Ghisalberti, M., Nepf, H.M., 2004. The limited growth of vegetated shear layers. Water Res. Res.
402 40, W07502, doi: 10.1029/2003WR002776.

403 Ghisalberti, M., Nepf, H., 2005. Mass transport in vegetated shear flows. Environmental Fluid
404 Mech 5, 527-551.

405 Ghisalberti, M., Nepf, H., 2006. The structure of the shear layer in flows over rigid and flexible
406 canopies. Environmental Fluid Mechanics 6, 277-301.

Grizzle, R.E., Short, F.T., Newell, C.R., Hoven, H., Kindblom, L., 1996. Hydrodynamically induced synchronous waving of seagrasses: 'monami' and its possible effects on larval mussel settlement. Journal of Experimental Marine Biology and Ecology 206, 165-177.

Hughes, A.R., Inouye, B.D., Johnson, M.T., Underwood, N., Vellend, M., 2008. Ecological consequences of genetic diversity. Ecology Letters 11, 609-623.

Hughes, A.R., Stachowicz, J.J., 2004. Genetic diversity enhances the resistance of a seagrass ecosystem to disturbance. Proceedings of the National Academy of Sciences 101 (24), 8998-9002.

Infantes, E., Orfila, A., Simarro, G., Terrados, J., Luhar, M., Nepf, H., 2012. Effect of a seagrass (*Posidonia oceanica*) meadow on wave propagation. Mar. Ecol. Prog. Ser. 456, 63-72.

Israelsson, P.H., Y.D. Kim, E.E. Adams, 2006. A comparison of three Lagrangian approaches for extending near field mixing calculations. Environ Model Softw 21, 1631-1649.

Lightbody, A., Nepf, H., 2006. Prediction of velocity profiles and longitudinal dispersion in emergent salt marsh vegetation. Limnology and Oceanography 51 (1), 218-228.

Luhar, M., Nepf, H.M., 2011. Flow-induced reconfiguration of buoyant flexible aquatic vegetation. Limnol. Oceanogr. 56 (6), 2003-2017.

McKone, K. 2009. Light available to the seagrass Zostera marina when exposed to currents and waves, Univ. Maryland, PhD Thesis.

Moore, K.A., 2004. Influence of seagrasses on water quality in shallow regions of the lower Chesapeake Bay. J Coast Res (20), 162–178.

Nepf, H., 2012. Flow and transport in regions with aquatic vegetation. Annu. Rev. Fluid Mech. 44, 123-142.

Nepf, H., Ghisalberti, M., White, B, Murphy, E., 2007. Retention time and dispersion associated with submerged aquatic canopies. Water Res. Res. 43, W04422.

Palmer, M.R., Nepf, H., Pettersson, T.J.R., 2004. Observations of particle capture on a cylindrical collector: Implications for particle accumulation and removal in aquatic systems. Limnol. Oceanogr. 49 (1), 75-85.

van Katwijk, M., Thorhaug, A., Núria, M., Orth, R., Duarte, C., Kendrick, G., ... Verduin, J., 2016. Global analysis of seagrass restoration: the importance of large-scale planting. Journal of Applied Ecology 53, 567-578.

Kendrick, G.A., Waycott, M., Carruthers, T.J.B., Cambridge, M.L., Hovey, R., Krauss, S.L., ... Verduin, J., 2012. The central role of dispersal in the maintenance and persistence of seagrass populations. BioScience 62 (1), 56-65.

441 Luhar, M., Nepf, H., 2011. Flow-induced reconfiguration of buoyant and flexible aquatic
442 vegetation. Limnol. Oceanogr. 56 (6), 2003-2017.

443 Pan, Y., Chamecki, M., Isard, S.A., 2014: Large-eddy simulation of particle dispersion inside the
444 canopy roughness sublayer. J. Fluid Mech, in review.

445 Sand-Jensen, K., 1998. Influence of submerged macrophytes on sediment composition and
446 near-bed flow in lowland streams. Freshwater Biology 39, 663-679.

447 Unsworth, R.K.F., Cullen, L.C., Pretty, J.N., Smith, D.J., Bell, J.J., 2010. Economic and subsistence values of
448 the standing stocks of seagrass fisheries: potential benefits of no-fishing marine protected area
449 management. Ocean and Coastal Management 53, 218-224.

450 Vogel, S., 1984, Drag and flexibility in sessile organisms. American Zoology 24, 37-44.

451 Wilson, J.D., Sawford, B.L., 1996. Review of Lagrangian stochastic models for trajectories in the turbulent
452 atmosphere. Boundary-Layer Meteorol 78, 191-210.

453 Wilson, J.D., Yee, E., 2007. A critical examination of the random displacement model of turbulent
454 dispersion. Boundary-Layer Meterorol 125, 399-416

455

Chapter 7

Conclusion

In order to predict the resiliency and future growth of vegetated systems, it is necessary to consider the physical mechanisms governing the feedbacks between plants, flow, and particle fate. Environmental flows carry a wide variety of particles which interact with vegetation. Vegetated canopies are anchored by sediment, release pollen and seeds to colonize new ground, rely on nutrients carried by sediment, and may be killed by disease spores. This thesis investigated particle transport in the context of the canopy-mediated flow environment through laboratory experiments and numerical modeling, advancing understanding of canopy mediated particle transport and improving model predictions.

Chapter 2 demonstrated the effect of rigid emergent patches on bedload sediment transport and fine particle deposition (Follett and Nepf, 2012). Scouring within the patch was positively correlated with in-patch turbulent kinetic energy, and the transport length scale of scoured sediment was dependent on patch area density and diameter. Deposition in the extended wake zone behind the patch encouraged future vegetative growth, resulting in a steady state teardrop formation (Gurnell et al., 2001, 2008, Chen et al., 2012). By mediating its environment through flow diversion and attenuation, vegetation acts as an ecosystem engineer, creating habitat conducive to future growth. Similar feedbacks have been observed in Zostera marina (van Katwijk et al., 2010). In nutrient limited conditions, the seagrass maintained a high canopy density, promoting nutrient capture. In environments with excess nutrients, however, sediment anoxia reduced the canopy area density, so that nutrients were resuspended and exported from the canopy.

In Chapter 3, results were presented from laboratory experiments investigating the capture of particles released in a 10 m long submerged model canopy. Particle capture increased as the vertical updraft decayed over the initial adjustment region, reaching a maximum at the end of this region, where the vertical updraft had decayed, but the canopy scale turbulence had not reached its full strength. In the fully developed region, particle capture was reduced for releases above the vortex penetration distance, reflecting the influence of canopy scale vortices. The presence of vegetation induced flow divergence and the development of a mixing layer, which in turn influenced particle transport. The differing transport patterns within the adjustment and fully developed regions could be considered when designing field studies, such as in the placement of sediment traps. Flow diversion and the development of canopy scale vortices also occur in terrestrial flows, potentially increasing the escape of fungal spores produced within the adjustment region. Because particle transport depends on the relative balance of the particle settling velocity and the Reynolds stresses at the top of the canopy, the particle transport trends observed in this aquatic study could also

represent terrestrial particles with a similar scaling.

Chapter 4 (Pan et al., 2014) described the impact of unsteady reconfiguration of flexible seagrass meadows on the penetration of turbulence into the canopy. This chapter described the drag reduction as a function of the flow velocity and blade parameters, allowing large eddy simulations to reproduce measured skewness values. Larger, stronger turbulent structures that bend the blades experience reduced canopy drag relative to smaller, weaker structures that do not bend the blades, leading to greater penetration of larger structures into the canopy, which is reflected in an increased the velocity skewness within the canopy. Because the penetration of large scale structures is favored in the weak reconfiguration regime, for which the Vogel number achieves its peak negative value, flexible canopies within this regime would experience greater penetration of large scale structures and higher skewness values than rigid canopies, potentially impacting resuspension and water clarity.

Chapter 5 (Follett et al., 2016) used existing literature to construct profiles of velocity and eddy diffusivity from a simple set of parameters [canopy height, canopy density, vegetation length scale, and wind speed]. The profiles were used to drive an RDM model that predicted particle escape from the canopy without the need for detailed velocity field measurements. This chapter provided a physically grounded description of particle fate that could realistically replace empirical relations in long-distance spore transport models, reducing fungicide use through improved predictions of fungal disease spread. Similar physical mechanisms govern the structure of the canopy shear layer and particle transport in both terrestrial and aquatic flows, so that transport could be explored in either fluid. Because the RDM does not require significant computational resources, a wide parameter space could be explored, guiding the design of field experiments or the choice of parameters for more computationally intensive simulations.

Future work on the intersection of plants, flow, and particle fate could consider the influence of canopy hydrodynamics on pollination and sediment transport in submerged aquatic vegetation, such as seagrasses. Seagrass meadows, which mediate turbidity and increase biodiversity by providing shelter for larvae and small fish, are declining worldwide. A recent meta-analysis of meadow restoration attempts found that only 37% of restoration efforts were successful, highlighting the importance of supporting existing meadows before collapse occurs (van Katwijk et al., 2016). Increased genotypic diversity in the seagrass *Zostera marina* has been shown to enhance resistance to disturbances (Hughes and Stachowicz, 2004). Meadow genotypic diversity depends on successful pollination, reliant on the transport of pollen particles. As a first step, Chapter 6 explored the transport of seagrass pollen as a function of canopy and particle characteristics using a random walk method similar to Chapter 5, but with velocity and diffusivity profiles constructed based on studies with submerged flexible canopies. The model was validated using a release of polyethylene particles in a *Zostera marina* canopy (Ackerman, 2002). The distance over which half of released particles were captured by the canopy decreased during a flood tide, due to increased efficiency of vertical impaction and reduced mixing associated with the onset of canopy waving, or *monami*. Future work could investigate the transport of pollen as submergence depth is increased, exploring observations of reduced genetic diversity in the subtidal region, compared to canopies with reduced submergence depth (de Cock, 1980, Hughes and Hays, personal communication, March 30, 2016). Subsequently, pollen transport in patchy landscapes, as compared to a continuous canopy, and the influence of epiphyte presence could be considered.

References

Ackerman, J.D., 2002. Diffusivity in a marine macrophyte canopy: Implications for submarine pollination and dispersal. American Journal of Botany 89 (7), 1119-1127.

Chen, Z., Ortiz, A., Zong, L., Nepf, H., 2012. The wake structure behind a porous obstruction and its implications for deposition near a finite patch of emergent vegetation. Water Res. Res. 48, W09517.

de Cock, A.W.A.M., 1980. Flowering, pollination and fruiting in Zostera marina L. Aquatic Botany 9, 201-220.

Follett, E., Nepf, H., 2012. Sediment patterns near a model patch of reedy emergent vegetation. Geomorphology 179, 141-151.

Follett, E., Chamecki, M., Nepf, H., 2016. Evaluation of a random displacement model for predicting particle escape from canopies using a simple eddy diffusivity model. Agricultural and Forest Meteorology 224, 40-48.

Gurnell, A.M., Petts, G.E., Hannah, D.M., Smith, B.P.G., Edwards, P.J., Kollmann, Tockner, K., 2001. Riparian vegetation and island formation along the gravel-bed Fiume Tagliamento, Italy. Earth Surf. Process. Landforms 26, 31-62.

Gurnell, A.M., Blackall, T.D., Petts, G.E., 2008. Characteristics of freshly deposited sand and finer sediments along an island-braided, gravel-bed river: The roles of water, wind and trees. Geomorphology 99, 254-269.

Hughes, A.R., Stachowicz, J.J., 2004. Genetic diversity enhances the resistance of a seagrass ecosystem to disturbance. Proc Natl Acad Sci 101 (24), 8998-9002.

van Katwijk, M.M., Bos, A.R., Hermus, D.C.R., Suykerbuyk, W., 2010. Sediment modification by seagrass beds: Muddification and sandification induced by plant cover and environmental conditions. Estuarine, Coastal and Shelf Science 89, 175-181.

van Katwijk, M., Thorhaug, A., Marb, N., Orth, R.J., Duarte, C.M., Kendrick, G.A., Verduin, J.J., 2016. Global analysis of seagrass restoration: the importance of large-scale planting. Journal of Applied Ecology 53, 567-578.

Pan, Y., Follett, E., Chamecki, M., Nepf, H., 2014. Strong and weak, unsteady reconfiguration and its impact on turbulence structure within plant canopies. Physics of Fluids 26, 105102.

Appendix A

RDM code used in chapters 3 and 5

```
%%
%RDM code used in Chapter 6
%to run, you need profiles of u, Kz, dKz/dz in cm/s and
%cm^2/s and projected area (1/m) in the x and
%z directions (ax, az). The above is an example for
%filamentous particles from Ackerman, 2002.
hm=1; ustar=0.005; cd=1; a=.91; d=0.005; H=5;
%canopy height, u*, cd, a, submergence depth
[z u Kz]=createuKzflexible(hm,ustar,cd,a,d,H,0); %0-no monami, 1-monami
Dz=Kz.*100^2; %convert to cm2/s from m2/s
z=z.*100;
h=hm*100; u=u.*100;
lKz=length(Dz);
dDz=zeros(1,lKz); zdDz=zeros(1,lKz);
dDz(2:lKz)=diff(Dz)./diff(z);
zdDz(2:lKz)=mean([z(1:(lKz-1))',z(2:lKz)']');
zdDz(lKz)=10*h;
ax=ackPx(:,1)*0.91;
az=(ackPz(:,1))*0.91;
zP=ackPx(:,2).*100; zP(end)=h;
H=H*100; L=450; %arbitrary length of canopy in cm
%Ackerman pole locations from Ackerman, 2002
xpole=[1.5 2 2.5 3 3.5].*100;
ypole=[-0.5 -0.25 0 0.25 0.5].*100;
dyp=2.5; %cm
for xi=1:length(xpole)
    poledep{xi}=[];
end
%-------------------------SET UP START CONDITIONS-------------------------
tic
for runind=1 %can run multiple times to generate repeats
numParticles=1000;
space=1; %this can be used for a continuous release, try numParticles/10
numSteps=20000;
```

```
allws=[4.7e-3]; %input particle settling velocity (can be an array)
injHeightreal=1*h;  %input injection heights (can be an array)
wschoice=1;
for i=wschoice %length(allws)
    ws=allws(wschoice);
    delt=min([abs(0.1*h/max(dDz-ws)) (0.1*h)^2/max(Dz) 1],[],2);
 %also make sure P(deposition) is less than 1 for each time step
    injchoice=1;
    QCall=zeros(length(injHeightreal),4);
for injHeight=injchoice %injection heights
particle_release=floor(linspace(1,space,numParticles));
particle_pos=zeros(2,numParticles);
partnum=0; numSettle=0; numEscape=0; numAdvect=0; numCanopy=0;
velStepX=zeros(1,numParticles); ticleave=zeros(1,numParticles);
velStepZ=zeros(1,numParticles); ticenter=zeros(1,numParticles);
pos_save=zeros(numSteps,numParticles,2);
particles=zeros(1,numParticles);
settleindsave=zeros(1,numParticles); escapeindsave=zeros(1,numParticles);
canopyindsave=zeros(1,numParticles);
for stepnum=1:numSteps
    %find velocity for all particles
    posParticlesZ=find(particle_pos(2,:));
    if nnz(particle_pos)~=0
    for k=nonzeros(posParticlesZ)';
        R=normrnd(0, 1);
        velStepX(k)=interp1(z,u,particle_pos(2,k))*delt;
        velStepZ(k)=(interp1(zdDz,dDz,particle_pos(2,k))-ws)*delt+...
R*sqrt(2*interp1(z,Dz,particle_pos(2,k))*delt);
    end
    for k=nonzeros(particles(particle_pos(2,:)==0))';
        velStepZ(k)=0; velStepX(k)=0;
    end
    %update particle position
    particle_pos(2,posParticlesZ)=particle_pos(2,posParticlesZ)+...
        velStepZ(posParticlesZ);
    particle_pos(1,posParticlesZ)=particle_pos(1,posParticlesZ)+...
        velStepX(posParticlesZ);
 %canopy deposition modified from Palmer et al., 2004----------------------
    for k=nonzeros(posParticlesZ)' %define Px and Pz above
    if particle_pos(2,k)<=h && particle_pos(2,k)>0
    dp=4e-3; %input particle diameter here, m
    dc=d; %collector (blade) diameter, m
 %upward facing surfaces---------------------------------------------------
    azk=interp1(zP,az,particle_pos(2,k)); %projected one sided leaf area in z
    Recz=max([0 velStepZ(k)./100*dc/(1.0034e-6)]);
    Rz=dp/dc;
    etaz=0.224*(Recz)^0.718*(Rz)^2.08;
    Pz=etaz*azk*velStepZ(k)./100; %since the projected area is in m^-1,
```

```
 %velocity must be in meters
%vertical surfaces-------------------------------------------------------
    axk=interp1(zP,ax,particle_pos(2,k)); %one sided leaf area in x 1/m
    Recx=velStepX(k)./100*dc/(1.004e-6); %Lv=Lvx since bent over
    Rx=dp/dc; %Palmer 2004
    etax=0.224*(Recx)^0.718*(Rx)^2.08; %assume etax=etay=etaz
    Px=etax*axk*velStepX(k)./100;
%random chance-----------------------
   Pall=(Px+Pz); %again, this needs to be less than 1 (constraint on delt)
   R=rand(1);
   if R<=Pall
       numCanopy=numCanopy+1;
       canopyindsave(k)=stepnum;
       particle_pos(2,k)=0;
       particle_pos(1,k)=0;
   end
    end
    end
%see where particles are when they contact the pole (Ackerman study)
for xi=1:length(xpole)
    beforex=pos_save(stepnum-1,:,1)<xpole(xi);
    afterx=particle_pos(1,:)>=xpole(xi);
    ximpact=beforex.*afterx; %everyone that crossed a pole in that timestep
    polepartx=find(ximpact);
    polepart=find(ximpact);
    poledep{xi}=[poledep{xi} particle_pos(2,polepart)]; %save z location
end
    %does particle settle in this timestep?
    numAdvect=numParticles-(numSettle+numEscape+numCanopy);
    numSettle=numSettle+length(find(particle_pos(2,:)<0));
    particle_pos(1,find(particle_pos(2,:)<0))=0; %particle settles
    particle_pos(2,find(particle_pos(2,:)<0))=0;
    particle_pos(1,find(particle_pos(2,:)>H))=...
pos_save(stepnum-1,find(particle_pos(2,:)>H),1)+0.0001;
    particle_pos(2,find(particle_pos(2,:)>H))=H-0.001; %bounces off surface
    particle_pos(2,find(particle_pos(1,:)>L))=0; %stop when >L
    particle_pos(1,find(particle_pos(1,:)>L))=0;
    pposnonz=nonzeros(particle_pos(2,:));
    end
    advectind=find(ones(1,numParticles)-...
(canopyindsave+settleindsave+escapeindsave)>zeros(1,numParticles));
    %release particles
    if partnum~=numParticles&&stepnum==particle_release(partnum+1)
%release particle if stepnum==release time
        particle_pos(2,(partnum+1):(partnum+length(find(...
particle_release==stepnum))))=injHeightreal(injHeight);
        particle_pos(1,(partnum+1):(partnum+length(find(...
particle_release==stepnum))))=0;
```

```
        partnum=partnum+length(find(particle_release==stepnum));
        particles(partnum)=partnum;
        pos_save(stepnum,:,:)=particle_pos(:,1:numParticles)';
        continue
    elseif partnum==0
        continue
    end
    pos_save(stepnum,:,:)=particle_pos(:,1:numParticles)';
end
    disp(['ws=' ,num2str(i),'injHeight=' ,num2str(injHeight)])
end
end
end
disp('done')
toc

function [z u Kz]=createuKzflexible(h,ustar,cd,a,d,H,toggle)
delU=ustar/.1; %can use u* or delU depending on available data
%ustar=0.1*delU;
uh=delU/(16*a*d+1);
kappa=0.4;
u1=uh*(.21*(cd*a*h)^-.45);
u2=u1+delU;
z1=max([0 h.*(0.63-0.29/(cd*a*h))]);
hz1=h-z1;
tml=hz1/0.38;
theta=tml/7.1;
z=0:0.001:4*h;
u=0.5.*delU.*tanh((z-(h+0.5*theta))./(2*theta))+.5*(u1+u2);
z2=z1+tml;
%Kz----------------------------------------------------------------------
Kzw=0.14*u*d;
Kzh=0.032*delU*tml;
if toggle==1
    Kzh=Kzh/2; %reduced momentum for flexible canopies if monami present
end
Kz2=0.013*delU*tml;
Kz1=Kzw.*(z<=z1);
Kzwmean=mean(Kzw(find(z<=z1)));
KzCzloc=find((z<=h).*(z>z1));
KzCval=interp1([z1 h],[Kzwmean Kzh],z(KzCzloc));
KzCfill=zeros(size(z)); KzCfill(KzCzloc)=KzCval;
KzMzloc=find((z>h).*(z<=z2));
KzMval=interp1([h z2],[Kzh Kz2],z(KzMzloc));
KzMfill=zeros(size(z)); KzMfill(KzMzloc)=KzMval;
KzH=Kz2.*(z>z2);
Kz=Kz1+KzCfill+KzMfill+KzH;
```

```
%%
%RDM code used in ch.3 (terrestrial crops)
%cd*a, h, cd, u*, vegetation length scale
[u Kzd z]=makefamilyLuhar_overh(0.68*1.65,2.1,0.68,.51,0.1);
h=2.1;
Dz=Kzd.*100^2; %convert to cm2/s from m2/s
z=z.*100;
h=2.1*100;
lKz=length(Dz);
dDz=zeros(1,lKz); zdDz=zeros(1,lKz);
dDz(2:lKz)=diff(Dz)./diff(z);
zdDz(2:lKz)=mean([z(1:(lKz-1))',z(2:lKz)']');
zdDz(lKz)=10*h;
%%
%-----------------------SET UP START CONDITIONS-----------------------------
tic
for runind=1
space=1; %number of steps to space release over %make this f(numSteps)?
numParticles=1000;
numSteps=20000;
allws=[1.94,10]; %settling velocities (cm/s)
injHeight2=[0.1 0.2105 0.2939 0.3772 0.4605 0.5439 0.6272, ...
0.7105 0.7939 0.8772 0.9605 1].*h;
injHeight10=[0.1 0.2939 0.3816 0.4605 0.5439 0.6316,...
 0.7105 0.7939 0.8772 0.9605 1].*h;
wschoice=1:2;
delt=.03; %time step (s)
H=10*h; %height at which particles are assumed to always be above h (cm)
L=18*h; %stop all particles at this point
zaz=[0 0.15 0.1500001 0.30 0.3000001 0.45 0.4500001 0.6 0.600001,...
 0.75 0.7500001 0.9 0.900001 1].*h;
az=[0.34 0.34 0.75 0.75 1.36 1.36 1.50 1.50 1.61 1.61 1.50,...
 1.50 0.43 0.43].*3.3.*0.01; %from T.1 Pan/chamecki JFM draft
escapeindsave=zeros(1,numParticles);
settleindsave=zeros(1,numParticles);
canopyindsave=zeros(1,numParticles);
ind1=length(allws); ind2=11;
numSettleSave=zeros(ind1,ind2);
stdSettleSave=zeros(ind1,ind2); numCanopySave=zeros(ind1,ind2);
numEscapeSave=zeros(ind1,ind2);
for i=wschoice %length(allws)
    ws=allws(i);
    if i==1
        injHeightreal=injHeight2;
    elseif i==2
        injHeightreal=injHeight10;
    end
    injchoice=1:length(injHeightreal);
```

```
for injHeight=injchoice %injection heights
particle_release=floor(linspace(1,space,numParticles)); %space release times over
particle_pos=zeros(2,numParticles); %everyone initially at 0
partnum=0; numSettle=0; numEscape=0; numAdvect=0; numCanopy=0;
velStepX=zeros(1,numParticles); ticleave=zeros(1,numParticles);
velStepY=zeros(1,numParticles); ticenter=zeros(1,numParticles);
pos_save=zeros(numSteps,numParticles,2);
particles=zeros(1,numParticles);
settleindsave=zeros(1,numParticles); escapeindsave=zeros(1,numParticles);
canopyindsave=zeros(1,numParticles);
for stepnum=1:numSteps
    %find velocity for all particles
    posParticlesY=find(particle_pos(2,:));
    if nnz(particle_pos)~=0
    for k=nonzeros(posParticlesY)';
        %delt=interp1(z,deltz,particle_pos(2,k));
        R=normrnd(0, 1);
        velStepX(k)=interp1(z,u,particle_pos(2,k))*delt;
        velStepY(k)=(interp1(zdDz,dDz,particle_pos(2,k))-ws)*delt+...
R*sqrt(2*interp1(z,Dz,particle_pos(2,k))*delt);
    end
    for k=nonzeros(particles(particle_pos(2,:)==0))';
        velStepY(k)=0; velStepX(k)=0;
    end
    %update particle position
    particle_pos(2,posParticlesY)=particle_pos(2,posParticlesY)+...
        velStepY(posParticlesY);
    particle_pos(1,posParticlesY)=particle_pos(1,posParticlesY)+...
        velStepX(posParticlesY);
    %canopy deposition----------------------------------------------
    for k=nonzeros(posParticlesY)'
    fv=0; fu=0; Px=0.28; Py=0.28; Pz=0.44; lv=10; Sp=0;%aylor 2005
    azk=interp1(zaz,az,particle_pos(2,k)); %in cm to match velocity
    velrt=sqrt((velStepX(k)./delt).^2); %assumes v=0;
    if velrt<0.45*100; %Vcrit=0.45 m/s from JFM draft pan chamecki
        fv=1; fu=1;
    end
    Spu=fu*Px*azk*ws;
    St=(ws/(9.8*100))*(velrt/lv);
    Ei=0.86*(1+0.442*St.^-1.967).^-1;
    Si=Ei*(Px+Py)*azk*velrt;
    Spv=fv*Si;
   if (velStepY(k)./delt-ws)<0
        Sp=(Spv+Spu)*delt;
   elseif (velStepY(k)./delt-ws)>=0
        Sp=Spv*delt;
   end
   R=rand(1);
```

```
    if R<=Sp
        numCanopy=numCanopy+1;
        canopyindsave(k)=stepnum;
        particle_pos(2,k)=0;
        particle_pos(1,k)=0;
    end
     end
     %settle or escape
     numSettle=numSettle+nnz(particle_pos(2,find(particle_pos(2,:)~=0))<0);
     numEscape=numEscape+nnz(find(particle_pos(2,:)>H));
     numAdvect=numParticles-(numSettle+numEscape+numCanopy);
     particle_pos(1,find(particle_pos(2,:)<0))=0;
     particle_pos(2,find(particle_pos(2,:)<0))=0;
     particle_pos(1,find(particle_pos(2,:)>H))=0;
     particle_pos(2,find(particle_pos(2,:)>H))=0;
     particle_pos(2,find(particle_pos(1,:)>L))=0;
     particle_pos(1,find(particle_pos(1,:)>L))=0;
     pposnonz=nonzeros(particle_pos(2,:));
     end
     advectind=find(ones(1,numParticles)-...
(canopyindsave+settleindsave+escapeindsave)>zeros(1,numParticles));
     %release particles
     if partnum~=numParticles&&stepnum==particle_release(partnum+1)
%release particle if stepnum==release time
         particle_pos(2,(partnum+1):(partnum+length(...
find(particle_release==stepnum))))=injHeightreal(injHeight);
         particle_pos(1,(partnum+1):(partnum+length(...
find(particle_release==stepnum))))=0;
        partnum=partnum+length(find(particle_release==stepnum));
         particles(partnum)=partnum;
         pos_save(stepnum,:,:)=particle_pos(:,1:numParticles)';
         continue
     elseif partnum==0
         continue
     end
     pos_save(stepnum,:,:)=particle_pos(:,1:numParticles)';
end
     numCanopySave(i,injHeight)=numCanopy;
     numEscapeSave(i,injHeight)=numEscape+numAdvect;
     numSettleSave(i,injHeight)=numSettle;
     disp(['ws=␣',num2str(i),'␣injHeight=' ,num2str(injHeight)]);
end
end
end
disp('done')
toc

function [u Kzall zall]=createuKzch3(cdah,h,cd,ustar,Lv)
```

```
kappa=0.4; %
ah=cdah./cd;
Sc=.5; %Schmidt number
a=ah/h;
de=min([0.23/(cd*a),h]);
zm=max([0,h.*(1-.12/(cd*ah))]) ;%Luhar eq. 6 p. 7
if cd*ah<0.099999999999999999
    z0=4*(cd*ah);
elseif cd*ah>=0.09999999999999999999999
    z0=.04/(cd*ah);
end
z0=z0*h;
zall=[linspace(0,h,20) linspace(h+.01,10*h,180)];
%1. u profile
uBL=ustar/kappa.*log((zall-zm)./z0); %Luhar eq. 5 p. 6
uh=real(interp1(zall,uBL,h));
u10=interp1(zall,uBL,10);
if cd*ah<0.0999
    disp('sparse')
    cd*ah;
    betaB=ustar/uh;
elseif cd*ah>=0.0999
    betaB=1/2.6;
end
lm=2*betaB^3/(cd*a);
u1uhw=.1638*ah^-.6842;
u1w=u1uhw*uh;
if u1w>uh
    u1w=uh; %truncate power law below ah=.0711 (shoots up)
end
uC=u1w+(uh-u1w)*exp(betaB*(zall-h)./lm);
uC=u1w+(uh-u1w)*exp(0.5*cd*a*(1/betaB)^2*(zall-h));
u3=uBL.*(zall>=h); %3 for above canopy; 1 for canopy
u3(isnan(u3))=0;
u1=uC.*(zall<h);
u=u1+u3;
u(isnan(u))=0;
%u=u./uh;
%now for Kz
poggi=importdata('C:\Users\emf\G3data\Pictures\poggi_alphaa.dat');
poggi(:,1)=[0.02 0.04 0.09 0.23 0.56]';
alpha=interp1(poggi(:,1),poggi(:,2),cdah);
if alpha>0.45 || cdah>max(poggi(:,1))
    alpha=0.45;
elseif alpha<0 || cdah<min(poggi(:,1))
    alpha=0;
end
%1. wake zone has small constant value
```

```
Kzcoeff=findcoeff(a,cd);
Kz1=Kzcoeff.*u.*Lv; %changed from u for checking!!
Kz1de=interp1(zall,Kz1,(h-de));
%2a. mixing layer--linear model ([K1,h-de],[Kzh,h])
dudzML=uh/de;
lML=min([2/(cd*a)*(betaB)^2,h]);
lBL=kappa*(zall-zm);
lbldisp=interp1(zall,lBL,h);
leff=(1-alpha)*lBL+alpha*lML;
leffdisp=interp1(zall,leff,h);
Kz2=leff.^2.*abs(dudzML);
Kzh=interp1(zall,Kz2,h)*(1/.5);
if de<=h
    Kz2fill=interp1([(h-de) h],[Kz1de Kzh],...
zall(find((zall<=h).*(zall>(h-de)))));
end
Kz2=zeros(size(zall)); Kz2(find((zall<=h).*(zall>(h-de))))=Kz2fill;
Kzhsavei=Kzh;
%3. boundary layer model
%3a. some combination of ML and BL (Poggi alpha)
if de<=h
    Kz3MLfill=interp1([h (h+de)],[Kzh Kz1de],...
zall(find((zall>h).*(zall<=(h+de)))));
end
Kz3ML=zeros(size(zall)); Kz3ML(find((zall>h).*(zall<=(h+de))))=Kz3MLfill;
lBL=kappa*(zall-zm);
dudzBL=ustar/kappa.*(1./(zall-zm));
Kz3BL=(1/0.8)*kappa*ustar.*(zall-zm); %lBL.^2.*abs(dudzBL);
%3c. Decrease Kz over de from Kzh to boundary layer value.
zlocMLbound=find(zall>=(h+de)); zlocMLbound=zlocMLbound(1);
Kz3fill=interp1([h (h+de)],[Kzh Kz3BL(zlocMLbound)],zall(find((zall>h)...
    .*(zall<=(h+de)))));
Kz3=zeros(size(zall)); Kz3(find((zall>h).*(zall<=(h+de))))=Kz3fill;
%4. pure boundary layer model--if section 3 has upper bound
Kz4=Kz3BL;
%FINAL: add everything together
Kzall=Kz1.*(zall<(h-de))+Kz2.*((zall>=(h-de)).*(zall<=h))+Kz3.*((zall>h)...
    .*(zall<=(h+de)))+Kz4.*(zall>(h+de));
Kzall=Kzall;
```